Dynamics of spinor Fermions

Ph. D. Thesis

submitted by

Ulrich Ebling

ICFO - The Institute of Photonic Sciences
Castelldefels (Spain)

Thesis advisor:
Prof. Dr. Maciej Lewenstein
Thesis Co-advisor:
Dr. André Eckardt

Abstract

Ultracold atomic gases have established themselves as quantum systems, which are clean and offer a high degree of control over crucial parameters. They are well isolated from their environment and thus offer the possibility to study coherent many-body dynamics. This allows, e.g. to address the fundamental question, whether and how an isolated quantum many-body system can thermalize. In this thesis, we present results regarding the dynamics of ultracold Fermions with large spin. Fermionic spinor gases are different from bosonic spinor gases, which have been studied in greater detail the past, because the Pauli-Principle ensures that many single-particle modes are involved. They also differ from the typical situation in condensed matter physics, due to both the presence of the trap and the possibility of having fermions with large ($> 1/2$) spin. Compared to the spin-$1/2$ case, large spin fermions must have one of two possible new properties. Either they obey an enhanced SU(N) symmetry between all spin states, (this attracted great interest recently), or they feature spin-changing collisions (and a non-trivial quadratic Zeeman shift). Here, we address the latter case, which is relevant for alkaline atoms such as Potassium-40.

When studying the weakly interacting scenario, one can still distinguish three different regimes. For extremely weak interactions, the system is in the collisionless regime and interactions can be taken into account on a mean-field level. For sufficiently strong interactions on the other hand, collisions are expected to ensure local equilibrium, such that the system is described by hydrodynamic equations of fields like density, magnetization or temperature, which only depend on position. For the intermediate regime however, there is no simple description. Moreover, the scattering cross-section for spin-changing and spin-conserving collisions can be quite different for large-spin fermions, such that a situation can be found in which the system might be hydrodynamic with respect to one process but not the other. In this thesis, a semi-classical Boltzmann-type theory with full spin coherence is developed (and implemented on the machine) that allows one to interpolate between the collisionless and hydrodynamic regime. Both the presence of the trap as well as fermions with large spin are included.

This approach goes beyond mean-field theory and corresponds to the intuitive Ansatz to treat the single-particle dynamics as an open system coupled to the environment given by all other particles. Our theory is derived from the microscopic Hamiltonian of the full system and even though it does not allow for an exact treatment, we find good agreement with experiments performed in the group of Klaus Sengstock at Hamburg University, using ultracold Potassium.

We begin by investigating the effect of the harmonic trap on a two-component, collisionless system. We find a dynamical mechanism for spin-segregation, the mean-field driven creation of two domains of opposite magnetization in phase-space, building up from a spiral spin segregation in the trap. The effect finds a transparent explanation when introducing the concept of dynamically induced long-range interactions, occurring when the fast phase-space rotation induced by a strong parabolic trap effectively smears out the contact interactions.

Further results in this thesis have been achieved in collaboration with the experimental group of Klaus Sengstock in Hamburg. In the first project, we study the collective excitations of a trapped four-component Fermi gas. Long-wavelength spin waves (sloshing, breathing, ...) are excited by preparing all atoms in a coherent superposition of spin states and using a short magnetic field gradient to wind up a phase spiral. During the subsequent dynamics, the four spin components counter-oscillate in the trap, while the total density remains constant. The dynamics, including amplitude and frequency, can be understood quantitatively on a mean-field level by disentangling it into dipolar, nematic and octupolar spin configurations.

In a further experiment with spin-$9/2$ fermions, it was found that spin-changing interactions can lead to collective and coherent oscillations of the spin state of the whole Fermi sea, living for long times of several seconds. It is found theoretically, that these giant oscillations are protected from spatial dephasing by dynamically induced long-range interactions. Also the suppression of such oscillations, observed in the high-density regime, is identified to be the consequence of incoherent non-forward scattering, beyond mean-field.

In the last project, we study collision processes in ultracold Potassium in even greater detail. We find that they can be arranged in three categories: Spin-changing vs. spin-conserving collisions, processes depending on density vs. processes depending on gradients of density, and forward vs. lateral scattering. With this categorization, as well as the exact dependence of each process on scattering lengths and momenta, we can explain and simulate not only the coherent mean-field driven oscillations, but also relaxation effects that appear to be incoherent on the single-particle level. For example, in agreement with experiment, spin-conserving relaxation processes are found to occur much faster than the redistribution of the particles between different spin states.

Contents

II Application to trapped Fermi gases 55

Chapter 1

Introduction

Progress in the field of ultracold atoms in the last decade has established them as valuable systems, with which physicists can improve their understanding of quantum many-body systems, especially dynamics. Trapped ultracold atomic systems offer new possibilities to simulate theoretical models, because they are in general very clean, isolated from their environment and crucial parameters can be controlled with high accuracy [1–4]. This control extends over temperature, particle number, interactions to even the dimensionality, or more general geometry of the system. Experimental work on the subject ranges back to early work on superfluidity in liquid Helium [5], while the major breakthrough was made in the 1990s with the demonstration of Bose-Einstein condensation (BEC) in Rubidium [6, 7]. Further milestones were the preparation of a degenerate Fermi gas [8] and the development of optical lattices, with which a variety of problems from solid state physics can be studied [3].

Research on cold atoms can be roughly divided into two paths. A large proportion focuses on equilibrium properties of many-body systems, where possibly the most famous example is the transition from the superfluid phase to the Mott-insulator regime [9]. Other famous lines of work in this field are the BEC-BCS crossover [10, 11] and the search for itinerant ferromagnetism in strongly interacting Fermi gases [12–15]. Here, especially large-spin systems are expected to have very rich phase diagrams [16–19]. The second path is the *dynamics* of ultracold atomic systems far from equilibrium. Research on dynamics deals with e.g. transport properties [20, 21], domain and texture formation [22, 23] and recently the relaxation of such systems after a quench, where it is hoped that studies of ultracold atoms provide insight on how closed quantum many-body systems equilibrate [24–30].

In this thesis, we present advances concerning the dynamics of Fermi gases. Traditionally, the motivation for work on Fermi gases comes from the field of condensed matter physics, since electrons and ^{3}He atoms both are fermions. However, in ultracold atoms, situations can occur, which are absent in traditional condensed matter systems and consequently have not been addressed so far. Electrons are fermions with spin 1/2, while trapped atoms can have much larger values of spin, such as ^{40}K with spin 9/2 featured in this thesis. The larger spin adds novel properties to the system compared to the spin 1/2 case. The magnetic quantum number m of an atom of spin F has $2F+1$ values. In some atoms, mostly alkaline-earths with zero electron spin, this leads to an enhanced symmetry of SU(N) of the Hamiltonian, where $N = 2F+1$ [31–35]. In the more general case without the SU(N) symmetry, such as it occurs in alkali atoms, interactions of particles will depend on the total spin of the collision partners. Hence, scattering processes in large-spin systems are described by more than a single scattering length, depending on the internal state of the colliding atoms. As a direct consequence, collisions can allow the incoming and outgoing spin states $\{m_1, m_2\} \rightarrow \{m_3, m_4\}$ to be different, which is prohibited in a spin 1/2 system by conservation of total magnetization $M = m_1 + m_2 = m_3 + m_4$. This has consequences together with the fact that level splittings induced by a magnetic field are in general not uniform because of the nonlinear Zeeman effect: a large number of different energies and hence time-scales affect the dynamics of the system, which in turn becomes much more complex than the spin 1/2 case. A second feature of cold atom physics, which is absent in typical condensed matter systems such as solid states or liquid Helium, is the trap used to confine the atoms, which in theoretical descriptions can be usually assumed to be harmonic. In this thesis, we show that the trap can play an important role for the spin dynamics of ultracold fermions away from the hydrodynamic regime.

Coherent dynamics of large-spin systems has been studied extensively in the case of Bose Einstein condensates and non-condensed Bose gases [4, 36]. This includes spinor dynamics, i.e. dynamics of the population of the components of large-spin BEC [37–39] and thermal Bose gases [40–42] but also spin waves [43, 44]. In the BEC case, such dynamical effects can be well described theoretically using a multi-component Gross-Pitaevskii-Equation [45]. The description of such effects is greatly facilitated because effectively all particles occupy approximately the same spatial mode. In many-body Fermi systems, the Pauli principle necessarily means, that many spatial modes are occupied.

A fundamental motivation to study dynamics of cold atom systems is their capacity to vary single parameters with high accuracy and their good isolation from any environment. This way, one can engineer non-equilibrium states and study e.g. how the system equilibrates over time, a process still not fully understood for closed quantum many-body systems. With the option to manipulate the system with a time-dependent parameter variation, fundamental non-equilibrium situations can be arranged in cold atom systems. One can vary a parameter slowly across a quantum phase transition, e.g. from the ground state of a simple Hamiltonian into a more complex many body state, as a procedure to reliably generate such states [9, 46–49]. Theoretical methods, which work fine at equilibrium, are often not valid anymore to describe this situation [27].

Such a phase transition is believed to be described by a quantum mechanical version of the Kibble-Zurek-Mechanism [26]. The Kibble-Zurek-Mechanism is originally a classical concept [50, 51], where temperature is the parameter that drives the phase transition. As the system approaches a critical point, its relaxation time diverges (critical freezing) and it cannot adiabatically follow the parameter, regardless of how slow it is changed. The change in the Hamiltonian while the system is frozen will lead to the formation of defects. Also, sudden quenches induced by rapid parameter variations are possible, an example featured in this thesis would be instantaneously switching off a magnetic gradient thus changing the symmetry of the system. The reaction of a system to such a rapid quench might manifest in different behavior on several time-scales.

Beyond that, the tunable influence of symmetries and nearly conserved quantities can be used to create situations, where the system first approaches an approximately steady state, which is not the true equilibrium, before it eventually thermalizes, a process known as prethermalization [28, 29, 52].

These cases are very difficult to address using "exact" theoretical many-body methods. For instance, the Quantum Monte Carlo method does not model dynamics and other well known techniques such as density matrix renormalization group (DMRG) [53, 54] and time-evolving block decimation (TEBD) [55] become unstable at long times due to the linear growth of block entropy and works. Moreover, they can only describe 1D systems effectively. These examples make it necessary to study non-equilibrium dynamics in quantum many-body systems in combination with cold atom or ion experiments and simpler, approximate methods, which give guidance also for longer times [27]. In this thesis, we develop and apply such an approximate method.

In our approach, we treat he single-particle dynamics as an open system in an environment, which is given by the other particles. Interactions are taken into account as binary collisions and separated into the dominating forward scattering and the smaller non-forward contribution. This leads to a kinetic Boltzmann equation with full spin coherence, where the forward scattering leads to a coherent mean-field modification of the external fields and non-forward collisions produce an incoherent collision integral, which acts dissipatively on the level of single-particle dynamics. With this approach we can address weakly interacting system in the collisionless regime, where incoherent collisions are negligible and coherent dynamics such as collective excitations and spin oscillations with long lifetimes prevail. We can also explore the intermediate range between the collisionless and the hydrodynamics regimes. While in the hydrodynamic regime, strong collisions ensure local equilibrium and quantities such as temperature, density, magnetization or velocity are functions of position only, this simplification is not valid in the intermediate regime. We can address a situation, where, due to differences in scattering lengths, the system may be hydrodynamic with respect to some collision processes, but not others. This is unique to large-spin systems without SU(N) symmetry, where several scattering lengths are present and e.g. spin-changing collisions whose scattering cross section depends on differences of scattering lengths are much weaker than spin-conserving collisions. In this thesis, our method is applied to experiments performed in the experimental group of Klaus Sengstock in Hamburg featuring ultracold ^{40}K with spin 9/2 and shows good agreement.

This thesis is divided in two parts. Part I outlines the main methods derived and implemented in this thesis, in part II we apply these methods to describe large-spin spin dynamics of trapped Fermi gases. In chapter 3, we first formulate the Hamiltonian of the system we consider throughout this thesis. We introduce the concept of the reduced single-particle density matrix and its phase-space representation, the Wigner quasi-probability distribution function. Towards the end of the chapter, we derive a kinetic equation that describes the time-evolution of the system in terms of the Wigner-function. In this derivation, we employ a mean-field Hartree-Fock approximation and a semi-classical equation for the phase-space variables, while we keep the full quantum description of the spin.

In the subsequent chapter 4, we derive the above mentioned Boltzmann method, which describes interactions beyond the mean field level and generated the mean-field equation of chapter 3 as a special case. In the Boltzmann method, we start from binary low-energy collisions of particles with spin, where the change of the two-body density matrix can be described by the Heisenberg S-matrix. The description is then reduced by tracing over the second particle and keeping quantum statistics and particle indistinguishability into account. We find that this approach leads to a full Boltzmann equation with a collision term. We find that mean-field equation of chapter 3 corresponds to the forward scattering part from the S-matrix, while the non-forward contribution leads to a collision term, which acts dissipatively on the single-particle level.

Chapter 5 is devoted to the different geometries of ultracold atom systems, which we later describe with our theory. First, while in the previous chapter we derived everything for the most general 3D case, we repeat the calculation for 1D systems, which can be achieved in certain experimental setups by applying a very tight confinement to two dimensions, such that all particles occupy the lowest radial mode, even in the case of Fermions. Here of note is that in the mean-field case, only the scattering lengths are rescaled, while for the Boltzmann equation the momentum dependence of the collision integral is different.

Then we investigate the case of a strong harmonic confinement, where the trap oscillation frequency is faster than all relevant internal (interaction induced) dynamics of the system. In this case, we can formulate a time-averaged equation of motion, in which the dynamically induced interaction appear as long-range, despite being induced only by contact interactions. This effective interaction can allow us to completely integrate out the phase-space part of the equations in one or more dimensions. This will allow us to justify a further approximation needed for the treatment of 3D systems. We can reduce the effective dimension of the system, in a sense that kinetic motion is not frozen out in tightly confined directions, but averaged out by rapid oscillations in the trap, such that all relevant dynamics appear along the less confined axes. In the case of a tight trap in all directions, we derive an extremely simplified model for spinor dynamics similar to a single-mode-approximation employed for spinor BEC.

In chapter 7, we illustrate the effect of the dynamically induced long-range interaction in a strongly trapped spin $1/2$ system in one dimension. We simulate the dynamics of a situation, where initially all atoms are perfectly spin polarized, and hence non-interacting and in equilibrium. A rapid quench, induced by a short pulse of a magnetic field gradient then creates a spiral configuration of spins, with spins polarized in the x-y-plane, but in different directions depending on their position. This configuration is then suddenly interacting and far from equilibrium. We show how two domains of magnetization along the z-axis emerge over time and study the dependence of this effect on parameters. We find that always two domains of positive and negative magnetization form, irrespective of the number of windings or domains in the x-y-plane of the initial spin spiral. We show that this effect is a result of dynamically induced long-range interactions.

In the following chapters, we present results obtained in collaboration with the experimental group of Klaus Sengstock in Hamburg, who run an experiment using ultracold ^{40}K, a fermionic species with spin 9/2. In the first joint project, laid out in chapter 8, we perform the first study of spin waves in a large-spin Fermi gas. Through careful preparation, we prohibit population of other components and create an effective spin 3/2 gas. This gas is then prepared in a superposition of its four spin states and a short magnetic field gradient is applied, to initialize the spin waves. These collective excitations are characterized by oscillatory motion (breathing, sloshing) of spin-components in the trap, while the total density distribution remains constant at all times. To reproduce the oscillation frequencies and amplitudes, we derive a linearized mean-field equation and obtain good agreement with the experiment. We categorize the spin wave excitations by expanding the spin state into its scalar, dipole, nematic and octupole components, which shows why some spin waves are excited easily while others appear only in subleading order.

In chapter 9, we study long-lived and large-amplitude spin oscillations of a large-spin Fermi sea. In the experiment it is observed that the system of ^{40}K, now featuring all 10 spin states, exhibits coherent spin-changing dynamics on the time scale of several seconds. Even more fascinating, all atoms in the trap change their spin collectively, at first completely unexpected for a Fermi gas where particles occupy different spatial modes. We identify this effect as a result of the harmonic trap, whose frequencies in all three directions are higher than the observed frequency of the spin oscillations. We can apply our results from chapter 5 on the dynamically induced long-range interaction and show that in this setup it preserves the spatial structure of all spin components and fully suppresses spatial dephasing expected from a multimode Fermi system. With this, we reproduce the experimental results in good agreement using a simple single-mode description. We also investigate the effect of incoherent scattering processes, which are responsible for the eventual damping of the giant spin oscillations. With this knowledge we are able to understand another fascinating effect. If the system is prepared in a magnetically excited spin configuration, small fluctuations induce an instability and drive it out of this configuration into long-lived oscillations. While this mean-field effect is expected to get stronger with increased density, above a certain density the system actually stabilizes, because the rate of incoherent collisions exceeds the coherent dynamics and projects the system back onto its initial state, as in the quantum Zeno effect.

In chapter 10, we continue the investigation of spin-changing dynamics in the spin 9/2 system of Potassium. Here, we focus on dynamics on a very long time-scale, where long after coherent spin oscillations are damped out a slow redistribution is observed. By comparing the time evolution of a coherent and an incoherent spin state, we find that this effect is the relaxation of the system towards a stationary state with approximately equal population in all ten spin states. We identify and categorize the scattering processes responsible for the three main dynamical effects: spin oscillations, their damping and long-time redistribution. While oscillations are driven by forward spin-changing collisions, damping is caused by non-forward spin-conserving collisions, which lead to a quasi-thermalization of each two-component $\pm m$ subsystem. The slow redistribution is a result of spin-changing non-forward scattering, the weakest collision process in the system. The difference in time-scale stems from the fact that spin-changing processes depend on differences of scattering lengths, which in ^{40}K are one order of magnitude smaller than the scattering lengths themselves, and that forward scattering has a larger cross-section than lateral processes. We study study the dependence of non-forward spin-changing collisions on density and magnetic field. We use the fact that for large magnetic fields, spin-changing collisions are suppressed to change the character of a two-component subsystem from open (particles can scatter into the other empty states) to closed, and monitor the evolution of the temperature of such a subsystem. We find that a lossy system increases its temperature due to the creation of holes in the Fermi sea.

We close with chapter 11, where we conclude this thesis and provide some outlook on further related problems and possible future research.

This thesis is based on the following publications [56–59]:

1. **U. Ebling**, A. Eckardt, and M. Lewenstein:
   Spin segregation via dynamically induced long-range interactions in a system of ultracold fermions. Phys. Rev. A **84**, 063607 (2011):
   Chapters 3, 5, 6 and 7.

2. J. Heinze, J. S. Krauser, N. Fläschner, K. Sengstock, C. Becker,
   U. Ebling, A. Eckardt, and M. Lewenstein:
   Engineering spin-waves in a high-spin ultracold Fermi gas. Phys. Rev. Lett. **110**, 250402 (2013):
   Chapters 3, 6 and 8.

3. J. S. Krauser, **U. Ebling**, N. Fläschner, J. Heinze, K. Sengstock, M. Lewenstein, A. Eckardt, and C. Becker:
   Giant spin oscillations in an ultracold Fermi sea. Science **343**, 157 (2014):
   Chapters 3, 6 and 9.

4. **U. Ebling**, J. S. Krauser, N. Fläschner, K. Sengstock, C. Becker, M. Lewenstein, and A. Eckardt:
   Relaxation dynamics of an isolated large-spin Fermi gas far from equilibrium. Phys. Rev. X **4**, 021011 (2014):
   Chapters 4, 5, 6 and 10.

Part I

Methods

Chapter 2

Large spin Fermi system

This chapter serves to prepare the reader for the subsequent parts of this thesis. We first give a short overview of the ideal Fermi gas in a harmonic trap and introduce a few basic concepts, most importantly the Fermi energy and equilibrium distributions of a non-interacting gas of fermions. In the second section, we derive the Hamiltonian of the weakly-interacting large-spin trapped Fermi gas we consider throughout this thesis and conclude with a few remarks on spin-dependent interactions. For a far more detailed overview of Fermi gases, we refer to [60] and [61], on which the first section of this chapter is based.

2.1 Some basics of the trapped ideal Fermi gas

To introduce some basic concepts, we consider a gas of N non-interacting identical Fermions of mass M in a harmonic trap, described by the potential

$$V^{\text{trap}}(\vec{x}) = \frac{M}{2}\left(\omega_x^2 x^2 + \omega_y^2 y^2 + \omega_z^2 z^2\right). \tag{2.1}$$

Since two identical Fermions cannot occupy the same mode of this harmonic oscillator, for a large value of N we can assume, that many modes single-particle modes in all directions are occupied. For Fermions, the average occupation number for an energy eigenstate i is given by the Fermi-Dirac distribution (see e.g. [62])

$$n(E_i) = \frac{1}{\mathrm{e}^{(E_i-\mu)/k_{\mathrm{B}}T} + 1}, \tag{2.2}$$

where k_{B} denotes the Boltzmann constant, T the system temperature and μ is the chemical potential. We consider very large particle numbers and occupation of many modes, where wave-lengths are short compared to the extension of the trap. Then we can apply local density approximation and substitute E_i with the local single-particle energy density [61], such that we obtain the (equilibrium) distribution

$$f(\vec{x},\vec{p}) = \frac{1}{(2\pi\hbar)^3}\frac{1}{\exp\left(\frac{1}{k_{\mathrm{B}}T}\left[\frac{\vec{p}^2}{2M} + V^{\text{trap}}(\vec{x}) - \mu\right]\right) + 1}. \tag{2.3}$$

The chemical potential μ is defined by the condition

$$N = \int d^3x \int d^3p f(\vec{x}, \vec{p}) \tag{2.4}$$

and the temperature T by

$$E = \int d^3x \int d^3p \left[\frac{\vec{p}^2}{2M} + V^{\text{trap}}(\vec{x}) - \mu \right] f(\vec{x}, \vec{p}). \tag{2.5}$$

The chemical potential at $T = 0$ is called the Fermi energy E_{F} and corresponds to the energy of the highest single-particle mode occupied at $T = 0$. We obtain it from solving (2.4) at zero temperature:

$$E_{\text{F}} = (6N)^{1/3} \hbar \bar{\omega}, \tag{2.6}$$

where we have introduced the average trapping frequency $\bar{\omega} = (\omega_x \omega_y \omega_z)^{1/3}$.

In this thesis, we also treat 1D systems very extensively (see e.g. chapter 7). In a 1D system, two frequencies of the harmonic trap (2.1 are so large, that only modes corresponding to the lowest frequency (without loss of generality $\omega_x \equiv \omega$) are macroscopically occupied, while in the transversal directions y, z all particles occupy the ground state. In this case, motion in along y, z is effectively frozen out and we can treat the system in one dimension only. The trap is then given by

$$V^{\text{trap}}(x) = \frac{M}{2} \omega^2 x^2, \tag{2.7}$$

and the distribution function by

$$f(x, p) = \frac{1}{2\pi\hbar} \frac{1}{\exp\left(\frac{1}{k_{\text{B}} T} \left[\frac{p^2}{2M} + V^{\text{trap}}(x) - \mu \right] \right) + 1}, \tag{2.8}$$

where now $p_x \equiv p$. The chemical potential is now fixed by

$$N = \int dx \int dp f(x, p), \tag{2.9}$$

and the dependence of the Fermi energy on the particle number is different:

$$E_{\text{F}} = N \hbar \omega, \tag{2.10}$$

it is now proportional to N.

2.2 Hamiltonian of a large-spin Fermi gas

In this section, we introduce spin, external magnetic fields and spin-dependent interactions to the picture. We use a second-quantized description, in which the single-particle state of an atom is described by a field operator $\hat{\psi}_m(\vec{r})$, where m indicates the magnetic quantum number $m = -F, -F+1, \ldots, F$ and F the total spin of the atom, defined by nuclear spin, electron spin and electronic angular momentum. Throughout this thesis, if a summation appears without specified delimiter, it denotes a summation over all values of the magnetic quantum number. For a Fermi gas, F and m are half-integers and the field operators fulfill the anticommutation relations $\left\{\hat{\psi}_m(\vec{x}), \hat{\psi}_n^\dagger(\vec{y})\right\} = \delta(\vec{x}-\vec{y})\delta_{mn}$. In terms of these operators, the Hamiltonian describing our system consists of two parts, $\hat{H} = \hat{H}_0 + \hat{H}_1$, of which the single-particle part is given by

$$\hat{H}_0 = \sum_{mn} \int \mathrm{d}^3x \hat{\psi}_m^\dagger(\vec{x}) \left[-\frac{\hbar^2\nabla^2}{2M}\delta_{mn} + V_{mn}^{\mathrm{ext}}(\vec{x}) \right] \hat{\psi}_n(\vec{x}). \tag{2.11}$$

Here, M denotes the particle mass and $V_{mn}^{\mathrm{ext}}(\vec{x})$ the external fields. Here, we consider the presence of a trapping potential and external magnetic fields, such that we write

$$V_{mn}^{\mathrm{ext}}(\vec{x}) = V^{\mathrm{trap}}(\vec{x})\delta_{mn} + g\mu_B \vec{B}(\vec{x}) \cdot \vec{S}_{mn} + Q(\vec{x})_{mn}. \tag{2.12}$$

The first term denotes the trapping potential, the other terms denote the effect of a magnetic field. The linear Zeeman effect depends on the magnetic field $\vec{B}(\vec{x})$, while $\vec{S}$ denotes the spin operators, μ_B the Bohr magneton and g the gyromagnetic ratio. It depends on the electronic state of the atom considered, as does the explicit form of the non-linear contributions to the Zeeman splitting. For a spin 1/2-system, $Q(\vec{x})_{mn}$ is necessarily zero, while for the case of ^{40}K, we show the explicit level splitting in appendix A. If we assume magnetic fields parallel to the z-axis and the non-linear part to be purely quadratic (for the range of magnetic fields considered in this thesis, this is a good approximation), the potential (2.12) can be written

$$V_{mn}^{\mathrm{ext}}(\vec{x}) = V^{\mathrm{trap}}(\vec{x}) + g\mu_B B(\vec{x}) m + Q(\vec{x}) m^2, \tag{2.13}$$

where Q is a scalar, which we calculate for ^{40}K in appendix A.

We take two-body interactions into account in the interaction Hamiltonian

$$\hat{H}_1 = \frac{1}{2} \sum_{ijkl} \int d^3x \int d^3y V_{ijkl}(\vec{x},\vec{y}) \hat{\psi}_i^\dagger(\vec{x}) \hat{\psi}_k^\dagger(\vec{y}) \hat{\psi}_l(\vec{y}) \hat{\psi}_j(\vec{x}), \tag{2.14}$$

where $V_{ijkl}(\vec{x},\vec{y})$ is the spin-dependent two-body interaction potential, with incoming and outgoing spins $\{i,k\} \to \{j,l\}$. In this thesis, we assume short-range Van-der-Waals interaction between the atoms. In the low-energy regime of elastic scattering in an ultracold gas, the range of the potential can be considered zero when compared to the wavelength of the atoms. Further, at low energies s-wave scattering is the dominant process [62] and we substitute it with a contact interaction described by the potential $V_{ijkl}(\vec{x},\vec{y}) = U_{ijkl}\delta(\vec{x}-\vec{y})$, such that

$$\hat{H}_1 = \frac{1}{2} \sum_{ijkl} \int d^3x U_{ijkl} \hat{\psi}_i^\dagger(\vec{x}) \hat{\psi}_k^\dagger(\vec{x}) \hat{\psi}_l(\vec{x}) \hat{\psi}_j(\vec{x}), \tag{2.15}$$

The coupling constants U_{ijkl} depend on the s-wave scattering lengths relevant for a collision $\{i,k\} \to \{j,l\}$ [63]. S-wave scattering conserves the total spin S of two incoming particles, the total magnetization $M = i+k = j+l$ as well as the total kinetic and Zeeman energy. For Fermions, the antisymmetry of the wave function of two identical particles means s-wave scattering is not possible between fermions in the same spin state (see e.g. [61]). Hence $U_{ijkl} \neq 0$, if $i \neq k$ and $j \neq l$. With S, M being the good quantum numbers in this case of two body scattering, we expand the coupling constants into channels of total spin:

$$U_{ijkl} = \sum_{S=0,2,\ldots}^{2F-1} \sum_{M=-S,-S+1,\ldots}^{S} g_S \langle ik|SM\rangle \langle SM|jl\rangle . \tag{2.16}$$

Here, $\langle F, m_1; F, m_2|S, M\rangle$ denotes the Clebsch-Gordan coefficients for two spins to form total spin S, and throughout this thesis we make use of the short hand notation

$$\langle m_1 m_2|SM\rangle \equiv \langle F, m_1; F, m_2|S, M\rangle,$$

and omit the value of the single spin as we do not investigate mixtures of different atomic species or hyperfine manifolds in this work, where this would be relevant. The coupling constants $g_S = \frac{4\pi\hbar^2}{M} a_S$ are proportional to the s-wave scattering lengths a_S in each total spin channel. We note, that for s-wave scattering, only even values of S are relevant, as the Clebsch-Gordan coefficients are zero for odd S, again due to the symmetry of the wave functions. In the remainder of this thesis, wherever a summation over total spin quantum numbers S, M appears, we will not explicitly write the delimiters, unless they are different from the case in Eq. (2.16). The conservation of magnetization also allows us to neglect the linear Zeeman effect in the single-particle Hamiltonian and (2.13), which is unchanged regardless whether a collision is spin-changing or spin conserving, by going into the Larmor frame, as long as the magnetic field is homogeneous.

As a last remark on Eq. (2.16), we take a short look at the simplest case of large spins, where $F = 3/2$. In this case, U_{ijkl} has only three non-zero values:

$$U_{ijkl} = \begin{cases} -\frac{1}{8}\left(g_0 + g_2\right) \\ -\frac{1}{4} g_2 \\ \frac{1}{4}\left(g_2 - g_0\right) . \end{cases} \tag{2.17}$$

The first two values correspond to spin-conserving collisions $\{i, k\} = \{j, l\}$, the third one to spin-changing collisions $\{i, k\} \neq \{j, l\}$. Without explicitly writing down the values for large spins, we note that in general, the coupling constant for a spin-conserving collision depends on a *sum*, or *average* of scattering lengths, while for spin-changing collisions, it depends on a *difference*. In alkali atoms, scattering lengths are of the same order of magnitude, hence spin-changing collisions are much weaker than spin-conserving ones.

Chapter 3

Method 1: Mean-field approach

In this chapter we present the first of two approaches to derive an equation of motion for a weakly-interacting system of trapped ultracold Fermions with large spin F in a magnetic field. This approach corresponds to a mean-field and semi-classical treatment of the single-particle dynamics of the system and describes the so-called collisionless regime. For $F = 1/2$, this method has been applied to describe spin dynamics in weakly-interacting Fermi systems [64, 65] and also spin-1 noncondensd Bose gases [42], see also chapter 7 in this thesis. Its range of validity will be discussed in the next chapter, where corrections are taken into account to describe systems outside the collisionless regime.

3.1 Wigner function

We describe the motion of the system, described by the Hamiltonian composed of (2.11) and (2.14), in terms of the single-particle density matrix, defined as

$$\rho_{mn}(\vec{x},\vec{y}) = \left\langle \hat{\psi}^\dagger_m(\vec{x})\hat{\psi}_n(\vec{y}) \right\rangle . \tag{3.1}$$

The notation $\langle \ldots \rangle$ here denotes the many-body expectation value of the field operators, defined

$$\left\langle \hat{\psi}_m(\vec{x}) \right\rangle = \mathrm{Tr}\left(\tilde{\rho}\hat{\psi}_m(\vec{x}) \right) , \tag{3.2}$$

where $\tilde{\rho}$ denotes the full many-body density matrix.

The phase-space representation of the single-particle density matrix is obtained by performing a Wigner-transform,

$$W_{mn}(\vec{x},\vec{p}) = \frac{1}{(2\pi\hbar)^3} \int \mathrm{d}^3 y \mathrm{e}^{i\vec{p}\cdot\vec{y}/\hbar} \rho_{mn}(\vec{x}-\vec{y}/2, \vec{x}+\vec{y}/2), \tag{3.3}$$

and the result called the Wigner function[1]. This function is the phase-space representation of the single-particle density matrix. All relevant single-particle quantities can be extracted from it. It is a function of position and momentum and carries two spin

---

[1] For a review on applications of Wigner functions, see [66].

indices m, n. The diagonal elements with respect to spin are the phase-space densities of the $2F+1$ spin-components, the off-diagonals are called *coherences.* The trace $W_0(\vec{x},\vec{p}) = \sum_m W_{mm}(\vec{x},\vec{p})$ returns the total phase-space density. Position and momentum distributions, measured experimentally using in-situ or time-of-flight techniques, are related to the Wigner function by integration along the momentum or position axes respectively:

$$n_{mn}(\vec{x}) = \int d^3p W_{mn}(\vec{x},\vec{p}) \tag{3.4}$$

$$\tilde{n}_{mn}(\vec{p}) = \int d^3x W_{mn}(\vec{x},\vec{p}). \tag{3.5}$$

This amounts to a projection of the Wigner function onto the respective coordinate axis. It is worth noting here, that time-of-flight experiments for finite expansion times enable also projections onto axes diagonal in phase space, from which in return the entire phase-space distribution can be reconstructed via tomography [67]. The Wigner function is normalized to the total number of particles, because of the definitions (3.1) and (3.3), such that

$$\int d^3x \int d^3p \sum_m W_{mm}(\vec{x},\vec{p}) = N. \tag{3.6}$$

The inverse of the Wigner transform maps the Wigner-function back to the position or momentum representation of the single-particle density matrix:

$$\rho_{mn}(\vec{x},\vec{y}) = \int d^3p \mathrm{e}^{\frac{-i\vec{p}\cdot(\vec{x}-\vec{y})}{\hbar}} W_{mn}\left(\tfrac{\vec{x}+\vec{y}}{2},\vec{p}\right), \tag{3.7}$$

$$\tilde{\rho}_{mn}(\vec{p},\vec{q}) = \int d^3x \mathrm{e}^{\frac{-i\vec{x}\cdot(\vec{p}-\vec{q})}{\hbar}} W_{mn}\left(\vec{x},\tfrac{\vec{p}+\vec{q}}{2}\right). \tag{3.8}$$

3.2 Mean-field approximation

We start the derivation of the equation of motion by computing the time evolution of the single-particle density matrix (3.1). The motion of two field operators is governed by the von Neumann equation

$$i\hbar\frac{d}{dt}\left(\hat{\psi}^\dagger_m(\vec{x})\hat{\psi}_n(\vec{y})\right) = \left[\hat{H}, \hat{\psi}^\dagger_m(\vec{x})\hat{\psi}_n(\vec{y})\right]. \tag{3.9}$$

Hence, by taking the many-body expectation value of (3.9), we see that the single-particle density matrix evolves according to

$$i\hbar\frac{\mathrm{d}}{\mathrm{d}t}\rho_{mn}(\vec{x},\vec{y}) = \left\langle\left[\hat{H}, \hat{\psi}^\dagger_m(\vec{x})\hat{\psi}_n(\vec{y})\right]\right\rangle. \tag{3.10}$$

The evaluation of the commutator in this equation contains commutators of field operators of the form $[\hat{\psi}^\dagger_m\hat{\psi}_n, \hat{\psi}^\dagger_i\hat{\psi}_j]$ and $[\hat{\psi}^\dagger_m\hat{\psi}_n, \hat{\psi}^\dagger_i\hat{\psi}^\dagger_k\hat{\psi}_j\hat{\psi}_l]$. They reduce to the following expressions:

$$\begin{aligned}\left[\hat{\psi}^\dagger_m(\vec{x})\hat{\psi}_n(\vec{y}),\hat{\psi}^\dagger_i(\vec{r})\hat{\psi}_j(\vec{r})\right] &= \delta_{in}\delta(\vec{y}-\vec{r})\hat{\psi}^\dagger_m(\vec{x})\hat{\psi}_j(\vec{r})\\ &\quad -\delta_{mj}\delta(\vec{x}-\vec{r})\hat{\psi}^\dagger_i(\vec{r})\hat{\psi}_n(\vec{y}),\end{aligned} \tag{3.11}$$

$$\begin{aligned}\left[\hat{\psi}^\dagger_m(\vec{x})\hat{\psi}_n(\vec{y}),\hat{\psi}^\dagger_i(\vec{r})\hat{\psi}^\dagger_k(\vec{r})\hat{\psi}_j(\vec{r})\hat{\psi}_l(\vec{r})\right] &= \delta_{in}\delta(\vec{y}-\vec{r})\hat{\psi}^\dagger_m(\vec{x})\hat{\psi}^\dagger_k(\vec{r})\hat{\psi}_j(\vec{r})\hat{\psi}_l(\vec{r})\\ &\quad - \delta_{kn}\delta(\vec{y}-\vec{r})\hat{\psi}^\dagger_m(\vec{x})\hat{\psi}^\dagger_i(\vec{r})\hat{\psi}_j(\vec{r})\hat{\psi}_l(\vec{r})\\ &\quad + \delta_{jm}\delta(\vec{x}-\vec{r})\hat{\psi}^\dagger_i(\vec{r})\hat{\psi}^\dagger_k(\vec{r})\hat{\psi}_l(\vec{r})\hat{\psi}_n(\vec{y})\\ &\quad - \delta_{ml}\delta(\vec{x}-\vec{r})\hat{\psi}^\dagger_i(\vec{r})\hat{\psi}^\dagger_k(\vec{r})\hat{\psi}_j(\vec{r})\hat{\psi}_n(\vec{y}).\end{aligned} \tag{3.12}$$

Consequently, we obtain for the single-particle part of the commutator inside the brackets on the r.h.s. of (3.10)

$$\begin{aligned}\left[\hat{H}_0,\hat{\psi}^\dagger_m(\vec{x})\hat{\psi}_n(\vec{y})\right] = \sum_k \Bigg[&\left(-\frac{\hbar^2\nabla_y^2}{2M}\delta_{kn}+V^{\mathrm{ext}}_{nk}(\vec{y})\right)\hat{\psi}^\dagger_m(\vec{x})\hat{\psi}_k(\vec{y})\\ &-\left(-\frac{\hbar^2\nabla_x^2}{2M}\delta_{kn}+V^{\mathrm{ext}}_{kn}(\vec{x})\right)\hat{\psi}^\dagger_k(\vec{x})\hat{\psi}_n(\vec{y})\Bigg],\end{aligned} \tag{3.13}$$

while the interaction terms are given by

$$\begin{aligned}\left[\hat{H}_1,\hat{\psi}^\dagger_m(\vec{x})\hat{\psi}_n(\vec{y})\right] = \frac{1}{2}\sum_{jkl}\Big[&\left(U_{njkl}-U_{kjnl}\right)\hat{\psi}^\dagger_m(\vec{x})\hat{\psi}^\dagger_k(\vec{y})\hat{\psi}_j(\vec{y})\hat{\psi}_l(\vec{y})\\ &+\left(U_{imkj}-U_{ijkm}\right)\hat{\psi}^\dagger_i(\vec{x})\hat{\psi}^\dagger_k(\vec{x})\hat{\psi}_j(\vec{x})\hat{\psi}_n(\vec{y})\Big].\end{aligned} \tag{3.14}$$

When taking the expectation value of these terms, as prescribed in (3.10), we encounter quartic expectation values in the interaction term (3.14). We decompose them as

$$\langle\hat{\psi}^\dagger_k\hat{\psi}^\dagger_l\hat{\psi}_m\hat{\psi}_n\rangle \approx \langle\hat{\psi}^\dagger_k\hat{\psi}_n\rangle\langle\hat{\psi}^\dagger_l\hat{\psi}_m\rangle - \langle\hat{\psi}^\dagger_k\hat{\psi}_m\rangle\langle\hat{\psi}^\dagger_l\hat{\psi}_n\rangle, \tag{3.15}$$

such that we obtain a closed equation for only the single-particle density matrix. This application of a Wick decomposition is exact for Gaussian states, i.e. equilibrium states of a quadratic Hamiltonian and more broadly corresponds to a time-dependent Hartree-Fock, or mean-field approximation suitable for weak interactions. In the next chapter, we will give a more detailed estimate of its validity. The resulting equation for the time evolution of the single-particle density matrix is given by

$$\begin{aligned}i\hbar\frac{\mathrm{d}}{\mathrm{d}t}\rho_{mn}(\vec{x},\vec{y}) = \sum_k \Bigg[&\left(-\frac{\hbar^2\nabla_y^2}{2M}\delta_{kn}+V_{kn}(\vec{y})\right)\rho_{mk}(\vec{x},\vec{y})\\ &-\left(-\frac{\hbar^2\nabla_x^2}{2M}\delta_{mk}+V_{mk}(\vec{x})\right)\rho_{kn}(\vec{x},\vec{y})\Bigg].\end{aligned} \tag{3.16}$$

Here, we have combined the external potential, magnetic field with a mean-field potential, which formally reads $V^{\mathrm{mf}}_{mn}(\vec{x}) = \sum_{kl}(U_{klnm} - U_{kmnl})\rho_{kl}(\vec{x},\vec{x})$ and arises from the interaction Hamiltonian. Due to the definition of coupling constants (2.16), they are antisymmetric in the fermionic case: $U_{klmn} - U_{knml} = 2U_{klmn}$, such that

$$V^{\mathrm{mf}}_{mn}(\vec{x}) = 2\sum_{kl} U_{klnm}\rho_{kl}(\vec{x},\vec{x}). \tag{3.17}$$

The the total effective potential in Eq. (3.16) reads

$$V_{mn}(\vec{x}) = V^{\mathrm{ext}}_{mn}(\vec{x}) + V^{\mathrm{mf}}_{mn}(\vec{x}). \tag{3.18}$$

Our next step is to transform Eq. (3.16) into the phase-space representation using the Wigner transform (3.3) and obtain

$$\begin{aligned} &i\hbar\frac{\mathrm{d}}{\mathrm{d}t}W_{mn}(\vec{x},\vec{p}) + \frac{i\hbar}{M}\vec{p}\cdot\nabla_x W_{mn}(\vec{x},\vec{p}) = \\ &\sum_k\sum_{l=0}^{\infty}\frac{1}{l!}\left(\left[-\frac{i\hbar}{2}\nabla_y\cdot\nabla_p\right]^l V_{kn}(\vec{y})\Big|_{\vec{y}=\vec{x}} W_{mk}(\vec{x},\vec{p}) - \left[\frac{i\hbar}{2}\nabla_y\cdot\nabla_p\right]^l V_{mk}(\vec{y})\Big|_{\vec{y}=\vec{x}} W_{kn}(\vec{x},\vec{p})\right). \end{aligned} \tag{3.19}$$

In this representation, the mean-field potential is given by

$$V^{\mathrm{mf}}_{mn}(\vec{x}) = 2\sum_{kl}\int d^3p U_{klnm}W_{kl}(\vec{x},\vec{p}). \tag{3.20}$$

Equation (3.19) is an infinite expansion in terms of gradients of the Wigner function and potentials. It looks very similar to a Quantum-Liouville-Equation (QLE), the equation of motion for a single spinless particle in phase space in a potential $V(\vec{x})$ [68]. However, here, the expansion contains terms for all values of l, whereas in the QLE, only odd terms appear. This is a consequence of spin. In our case, the Wigner function and potential are not numbers but matrices of size $(2F+1)\times(2F+1)$. The even terms in (3.19) have the shape of commutators, which are obviously zero for numbers, but not necessarily for matrices. The most striking feature here is the appearance of a term for $l = 0$, without gradients and of lower order than the usual terms in the QLE. This term can only appear in a system with spin, and being of lowest order, should have a very large impact on the dynamics.

The Fermi statistics enters Eq. (3.19) twofold. First, the mean-field potential and interactions contained in it obey a fermionic symmetry, inherent in the properties of the Clebsch-Gordan coefficients for half-integer spins. Second, the single-particle Wigner function is not completely free. The definition of single-particle density matrix as a many-body expectation value (3.1) depends on the full many-body density matrix, which must represent a fermionic state here [2].

---

[2] The same derivation can be done for Bosons as well, as long as they are not condensed. Then the same considerations would apply: Interactions must have bosonic symmetry and the Wigner function must be restricted to bosonic states.

3.3 Semi-classical approximation

If we consider Eq. (3.19) for the non-interacting case (i.e. $U_{ijkl} = 0$), we notice that in the typical case of a harmonic trapping potential $V^{\text{trap}}(\vec{x}) = \frac{M}{2}\left(\omega_x^2 x^2 + \omega_y^2 y^2 + \omega_z^2 z^2\right)$, the gradient expansion automatically ends at $l = 1$ due to the absence of higher derivatives. We now employ a further *semi-classical* approximation of Eq. (3.19) and truncate the sum at $l = 1$ as well for the interacting case. This approximation is valid for anharmonic potentials, if the potential varies slowly compared to the single-particle wavelengths in the system, here the thermal wavelength $\lambda_T = 2\pi\hbar/\sqrt{3Mk_\text{B}T}$ at higher temperatures or the Fermi wavelength $\lambda_\text{F} = 2\pi\hbar/\sqrt{2ME_\text{F}}$ in colder systems.

The truncated equation of motion now reads

$$\begin{aligned}\frac{\mathrm{d}}{\mathrm{d}t}W_{mn}(\vec{x},\vec{p}) + \frac{\vec{p}}{M}\cdot\nabla_x W_{mn}(\vec{x},\vec{p}) &= \frac{i}{\hbar}\sum_k \left[V_{mk}(\vec{x})W_{kn}(\vec{x},\vec{p}) - W_{mk}(\vec{x},\vec{p})V_{kn}(\vec{x})\right] \\ &+ \sum_k \left\{\nabla_x V_{mk}(\vec{x})\cdot\nabla_p W_{kn}(\vec{x},\vec{p}) + \nabla_p W_{mk}(\vec{x},\vec{p})\cdot\nabla_x V_{kn}(\vec{x})\right\}, \qquad (3.21)\end{aligned}$$

or alternatively, if we change the notation from indices denoting matrix elements to phase-space dependent matrices

$$\frac{\mathrm{d}}{\mathrm{d}t}\hat{W}(\vec{x},\vec{p}) + \frac{\vec{p}}{M}\cdot\nabla_x\hat{W}(\vec{x},\vec{p}) = \frac{i}{\hbar}\left[\hat{V}(\vec{x}),\hat{W}(\vec{x},\vec{p})\right] + \frac{1}{2}\left\{\nabla_x\hat{V}(\vec{x}),\nabla_p\hat{W}(\vec{x},\vec{p})\right\}. \qquad (3.22)$$

This equation consists of four expressions. The second term on the left hand side is the free drift term of the particles, obtained from the kinetic energy part of the Hamiltonian. The leading order in the semi-classical expansion is the commutator $[\cdot,\cdot]$, it drives coherent spin dynamics through the interplay of scattering and magnetic field. This term only contains spin-dependent effects and is absent in the spinless case. The anticommutator $\{\cdot,\cdot\}$ is a force term resulting from both the external potential, inhomogeneities in the magnetic field and the mean field. The semi-classical nature of (3.22) and its derivation reveals itself in these expressions. Both the kinetic drift term and the force term are essentially expressions known from the classical Liouville equation. We note that these terms do not contain $\hbar$ here, which appears only in the commutator and would appear in higher order terms. Also, we recall that our semi-classical approximation only affects the phase-space variables, we kept the full quantum description of the spin. This results in the appearance of the commutator, which as a result is a quantum term, that is expected to have a strong impact on the system dynamics, as it appears at *lower* order than the classical (anticommutator) terms.

Chapter 4

Method 2: Collision approach

The second theoretical method in this thesis involves the derivation of a Boltzmann equation with full spin coherence and an explicit collision term. Previous work originating in the 1980s for the description of spin-waves in liquid Helium and Hydrogen [69–73], pioneered by Lhuillier and Laloë produced an intuitive approach to derive a Boltzmann equation from microscopic two-body collision processes [74–76]. This method, called the *Lhuillier-Laloë transport equation*, was later applied successfully to describe spin segregation in a cold spin 1/2 Fermi gas of ^{6}Li [64, 77]. In this chapter, we will generalize this method to larger spins and spin-changing collisions in the presence of a quadratic Zeeman effect, while in chapter 5, we also extend it to systems in a 1D geometry, where the collision term has a different momentum dependence.

This method describes the single-particle dynamics as an open system, where the other particles take the role of the bath. This makes some parts of the dynamics appear as dissipative on the single-particle level, which is not the case in the mean-field description, which is fully coherent. We will show, that the processes responsible for this dissipative dynamics are non-forward collisions, which become more relevant for stronger interactions and higher densities, where the system leaves the collisionless and approaches the hydrodynamic regime. Hence, this approach is required to describe experiments in the intermediate regime, where incoherent effects such as damping of spin oscillations are observed [58].

The Lhuillier-Laloë method features an expansion in scattering lengths for weak interaction and a remarkable feature of it is that in lowest order it reproduces the mean-field result obtained in the preceding chapter. This means, that it helps us better understand the limitations and validity of mean-field theory. Further, this approach is derived from microscopic equations of motion and does not require phenomenological assumptions. It does not require prior knowledge of the equilibrium state, whose determination is a very challenging effort in systems with high spin. From the viewpoint of doing numerical simulations, this allows us to build on existing code used to solve the mean-field equation of motion (3.22) instead of producing a completely new implementation. This chapter is based on Ref. [59].

4.1 Microscopic derivation of the collision integral

A general form of a Boltzmann equation describes the time-evolution of the single-particle density operator $\hat{\rho}$ in the following form:

$$\frac{d}{dt}\hat{\rho} - \frac{1}{i\hbar}\left[\hat{\rho}, \hat{H}_0\right] = I_{\text{coll}}[\hat{\rho}]. \tag{4.1}$$

The free motion of the particle in the trap is on the l.h.s., where $\hat{H}_0$ denotes the single-particle Hamiltonian (2.11), which contains kinetic energy, trap and magnetic fields. All effects of interactions are contained in the term on the r.h.s, called the *collision integral* or *collision term*, in whose derivation the appropriate approximations have to be employed, such that it only depends on the single particle density itself. In this and the following sections we derive an explicit expression for $I_{\text{coll}}[\hat{\rho}]$.

The idea behind the approach of Lhuillier-Laloë is to interpret the collision integral as the change rate of the single-particle density operator due to binary collisions,

$$I_{\text{coll}} = \frac{\hat{\rho}' - \hat{\rho}}{\Delta t}, \tag{4.2}$$

in a short time interval Δt, which nevertheless is longer than the duration of a collision, that is thus considered to be effectively instantaneous. Here we denote by $\hat{\rho}$ the state of a single particle before the collision and by $\hat{\rho}'$ the state after the collision. With this assumption, collisions are treated in the asymptotic limit, with incoming particles coming from $t = -\infty$ and going to $t = +\infty$, neglecting the state of particles during the collision process. In this limit, collisions can be described by the Heisenberg S-matrix. This matrix relates the *two-body* density matrices $\hat{\rho}(1, 2)$ before and after the collision

$$\hat{\rho}(1, 2)' = \hat{S}\hat{\rho}(1, 2)\hat{S}^{\dagger}, \tag{4.3}$$

where "1" and "2" denote the orbital and spin degree of freedom of particles 1 and 2: $(\vec{x}_1, \vec{y}_1, m_1, n_1)$ and $(\vec{x}_2, \vec{y}_2, m_2, n_2)$, which for now are treated as distinguishable. In terms of field operators, the elements of this two-body density matrix are defined as

$$\left[\hat{\rho}(1, 2)\right]_{m_1,n_1,m_2,n_2}(\vec{x}_1, \vec{y}_1, \vec{x}_2, \vec{y}_2) = \left\langle \hat{\psi}^{\dagger}_{m_1}(\vec{x}_1)\hat{\psi}^{\dagger}_{m_2}(\vec{x}_2)\hat{\psi}_{n_2}(\vec{y}_2)\hat{\psi}_{n_1}(\vec{y}_1)\right\rangle. \tag{4.4}$$

To reduce expression (4.3) to a single-body description, we later trace out particle 2. Another key assumption of this approach is that the particles involved in a collision are uncorrelated, both before and after the collision:

$$\hat{\rho}(1, 2) = \hat{\rho}(1) \otimes \hat{\rho}(2), \tag{4.5}$$

where now $\hat{\rho}(i)$ denotes the single-particle density matrix of particle i.

This assumption is effectively a quantum mechanical version of the molecular chaos hypothesis (Stosszahlansatz) of Boltzmann, here it is justified for a dilute system with a large number of particles. For the single-particle density matrices before and after a collision we obtain

$$\hat{\rho}(1) \approx \frac{1}{2}\mathrm{Tr}_2\{(1-\hat{\mathcal{P}}^{\mathrm{ex}})\hat{\rho}(1)\otimes\hat{\rho}(2)(1-\hat{\mathcal{P}}^{\mathrm{ex}}),\} \tag{4.6}$$

$$\hat{\rho}'(1) \approx \frac{1}{2}\mathrm{Tr}_2\{(1-\hat{\mathcal{P}}^{\mathrm{ex}})\hat{S}\hat{\rho}(1)\otimes\hat{\rho}(2)\hat{S}^{\dagger}(1-\hat{\mathcal{P}}^{\mathrm{ex}})\}, \tag{4.7}$$

where we now treat the particles as indistinguishable and introduce the exchange operator $\hat{P}^{\mathrm{ex}}$, which exchanges the quantum numbers of particles 1 and 2. Due to fermionic statistics, it comes with a minus sign in front. This Ansatz yields the following expression for the collision integral

$$\hat{I}_{\mathrm{coll}} \approx \frac{1}{\Delta t}\mathrm{Tr}_2\left\{\frac{\hat{1}-\hat{\mathcal{P}}^{\mathrm{ex}}}{\sqrt{2}}\hat{S}\hat{\rho}(1)\otimes\hat{\rho}(2)\hat{S}^{\dagger}-\hat{\rho}(1)\otimes\hat{\rho}(2)\frac{\hat{1}-\hat{\mathcal{P}}^{\mathrm{ex}}}{\sqrt{2}}\right\}. \tag{4.8}$$

The scattering S-matrix is related to the transmission T-matrix, $\hat{S} = \hat{1} - 2\pi i\hat{\mathcal{T}}$, such that Eq. (4.8) becomes

$$\begin{aligned}\hat{I}_{\mathrm{coll}} \approx \frac{2\pi}{\Delta t}\mathrm{Tr}_2\Bigg\{\frac{1-\hat{\mathcal{P}}^{\mathrm{ex}}}{\sqrt{2}}&\Big[i\hat{\mathcal{T}}\hat{\rho}(1)\otimes\hat{\rho}(2)-i\hat{\rho}(1)\otimes\hat{\rho}(2)\hat{\mathcal{T}}^{\dagger}\\ &+2\pi\hat{\mathcal{T}}\hat{\rho}(1)\otimes\hat{\rho}(2)\hat{\mathcal{T}}^{\dagger}\Big]\frac{1-\hat{\mathcal{P}}^{\mathrm{ex}}}{\sqrt{2}}\Bigg\}.\end{aligned} \tag{4.9}$$

It consists of two terms with linear dependence in the T-matrix and a quadratic term. As a first step before performing the trace operation we evaluate the expression (4.9) in the two-body phase space representation.

4.2 Two-body Wigner transform

Because the T-matrix depends only on the relative wave vectors, it is convenient to evaluate Eq. (4.9) in the center-of-mass frame. We introduce the standard notation

$$\begin{aligned}\vec{R} &= \frac{1}{2}(\vec{x}_1+\vec{x}_2), \qquad \vec{r} = \vec{x}_1-\vec{x}_2,\\ \vec{P} &= \vec{p}_1+\vec{p}_2, \qquad \vec{p} = \frac{1}{2}(\vec{p}_1-\vec{p}_2),\end{aligned} \tag{4.10}$$

to denote center-of-mass with capital letters $(\vec{R},\vec{P})$ and relative positions and momenta with bare lower case letters $(\vec{r},\vec{p})$, versus the coordinates of particles 1 and 2 denoted by subscript. We use the same notation style for wave vectors, which are related to momenta: $\hbar\vec{K} = \vec{P}$, $\hbar\vec{k} = \vec{p}$ and $\hbar\vec{k}_{1,2} = \vec{p}_{1,2}$.

We denote by $W^{(T,T^2)}$ the two-body Wigner transform of the part of Eq. (4.9) linear in the T-matrix,

$$i\times\frac{1-\hat{\mathcal{P}}^{\mathrm{ex}}}{\sqrt{2}}\left[\hat{\mathcal{T}}\hat{\rho}(1)\otimes\hat{\rho}(2)-\hat{\rho}(1)\otimes\hat{\rho}(2)\hat{\mathcal{T}}^{\dagger}\right]\frac{1-\hat{\mathcal{P}}^{\mathrm{ex}}}{\sqrt{2}}, \tag{4.11}$$

and the quadratic part,

$$\frac{1-\hat{\mathcal{P}}^{\mathrm{ex}}}{\sqrt{2}}\left[\hat{\mathcal{T}}\hat{\rho}(1)\otimes\hat{\rho}(2)\hat{\mathcal{T}}^{\dagger}\right]\frac{1-\hat{\mathcal{P}}^{\mathrm{ex}}}{\sqrt{2}}, \tag{4.12}$$

respectively. First, we take the wave-vector representation of expressions (4.11) and (4.12) in the center-of mass frame,

$$i\langle\vec{K}_+,\vec{k}_+,i,m|\frac{1-\hat{\mathcal{P}}^{\mathrm{ex}}}{\sqrt{2}}\hat{\mathcal{T}}\hat{\rho}(1)\otimes\hat{\rho}(2)\frac{1-\hat{\mathcal{P}}^{\mathrm{ex}}}{\sqrt{2}}|\vec{K}_-,\vec{k}_-,j,n\rangle, \tag{4.13}$$

$$\langle\vec{K}_+,\vec{k}_+,i,m|\frac{1-\hat{\mathcal{P}}^{\mathrm{ex}}}{\sqrt{2}}\hat{\mathcal{T}}\hat{\rho}(1)\otimes\hat{\rho}(2)\hat{\mathcal{T}}^{\dagger}\frac{1-\hat{\mathcal{P}}^{\mathrm{ex}}}{\sqrt{2}}|\vec{K}_-,\vec{k}_-,j,n\rangle, \tag{4.14}$$

where the notation $|\vec{K},\vec{k},m,n\rangle$ denotes a two-particle state, where particle 1 has spin m, particle 2 has spin n, $\vec{K}$ denotes the sum of the wave vectors of both particles and $\vec{k}$ the relative wave vector. We perform a Wigner transform (3.3) from the basis of center-of-mass wave vectors $\vec{K}_\pm,\vec{k}_\pm$ into the corresponding center-of-mass phase space variables (4.10). For this, we substitute $\vec{K}_\pm=\frac{\vec{P}}{\hbar}\pm\frac{\vec{K}}{2}$ and $\vec{k}_\pm=\frac{\vec{p}}{\hbar}\pm\frac{\vec{\kappa}}{2}$ and perform a Fourier transform with respect to $\vec{K},\vec{\kappa}$ to obtain

$$\begin{aligned}W^{T}_{ijmn}(\vec{r},\vec{R},\vec{p},\vec{P}) = {} & \frac{i}{(2\pi\hbar)^6}\int d^3K\int d^3\kappa\,\mathrm{e}^{i\vec{K}\cdot\vec{R}}\mathrm{e}^{i\vec{\kappa}\cdot\vec{r}}\\ & \times\langle\vec{K}_+,\vec{k}_+,i,m|\frac{1-\hat{\mathcal{P}}^{\mathrm{ex}}}{\sqrt{2}}\hat{\mathcal{T}}\hat{\rho}(1)\otimes\hat{\rho}(2)\frac{1-\hat{\mathcal{P}}^{\mathrm{ex}}}{\sqrt{2}}|\vec{K}_-,\vec{k}_-,j,n\rangle+\mathrm{h.c.}\end{aligned} \tag{4.15}$$

$$\begin{aligned}W^{T^2}_{ijmn}(\vec{r},\vec{R},\vec{p},\vec{P}) = {} & \frac{1}{(2\pi\hbar)^6}\int d^3K\int d^3\kappa\,\mathrm{e}^{i\vec{K}\cdot\vec{R}}\mathrm{e}^{i\vec{\kappa}\cdot\vec{r}}\\ & \times\langle\vec{K}_+,\vec{k}_+,i,m|\frac{1-\hat{\mathcal{P}}^{\mathrm{ex}}}{\sqrt{2}}\hat{\mathcal{T}}\hat{\rho}(1)\otimes\hat{\rho}(2)\hat{\mathcal{T}}^{\dagger}\frac{1-\hat{\mathcal{P}}^{\mathrm{ex}}}{\sqrt{2}}|\vec{K}_-,\vec{k}_-,j,n\rangle.\end{aligned} \tag{4.16}$$

Now, we insert two complete bases $\int d^3K_1\int d^3k_1\sum_{ab}|\vec{K}_1,\vec{k}_1,a,b\rangle\langle\vec{K}_1,\vec{k}_1,a,b|$ and $\int d^3K_2\int d^3k_2\sum_{cd}|\vec{K}_2,\vec{k}_2,c,d\rangle\langle\vec{K}_2,\vec{k}_2,c,d|$ to the left and right of the tensor product of density matrices $\rho(1)\otimes\hat{\rho}(2)$. The dependence of the T-matrix on the relative wave-vector only makes the integration over $K_{1,2}$ trivial. For the elements of the T-matrix, we note that collisions conserve total single-particle energy, hence we make the substitution

$$\langle\vec{K}_1,\vec{k}_1,a,b|\hat{\mathcal{T}}|\vec{K}_2,\vec{k}_2,c,d\rangle=\delta\left(\epsilon_{k_1}-\epsilon_{k_2}+Q_{abcd}\right)T_{abcd}(\vec{k}_1,\vec{k}_2) \tag{4.17}$$

in above expressions. The delta function ensures energy conservation, where $\epsilon_{k_{1,2}}=\hbar^2k_{1,2}^2/2\mu$ denotes kinetic energy, $\mu=M/2$ the reduced mass and $Q_{abcd}=Q(a^2+b^2-c^2-d^2)$ the shift in quadratic Zeeman energy (see Eq. 2.13), which is non-zero during a spin-changing collision. This shift is absent in spin 1/2 systems and introduces a situation not accounted for in the original theory, in which the total kinetic energy cannot change during a collision. The term $T_{abcd}(\vec{k}_1, \vec{k}_2)$ is thus defined only for values of spin and wave vector, which ensure energy conservation and hence called the *on-shell T-matrix*. We will provide its explicit expression later in this chapter in section 4.6. With this substitution, we obtain

$$
\begin{aligned}
W^{T}_{ijmn}(\vec{r}, \vec{R}, \vec{p}, \vec{P}) &= \frac{-i}{(2\pi\hbar)^6} \int d^3K \int d^3\kappa \int d^3k_1 \int d^3k_2 \mathrm{e}^{i\vec{K}\cdot\vec{R}} \mathrm{e}^{i\vec{\kappa}\cdot\vec{r}} \\
&\quad \times \sum_{abcd} \langle \vec{K}_+, \vec{k}_+, i, m | \frac{1 - \hat{\mathcal{P}}^{\mathrm{ex}}}{\sqrt{2}} \hat{\mathcal{T}} | \vec{K}_+, \vec{k}_1, a, b \rangle \langle \vec{K}_+, \vec{k}_1, a, b | \hat{\rho}(1) \otimes \hat{\rho}(2) | \vec{K}_-, \vec{k}_2, c, d \rangle \\
&\quad \times \langle \vec{K}_-, \vec{k}_2, c, d | \frac{1 - \hat{\mathcal{P}}^{\mathrm{ex}}}{\sqrt{2}} | \vec{K}_-, \vec{k}_-, j, n \rangle + \text{h.c.} \\
&= \frac{-i}{2(2\pi\hbar)^6} \int d^3K \int d^3\kappa \int d^3k_1 \int d^3k_2 \mathrm{e}^{i\vec{K}\cdot\vec{R}} \mathrm{e}^{i\vec{\kappa}\cdot\vec{r}} \sum_{abcd} \delta(\epsilon_{k_+} - \epsilon_{k_1} + Q_{imab}) \\
&\quad \times \Big(\delta(\vec{k}_2 - \vec{k}_-) \delta_{cj} \delta_{dn} - \delta(\vec{k}_2 + \vec{k}_-) \delta_{nc} \delta_{jd} \Big) \Big(T_{imab}(\vec{k}_+, \vec{k}_1) - T_{miab}(-\vec{k}_+, \vec{k}_1) \Big) \\
&\quad \times \langle \vec{K}_+, \vec{k}_1, a, b | \hat{\rho}(1) \otimes \hat{\rho}(2) | \vec{K}_-, \vec{k}_2, c, d \rangle + \text{h.c.}
\end{aligned} \tag{4.18}
$$

for the linear term and

$$
\begin{aligned}
W^{T^2}_{ijmn}(\vec{r}, \vec{R}, \vec{p}, \vec{P}) &= \frac{1}{2(2\pi\hbar)^6} \int d^3K \int d^3\kappa \int d^3k_1 \int d^3k_2 \mathrm{e}^{i\vec{K}\cdot\vec{R}} \mathrm{e}^{i\vec{\kappa}\cdot\vec{r}} \\
&\quad \times \sum_{abcd} \delta(\epsilon_{\vec{k}_+} - \epsilon_{\vec{k}_1} + Q_{imab}) \delta(\epsilon_{k_2} - \epsilon_{k_-} + Q_{cdjn}) \\
&\quad \times \Big(T_{imab}(\vec{k}_+, \vec{k}_1) - T_{miab}(-\vec{k}_+, \vec{k}_1) \Big) \Big(T^*_{jncd}(\vec{k}_-, \vec{k}_2) - T^*_{njcd}(-\vec{k}_-, \vec{k}_2) \Big) \\
&\quad \times \langle \vec{K}_+, \vec{k}_1, a, b | \hat{\rho}(1) \otimes \hat{\rho}(2) | \vec{K}_-, \vec{k}_2, c, d \rangle
\end{aligned} \tag{4.19}
$$

for the term quadratic in the T-matrix. The elements of the tensor product of density matrices are obtained from the Wigner functions by an inverse two-body Wigner transform

$$
\begin{aligned}
\langle \vec{K}_+, \vec{k}_1, a, b | \hat{\rho}(1) \otimes \hat{\rho}(2) | \vec{K}_-, \vec{k}_2, c, d \rangle &= \hbar^6 \int d^3R' \int d^3r' \mathrm{e}^{-i\vec{K}\cdot\vec{R}'} \mathrm{e}^{i(\vec{k}_2 - \vec{k}_1)\cdot\vec{r}'} \\
&\times W_{ac}(\vec{R}' + \tfrac{\vec{r}'}{2}, \tfrac{\vec{P} + \hbar\vec{k}_1 + \hbar\vec{k}_2}{2}) W_{bd}(\vec{R}' - \tfrac{\vec{r}'}{2}, \tfrac{\vec{P} - \hbar\vec{k}_1 - \vec{k}_2}{2}).
\end{aligned} \tag{4.20}
$$

and we substitute this expression into the terms forming the collision term (4.18) and (4.19). This produces a delta function $\int d^3K \mathrm{e}^{i\vec{K}\cdot(\vec{R} - \vec{R}')} = (2\pi)^3 \delta(\vec{R} - \vec{R}')$ and after carrying out the integrations over $\vec{K}$ and $\vec{R}'$ we obtain

$$\begin{aligned}W^{T}_{ijmn}(\vec{r},\vec{R},\vec{p},\vec{P}) = \frac{-i}{2(2\pi)^3}\int d^3\kappa\int d^3k_1\int d^3k_2\int d^3r'\mathrm{e}^{i\vec{\kappa}\cdot\vec{r}}\mathrm{e}^{i(\vec{k}_2-\vec{k}_1)\cdot\vec{r}'}\\
\times\sum_{abcd}\Big(\delta(\vec{k}_2-\vec{k}_-)\delta_{cj}\delta_{dn}-\delta(\vec{k}_2+\vec{k}_-)\delta_{nc}\delta_{jd}\Big)\\
\times\,\delta(\epsilon_{k_+}-\epsilon_{k_1}+Q_{imab})\Big(T_{imab}(\vec{k}_+,\vec{k}_1)-T_{miab}(-\vec{k}_+,\vec{k}_1)\Big)\\
\times\,W_{ac}(\vec{R}+\tfrac{\vec{r}'}{2},\tfrac{\vec{P}+\hbar\vec{k}_1+\hbar\vec{k}_2}{2})W_{bd}(\vec{R}-\tfrac{\vec{r}'}{2},\tfrac{\vec{P}-\hbar\vec{k}_1-\hbar\vec{k}_2}{2})+\text{h.c.}\end{aligned}\tag{4.21}$$

and

$$\begin{aligned}W^{T^2}_{ijmn}(\vec{r},\vec{R},\vec{p},\vec{P}) = \frac{1}{(2\pi)^3}\int d^3\kappa\int d^3k_1\int d^3k_2\int d^3r'\mathrm{e}^{i\vec{\kappa}\cdot\vec{r}}\mathrm{e}^{i(\vec{k}_2-\vec{k}_1)\cdot\vec{r}'}\\
\times\sum_{abcd}\delta(\epsilon_{k_+}-\epsilon_{k_1}+Q_{imab})\delta(\epsilon_{k_2}-\epsilon_{k_-}+Q_{cdjn})\Big(T_{imab}(\vec{k}_+,\vec{k}_1)-T_{miab}(-\vec{k}_+,\vec{k}_1)\Big)\\
\times\Big(T^*_{jncd}(\vec{k}_-,\vec{k}_2)-T^*_{lncd}(-\vec{k}_-,\vec{k}_2)\Big)\,W_{ac}(\vec{R}+\tfrac{\vec{r}'}{2},\tfrac{\vec{P}+\hbar\vec{k}_1+\hbar\vec{k}_2}{2})W_{bd}(\vec{R}-\tfrac{\vec{r}'}{2},\tfrac{\vec{P}-\hbar\vec{k}_1-\hbar\vec{k}_2}{2}).\end{aligned}\tag{4.22}$$

4.3 Trace over second particle

In order to trace out particle 2 as described in Eq. (4.9) we return from the center-of-mass frame to he lab frame by substituting equations (4.10) back into (4.21) and (4.22. In the representation we use, taking the trace over particle 2 means performing the operation $I^{(T,T^2)}_{ij}(\vec{x}_1,\vec{p}_1)=\frac{1}{\Delta t}\int d^3x_2\int d^3p_2\sum_{mn}\delta_{mn}W^{(T,T^2)}_{ijmn}(\vec{r},\vec{R},\vec{p},\vec{P})$ on each term. Introducing the notations

$$\vec{q}=2\hbar\vec{k},\qquad \vec{p}'_1=\vec{p}_1-\tfrac{\vec{q}-\hbar(\vec{k}_1+\vec{k}_1)}{2},\qquad \vec{p}'_2=\vec{p}_1-\tfrac{\vec{q}+\hbar(\vec{k}_1+\vec{k}_2)}{2},\tag{4.23}$$

we arrive at the following expressions for the collision term:

$$\begin{aligned}I^{T}_{ij}(\vec{x}_1,\vec{p}_1) = \frac{-i}{2(2\pi)^3}\int d^3\kappa\int d^3k_1\int d^3k_2\int d^3r'\int d^3r\int d^3q\mathrm{e}^{i\vec{\kappa}\cdot\vec{r}}\mathrm{e}^{i(\vec{k}_2-\vec{k}_1)\cdot\vec{r}'}\\
\times\sum_{abcdl}\delta(\epsilon_{k_+}-\epsilon_{k_1}+Q_{ilab})\Big(\delta(\vec{k}_2-\vec{k}_-)\delta_{cj}\delta_{dl}-\delta(\vec{k}_2+\vec{k}_-)\delta_{lc}\delta_{jd}\Big)\\
\times\Big(T_{ilab}(\vec{k}_+,\vec{k}_1)-T_{liab}(-\vec{k}_+,\vec{k}_1)\Big)\,W_{ac}(\vec{x}_1-\tfrac{\vec{r}-\vec{r}'}{2},\vec{p}'_1)W_{bd}(\vec{x}_1-\tfrac{\vec{r}+\vec{r}'}{2},\vec{p}'_2)+\text{h.c.}\end{aligned}\tag{4.24}$$

and

$$\begin{aligned}I^{T^2}_{ij}(\vec{x}_1,\vec{p}_1) = \frac{1}{2(2\pi)^3}\int d^3\kappa\int d^3k_1\int d^3k_2\int d^3r'\int d^3r\int d^3q\mathrm{e}^{i\vec{\kappa}\cdot\vec{r}}\mathrm{e}^{i(\vec{k}_2-\vec{k}_1)\cdot\vec{r}'}\\
\times\sum_{abcdl}\delta(\epsilon_{k_+}-\epsilon_{k_1}+Q_{ilab})\delta(\epsilon_{k_2}-\epsilon_{k_-}+Q_{cdjl})\Big(T_{ilab}(\vec{k}_+,\vec{k}_1)-T_{liab}(-\vec{k}_+,\vec{k}_1)\Big)\\
\times\Big(T^*_{jlcd}(\vec{k}_-,\vec{k}_2)-T^*_{ljcd}(-\vec{k}_-,\vec{k}_2)\Big)\,W_{ac}(\vec{x}_1-\tfrac{\vec{r}-\vec{r}'}{2},\vec{p}'_1)W_{bd}(\vec{x}_1-\tfrac{\vec{r}+\vec{r}'}{2},\vec{p}'_2).\end{aligned}\tag{4.25}$$

4.4 Semi-classical gradient expansion

In order to further simplify the expressions above we assume the Wigner function to vary only slowly in space compared to single-particle wave-functions. This assumption means that local contributions to the collision term dominate and we perform a Taylor expansion for the spatial coordinate

$$W_{ij}(\vec{x}_1 - \tfrac{\vec{r}\pm\vec{r}'}{2}, \vec{p}) = W_{ij}(\vec{x}_1, \vec{p}) - \tfrac{\vec{r}\pm\vec{r}'}{2} \cdot \nabla_{\vec{x}_1} W_{ij}(\vec{x}_1, \vec{p}) + \ldots, \tag{4.26}$$

therefore the expansion of the product of Wigner functions in (4.24) and (4.25) reads

$$\begin{aligned} W_{ac}(\vec{x}_1 - \tfrac{\vec{r}-\vec{r}'}{2}, \vec{p}_1')W_{bd}(\vec{x}_1 - \tfrac{\vec{r}+\vec{r}'}{2}, \vec{p}_2') &= W_{ac}(\vec{x}_1, \vec{p}_1')W_{bd}(\vec{x}_1, \vec{p}_2') \\ -\tfrac{\vec{r}}{2} \cdot \nabla_{\vec{x}_1}\left(W_{ac}(\vec{x}_1, \vec{p}_1')W_{bd}(\vec{x}_1, \vec{p}_2')\right) &+ \tfrac{\vec{r}'}{2} W_{bd}(\vec{x}_1, \vec{p}_2') \cdot \nabla_{\vec{x}_1} W_{ac}(\vec{x}_1, \vec{p}_1') \\ &- \tfrac{\vec{r}'}{2} W_{ac}(\vec{x}_1, \vec{p}_1') \cdot \nabla_{\vec{x}_1} W_{bd}(\vec{x}_1, \vec{p}_2') + \ldots \end{aligned} \tag{4.27}$$

Together with the expansion of the T-matrix above we must be careful to expand the collision term in two small parameters in a meaningful way. One small parameter is the coupling constant proportional to the s-wave scattering length. The other one is related to the gradient expansion. Its magnitude is determined by the Fermi or thermal wavelength compared to the spatial variation of the Wigner function and the trap, which determines the system size. We expand the collision term to quadratic order in scattering lengths a_S. This means we will obtain terms linear in a_S from $I^T_{ij}(\vec{x}, \vec{p})$ and quadratic terms from $I^T_{ij}(\vec{x}, \vec{p})$ and $I^{T^2}_{ij}(\vec{x}, \vec{p})$. We expand the terms linear in a_S up to first order in gradients and the terms quadratic in a_S to zero order, keeping only the local term. This amounts to a semi-classical approximation of the theory. In this case we substitute $W_{ac}(\vec{x}_1 - \frac{\vec{r}-\vec{r}'}{2}, \vec{p}_1')W_{bd}(\vec{x}_1 - \frac{\vec{r}+\vec{r}'}{2}, \vec{p}_2') \approx W_{ac}(\vec{x}_1, \vec{p}_1')W_{bd}(\vec{x}_1, \vec{p}_2')$ into (4.24) and (4.25), which means that further delta functions $\int d^3r' \mathrm{e}^{i(\vec{k}_2-\vec{k}_1)\cdot\vec{r}'} = (2\pi)^3\delta(\vec{k}_2 - \vec{k}_1)$, $\int d^3r \mathrm{e}^{i\vec{\kappa}\cdot\vec{r}} = (2\pi)^3\delta(\vec{\kappa})$ appear. We introduce renamed variables $\vec{k}_\pm \to \vec{k}$, $\vec{k}_1 \to \vec{k}'$, $\vec{x}_1, \vec{p}_1 \to \vec{x}, \vec{p}$ and $\vec{p}_\pm \equiv \vec{p} - \hbar(\vec{k} \pm \vec{k}')$ the local parts of the collision integral become

$$\begin{aligned} I^T_{ij}(\vec{x}, \vec{p}) = \frac{-i}{2(2\pi)^3} \int d^3q \int d^3k' \sum_{abcdl} \delta(\epsilon_k - \epsilon_{k'} + Q_{ilab})\Big(\delta(\vec{k} - \vec{k}')\delta_{jc}\delta_{ld} - \delta(\vec{k} + \vec{k}')\delta_{lc}\delta_{jd}\Big) \\ \times \Big(T_{ilab}(\vec{k}_+, \vec{k}_1) - T_{liab}(-\vec{k}_+, \vec{k}_1)\Big) W_{ac}(\vec{x}, \vec{p}_-)W_{bd}(\vec{x}, \vec{p}_+) + \text{h.c.} \end{aligned} \tag{4.28}$$

and

$$\begin{aligned} I^{T^2}_{ij}(\vec{x}, \vec{p}) = \frac{1}{2(2\pi)^3} \int d^3q \int d^3k' \sum_{abcdl} \delta(\epsilon_k - \epsilon_{k'} + Q_{ilab})\delta(\epsilon_{k'} - \epsilon_k + Q_{cdjl}) \\ \times \Big(T_{ilab}(\vec{k}_+, \vec{k}_1) - T_{liab}(-\vec{k}_+, \vec{k}_1)\Big)\Big(T^*_{jlcd}(\vec{k}_-, \vec{k}_2) - T^*_{ljcd}(-\vec{k}_-, \vec{k}_2)\Big) \\ \times W_{ac}(\vec{x}, \vec{p}_-)W_{bd}(\vec{x}, \vec{p}_+). \end{aligned} \tag{4.29}$$

4.5 Squares and products of delta functions

In scattering theory, the square of a delta function of energy appears frequently, when terms quadratic in the T-matrix are involved, where each T-matrix contains a delta-function for the on-shell condition. The well-known interpretation of this artifact is $[\delta(E)]^2 \approx \frac{\Delta t}{2\pi\hbar}\delta(E)$, where Δt denotes the elapsed time interval, which is quasi-infinite when compared to the duration of a single scattering event but nevertheless short compared to other relevant dynamics, like relaxation or the trapping period (see e.g. [78]). We first illustrate the standard case and use the Fourier representation of the delta function

$$\delta(E) = \frac{1}{2\pi\hbar}\int dt e^{\frac{i}{\hbar}Et}, \tag{4.30}$$

such that

$$\begin{aligned} [\delta(E)]^2 &= \delta(E)\frac{1}{2\pi\hbar}\int dt e^{\frac{i}{\hbar}Et} = \delta(E)\frac{1}{2\pi\hbar}\int dt \\ &\approx \delta(E)\frac{1}{2\pi\hbar}\int_{\Delta t} dt = \frac{\Delta t}{2\pi\hbar}\delta(E) \end{aligned} \tag{4.31}$$

This can also be applied to products of the form $\delta(\epsilon_k - \epsilon_{k'})\delta(\vec{k} - \vec{k}')$ since in spherical coordinates

$$\delta(\vec{k} - \vec{k}') = \frac{1}{4\pi k^2}\delta(k - k')\delta(\Theta - \Theta')\delta(\phi - \phi'), \tag{4.32}$$

while the delta function of energies reads

$$\begin{aligned} \delta(\epsilon_k - \epsilon_{k'}) &= \delta\left(\frac{\hbar^2 k^2}{2\mu} - \frac{\hbar^2 k'^2}{2\mu}\right) \\ &= \frac{\mu}{\hbar^2 |k|}\delta(k - k'). \end{aligned} \tag{4.33}$$

Hence, a product of both can be approximated as

$$\begin{aligned} \delta\left(\frac{\hbar^2 k^2}{2\mu} - \frac{\hbar^2 k'^2}{2\mu}\right)\delta(\vec{k} - \vec{k}') &= \frac{\mu}{4\pi\hbar^2 k^3}\delta(k - k')^2\delta(\Theta - \Theta')\delta(\phi - \phi') \\ &= \frac{\hbar^2}{4\pi\mu k}\delta(\epsilon_k - \epsilon_{k'})^2\delta(\Theta - \Theta')\delta(\phi - \phi') \\ &\approx \frac{\hbar\Delta t}{8\pi^2\mu k}\delta(\epsilon_k - \epsilon_{k'})\delta(\Theta - \Theta')\delta(\phi - \phi') \\ &= \frac{\Delta t}{2\pi\hbar}\delta(k - k')\delta(\Theta - \Theta')\delta(\phi - \phi') \\ &= \frac{\Delta t}{2\pi\hbar}\delta(\vec{k} - \vec{k}') \end{aligned} \tag{4.34}$$

We now deviate from the textbook example and modify this approximation to take into account a shift Q in the quadratic Zeeman energy, which occurs in a spin-changing collision at finite magnetic field. In our calculations two situations appear. In the first, coming from (4.28), there is only a Zeeman shift in one of the delta-functions and we must be careful, that only the delta-function of energy with the shift comes from the on-shell T-matrix, where we can approximate the integration area with the interval Δt:

$$\begin{aligned}
&\delta(\epsilon_k - \epsilon_{k'})\delta(\epsilon_k - \epsilon_{k'} + Q) \\
&\approx \delta(\epsilon_k - \epsilon_{k'})\frac{1}{2\pi\hbar}\int_{\Delta t} dt \mathrm{e}^{\frac{i}{\hbar}(\epsilon_k - \epsilon_{k'} + Q)t} \\
&= \delta(\epsilon_k - \epsilon_{k'})\frac{1}{2\pi\hbar}\int_{\Delta t} dt \mathrm{e}^{\frac{i}{\hbar}Qt/} \\
&= \frac{\Delta t}{2\pi\hbar}\delta(\epsilon_k - \epsilon_{k'})\mathrm{sinc}\left(\frac{Q\Delta t}{2\hbar}\right).
\end{aligned} \tag{4.35}$$

In the second case, both delta-functions originate from the energy conservation of the T-matrix and carry a quadratic Zeeman shift, which is not necessarily the same

$$\begin{aligned}
&\delta(\epsilon_k - \epsilon_{k'} + Q_1)\delta(\epsilon_k - \epsilon_{k'} + Q_2) \\
&= \frac{1}{(2\pi\hbar)^2}\int_{\Delta t} dt \int_{\Delta t} dt' \mathrm{e}^{\frac{i}{\hbar}(\epsilon_k - \epsilon_{k'} + Q_1)t}\mathrm{e}^{\frac{i}{\hbar}(\epsilon_k - \epsilon_{k'} + Q_2)t'} \\
&= \frac{1}{(2\pi\hbar)^2}\int_{\Delta t} dt \int_{\Delta t} dt' \mathrm{e}^{\frac{i}{\hbar}((\epsilon_k - \epsilon_{k'})(t+t') + Q_1 t + Q_2 t')} \\
&= \frac{2}{(2\pi\hbar)^2}\int_{\Delta t} du \int_{\Delta t} du' \mathrm{e}^{\frac{i}{\hbar}(\epsilon_k - \epsilon_{k'})u}\mathrm{e}^{\frac{iQ_1}{2\hbar}(u-u')}\mathrm{e}^{\frac{iQ_2}{2\hbar}(u+u')} \\
&= \frac{2}{(2\pi\hbar)^2}\int_{\Delta t} du \int_{\Delta t} du' \mathrm{e}^{\frac{i}{\hbar}(\epsilon_k - \epsilon_{k'} + \frac{Q_1+Q_2}{2})u}\mathrm{e}^{\frac{i}{2\hbar}(Q_2 - Q_1)u'} \\
&\approx \frac{\Delta t}{2\pi\hbar}\delta\left(\epsilon_k - \epsilon_{k'} + \tfrac{1}{2}(Q_1 + Q_2)\right)\mathrm{sinc}\left(\frac{Q_2 - Q_1}{2\hbar}\Delta t\right).
\end{aligned} \tag{4.36}$$

As it should, the time interval Δt that appears in front cancels with the one introduced at the beginning (4.2), like in the original theory (see [64, 79]). However, here, we must take the limit that the time interval is small compared to any macroscopic dynamics, such that $\Delta t \to 0$ and the sinc function goes to 1.

With these approximations, the two expressions for the collision integral become

$$\begin{aligned}
I_{ij}^{T}(\vec{x},\vec{p}) = \frac{(2\pi)^3}{2}\frac{i\Delta t}{2\pi\hbar}\int d^3k' \int d^3q \sum_{abcdl}\left(\delta(\vec{k}-\vec{k}')\delta_{cj}\delta_{dl} - \delta(\vec{k}+\vec{k}')\delta_{lc}\delta_{jd}\right) \\
\times \left(T_{ilab}(\vec{k},\vec{k}') - T_{liab}(-\vec{k},\vec{k}')\right) W_{ac}(\vec{x},\vec{p}-\hbar(\vec{k}-\vec{k}'))W_{bd}(\vec{x},\vec{p}-\hbar(\vec{k}+\vec{k}')) + \text{h.c.}
\end{aligned} \tag{4.37}$$

and

$$\begin{aligned}
I_{ij}^{T^2}(\vec{x},\vec{p}) = \frac{(2\pi)^3}{2}\frac{\Delta t}{2\pi\hbar}\int d^3k' \int d^3q \sum_{abcdl}\delta(\epsilon_k - \epsilon_{k'} + Q_{ijlabcd})\left(T_{ilab}(\vec{k},\vec{k}') - T_{liab}(-\vec{k},\vec{k}')\right) \\
\times \left(T^*_{jlcd}(\vec{k},\vec{k}') - T^*_{ljcd}(-\vec{k},\vec{k}')\right) W_{ac}(\vec{x},\vec{p}-\hbar(\vec{k}-\vec{k}'))W_{bd}(\vec{x},\vec{p}-\hbar(\vec{k}+\vec{k}')),
\end{aligned} \tag{4.38}$$

where the quadratic Zeeman shift in the second term is given as $Q_{ijlabcd} = \frac{1}{2}Q(i^2 + j^2 + 2l^2 - a^2 - b^2 - c^2 - d^2)$.

4.6 T-matrix for large spin

The two-body scattering problem in the center-of-mass frame is described by the Hamiltonian

$$H = \frac{-\hbar^2\nabla^2}{2\mu} + g\delta(\vec{r}) \tag{4.39}$$

in the case of contact interaction of strength $g = 4\pi\hbar^2 a/M$, where a is the s-wave scattering length. The wave function is of the form

$$\psi(\vec{x}) = \mathrm{e}^{i\vec{k}\cdot\vec{r}} + \psi_{\mathrm{sc}}(\vec{r}), \tag{4.40}$$

where $\vec{k}$ denotes the wave-vector of the incoming plane wave and $\psi_{\mathrm{sc}}(\vec{r})$ the scattered wave function. Making the Ansatz of a spherical wave $\psi_{\mathrm{sc}}(\vec{r}) = f_{k'}\frac{\mathrm{e}^{ik'r}}{r}$, we obtain $f_{k'} = \frac{-a}{1+ika}$ for the scattering amplitude $f_{k'}$ by solving the stationary Schrödinger equation.

In the momentum-representation, the T-matrix is related to the scattered wave function through the identity

$$\tilde{\psi}_{\mathrm{sc}}(\vec{k}') = G(\vec{k}, \vec{k}')T(\vec{k}', \vec{k}), \tag{4.41}$$

with the free Green's function $G(\vec{k}, \vec{k}') = \left(\frac{\hbar^2k^2}{2\mu} - \frac{\hbar^2k'^2}{2\mu} + i0^+\right)^{-1}$. Its representation in position space is

$$\begin{aligned} G(\vec{r}) &= \frac{2\mu}{\hbar^2}\int d^3k' \frac{\mathrm{e}^{i\vec{k}'\cdot\vec{r}}}{k^2 - k'^2 + i0^+} \\ &= -(2\pi)^3 \frac{\mu}{2\pi\hbar^2}\frac{\mathrm{e}^{ikr}}{r}. \end{aligned} \tag{4.42}$$

Hence the T-matrix and the scattering amplitude differ only by a pre-factor and fulfill the identity

$$T(\vec{k}', \vec{k}) = -(2\pi)^{-3}\frac{2\pi\hbar^2}{\mu}f_{k'} \tag{4.43}$$

and the expression for the T-matrix in terms of the scattering length is

$$T(\vec{k}', \vec{k}) = (2\pi)^{-3}\frac{2\pi\hbar^2 a}{\mu}\frac{1}{1 + ik'a}. \tag{4.44}$$

We have not made the usual assumption that $k = k'$, i.e. that kinetic energy is conserved, since here this is not always the case. The on-shell (energy conservation) condition for a spin-changing collision is a delta function $\delta(\epsilon_k - \epsilon_{k'} + Q)$, where Q denotes a shift in energy associated with different quadratic Zeeman energies for the initial and final spin-configuration. Hence the moduli of the incoming and outgoing wave vectors are related via $k' = \sqrt{k^2 + Q}$ in this case. Here and throughout this thesis, we use an implicit distinction of two cases: if the argument of such a square root becomes negative for a negative $Q < -k^2$, the T-matrix vanishes and with it the entire collision term, so the square root is implicitly taken to be zero for a negative argument.

Obviously Eq. (4.44) holds in any total spin channel with associated scattering length a_S, so in each channel there is a T-matrix

$$T_S(\vec{k}', \vec{k}) = (2\pi)^{-3} \frac{2\pi\hbar^2 a_S}{\mu} \frac{1}{1 + ik'a_S}, \tag{4.45}$$

which can be transformed into the basis of individual spins in the same fashion as the mean-field coupling constants (2.16), such that

$$T_{ijmn}(\vec{k}', \vec{k}) = \sum_{SM} \langle ij|SM\rangle\langle SM|mn\rangle T_S(\vec{k}', \vec{k}). \tag{4.46}$$

We expand this in powers of the scattering lengths to obtain an expansion for weak interactions, which can be performed alongside the gradient expansion (4.27),

$$T_S(\vec{k}', \vec{k}) = \frac{1}{(2\pi)^3} \frac{2\pi\hbar^2}{\mu} a_S(1 - ik'a_S) = \frac{1}{(2\pi)^3} g_S(1 - ik'a_S) = \frac{1}{(2\pi)^3} \left(g_S - ik' \frac{M}{4\pi\hbar^2} g_S^2 \right) \tag{4.47}$$

$$T_{ijmn}(\vec{k}', \vec{k}) = \frac{1}{(2\pi)^3} \left(U_{imjn} - ik' \frac{M}{4\pi\hbar^2} \tilde{U}_{imjn} \right), \tag{4.48}$$

where we introduced the second-order coupling constants

$$\tilde{U}_{imjn} = \sum_{SM} \langle ij|SM\rangle\langle SM|mn\rangle g_S^2. \tag{4.49}$$

4.7 Full Boltzmann equation

Finally we substitute the result for the the T-matrix into the collision term (equations (4.37),(4.38)). The expansion of the total collision term will be up to second order in scattering lengths, which means that in I^T we expand the T-matrix to second order and in I^{T^2} to first order. We start with I^T, where the integration over $\vec{k}'$ is straightforward. We split it into a term I^{mf} linear in scattering lengths and a quadratic term I^T, and include the pre-factor $2\pi/\Delta t$ from Eq. (4.9), such that $2\pi/\Delta t I^T \to I^{\text{mf}} + I^T$. We obtain

$$I^{\text{mf}}_{ij}(\vec{x}, \vec{p}) = -\frac{2i}{\hbar} \int d^3q \sum_{abl} \left[U_{ialb} W_{aj}(\vec{x}, \vec{p}) W_{bc}(\vec{x}, \vec{q}) - U_{ajbl} W_{ia}(\vec{x}, \vec{p}) W_{bc}(\vec{x}, \vec{q}) \right]. \tag{4.50}$$

This term is identical to the zero order term in the mean field equation of motion (3.22). The other term becomes

$$\begin{aligned} I^T_{ij}(\vec{x}, \vec{p}) = -\frac{M}{4\pi\hbar^4} \int d^3q \sum_{abl} \Big[&\sqrt{q^2 + \Delta_{ilab}} \tilde{U}_{ialb} W_{aj}(\vec{x}, \vec{p}) W_{bc}(\vec{x}, \vec{p} - \vec{q}) \\ &+ \sqrt{q^2 + \Delta_{abjl}} \tilde{U}_{ajbl} W_{ia}(\vec{x}, \vec{p}) W_{cb}(\vec{x}, \vec{p} - \vec{q}) \Big]. \end{aligned} \tag{4.51}$$

The integration in I^{T^2} is less straightforward. We transform one integration variable into spherical coordinates

$$\int d^3k' = \int_0^\infty dk' \int d\Omega k'^2 \tag{4.52}$$

and integrate over k'. As a function of k', the delta function fulfills

$$\delta\left(\epsilon_k - \epsilon_{k'} + Q_{ijlabcd}\right) = \frac{M}{2\hbar^2 \bar{k}} \delta(k' - \bar{k}), \tag{4.53}$$

where $\bar{k} = \sqrt{k^2 + \Delta_{ijlabcd}}$ and $\Delta_{ijlabcd} = 2MQ(i^2 + j^2 + 2l^2 - a^2 - b^2 - c^2 - d^2)$. We obtain

$$\begin{aligned} I_{ij}^{T^2}(\vec{x},\vec{p}) = \frac{M}{4\pi^2\hbar^4} \int d^3q \int d\Omega \sum_{abcdl} \hbar\bar{k} U_{ialb} U_{jcld} \\ \times W_{ac}(\vec{x},\vec{p} - \hbar(\vec{k} - \bar{k}\vec{e}_\Omega)) W_{bd}(\vec{x},\vec{p} - \hbar(\vec{k} + \bar{k}\vec{e}_\Omega)), \end{aligned} \tag{4.54}$$

where $\vec{e}_\Omega$ denotes the unit vector corresponding to solid angle $d\Omega$. The full equation, including the kinetic and external contributions reads

$$\begin{aligned} &\frac{d}{dt} W_{ij}(\vec{x},\vec{p}) + \left[\frac{\vec{p}}{M} \cdot \nabla_x - M\left(\omega_x^2 x, \omega_y^2 y, \omega_z^2 z\right) \cdot \nabla_p + \frac{iQ}{\hbar}(n^2 - m^2)\right] W_{ij}(\vec{x},\vec{p}) \\ &\quad + \frac{i}{\hbar} \sum_l \left[V_{jl}(\vec{x}) W_{il}(\vec{x},\vec{p}) - W_{li}(\vec{x},\vec{p}) V_{lj}(\vec{x})\right] \\ &\quad - \frac{1}{2} \sum_l \left\{\nabla_x V_{jl}(\vec{x}) \cdot \nabla_p W_{il}(\vec{x},\vec{p}) + \nabla_p W_{li}(\vec{x},\vec{p}) \cdot \nabla_x V_{lj}(\vec{x})\right\} \\ &\quad = -\frac{M}{4\pi\hbar^4} \int d^3q \left\{ \sum_{abc} \left(\sqrt{q^2 + \Delta_{icab}} \tilde{U}_{iacb} W_{aj}(\vec{x},\vec{p}) W_{bc}(\vec{x},\vec{p} - \vec{q}) \right.\right. \\ &\quad + \left. \sqrt{q^2 + \Delta_{abjc}} \tilde{U}_{ajbc} W_{ia}(\vec{x},\vec{p}) W_{cb}(\vec{x},\vec{p} - \vec{q}) \right) \\ &\quad - \left. \frac{1}{2\pi} \int d\Omega \sum_{abcdl} \hbar\bar{k} U_{ialb} U_{jcld} W_{ac}(\vec{x},\vec{p} - \hbar(\vec{k} - \bar{k}\vec{e}_\Omega)) W_{bd}(\vec{x},\vec{p} - \hbar(\vec{k} + \bar{k}\vec{e}_\Omega)) \right\}. \end{aligned} \tag{4.55}$$

This equation is the main result of this chapter. It extends the approach of Lhuillier-Laloë to arbitrary values of spin, multiple scattering channels including spin-changing collisions, and the presence of a quadratic Zeeman effect. We note, that on the left hand side of Eq. (4.55), this method reproduces exactly the mean-field result (3.22) of the previous section. The additional terms on the right hand side are quadratic in scattering lengths and, with their origin from an expansion of the T-matrix in terms of the scattering lengths, provide a correction to the mean-field terms. Physically, we can identify them as different scattering processes. The mean-field terms arise from the lowest order of the real part of the T-matrix (4.45), and describe forward scattering. The effect of forward scattering is basically a phase-shift, while individual momenta of the scattering particles are unchanged. This phase shift can be mimicked by a (mean-field) potential on the single-particle level. In the case of spin $1/2$, this potential can actually be decomposed into a scalar force and an effective magnetic field [56, 64, 77]. The quadratic terms describe backwards and lateral scattering, where individual momenta are changed. These processes cannot be described as coherent on the single-particle level, but make the single-particle problem an open dissipative problem. Mathematically, they lead to a decay of the off-diagonal elements of the Wigner function, the single-particle spin coherences. The first two terms of the right-hand side of Eq. (4.55) originate from linear terms in the T-matrix, but contain the second order of its expansion, which correspond to the imaginary part of the T-matrix. This describes the intensity shift of the forward scattered wave [64, 74, 79], as opposed to the phase shift in the mean-field term. The last term in Eq. (4.55) describes lateral collisions, which manifests in the explicit angular dependence.

Chapter 5

One-dimensional systems

In this thesis, we derive equations of motion for Fermi gases in a variety of geometries, given both by experimental setups and technical limitations when it comes to numerical treatment of the kinetic equations. The full 3D Boltzmann equation (4.55) is a set of $(2F+1)^2$ coupled partial integro-differential equations in seven dimensions $(\vec{x}, \vec{p}, t)$, and numerical simulation of it is not feasible using standard methods for such equations. However, studying the same high-spin Fermi system in a one-dimensional system reduces it to three dimensions (x, p_x, t). In this chapter we describe, how to use dimensionally reduced equations to describe the essential physics in the system. There are two geometries to distinguish here, which we term *1D* and *quasi-1D* systems, respectively, throughout this thesis. By 1D, we denote a system, where the harmonic trap is very strong in two dimensions, such that $\omega_x \ll \omega_\perp = \sqrt{\omega_y \omega_z}$ and the radial confinement is sufficiently strong such that $\hbar\omega_\perp \gg \mu, k_\mathrm{B}T$ and we can assume that all particles occupy the radial ground state, hence radial dynamics is completely frozen out. With a quasi-1D, we denote the case, where $\omega_x \ll \omega_\perp$, but large numbers of radial modes are still occupied. In this case, transversal dynamics is assumed to be so fast that we can assume the system to be in equilibrium with respect to the radial axes, and all relevant dynamics happens along the x-axis. The former leads to a more rigid theoretical description, while the latter is in many cases a good and practical approximation. It is justified for certain trapping geometries, which lead to an effect we call *dynamically induced long-range interactions* [56], which we introduce in chapter 6.

5.1 Hamiltonian of the 1D system

In this section, we derive the equivalent of the Hamiltonians (3.10) and (3.13) for a 1D system, under the assumption that the radial dynamics are fully frozen out, as described above. We assume, that any external magnetic fields vary only along the axial direction. With this assumption, the trap and external fields can be split into radial and axial contributions as

$$\begin{aligned} V_{mn}^{\text{ext}}(\vec{x}) &= V_{mn}^{\text{ext}}(x) + V^{\text{ext}}(y,z) \\ &= \frac{M}{2}\omega^2 x^2 + Q(x) m^2 \delta_{mn} + \frac{M}{2}\left(\omega_y^2 y^2 + \omega_z^2 z^2\right). \end{aligned} \tag{5.1}$$

If the atoms are all in the ground state of the transversal harmonic oscillator, we can replace the field operators by products

$$\hat{\psi}_m(\vec{x}) = \hat{\phi}_m(x)\chi(y,z), \tag{5.2}$$

where $\chi(y,z) = (M\omega_\perp/\pi\hbar)^{1/4}\mathrm{e}^{-M(\omega_y y^2+\omega_z z^2)/2\hbar}$ denotes the radial ground state wave function. We substitute (5.1) and (5.2) into the single-particle Hamiltonian (3.10):

$$\begin{aligned} \hat{H}_0 &= \sum_{mn}\int d^3x \hat{\phi}_m^\dagger(x)\chi^*(y,z)\left[-\frac{\hbar^2\nabla^2}{2M}\delta_{mn} + V_{mn}^{\text{ext}}(x) + V^{\text{ext}}(y,z)\delta_{mn}\right]\hat{\phi}_n(x)\chi(y,z) \\ &= \sum_{mn}\int dx \phi_m^\dagger(x)\left[-\frac{\hbar^2\partial_x^2}{2M}\delta_{mn} + V_{mn}^{\text{ext}}(x)\right]\phi_n(x) \times \int dy \int dz |\chi(y,z)|^2 \\ &+ \sum_{mn}\int dx \phi_m^\dagger(x)\phi_n(x) \times \int dy \int dz \chi^*(y,z)\left[-\frac{\hbar^2(\partial_y^2+\partial_z^2)}{2M} + V^{\text{ext}}(y,z)\right]\chi(y,z). \end{aligned} \tag{5.3}$$

Using the normalization of χ, we obtain

$$\hat{H}_0 = \sum_{mn}\int dx \phi_m^\dagger(x)\left[-\frac{\hbar^2\partial_x^2}{2M}\delta_{mn} + V_{mn}^{\text{ext}}(x)\right]\phi_n(x) + \text{const.} \tag{5.4}$$

for the one-dimensional single-particle Hamiltonian. The interaction Hamiltonian can be derived similarly:

$$\begin{aligned} \hat{H}_1 &= \frac{1}{2}\sum_{ijkl}\int dx U_{ijkl}\hat{\phi}_i^\dagger(x)\hat{\phi}_k^\dagger(x)\hat{\phi}_l(x)\hat{\phi}_j(x) \times \int dy \int dz |\chi(y,z)|^4 \\ &= \frac{M\omega_\perp}{2\pi\hbar}\sum_{ijkl}\int dx U_{ijkl}\hat{\phi}_i^\dagger(x)\hat{\phi}_k^\dagger(x)\hat{\phi}_l(x)\hat{\phi}_j(x). \end{aligned} \tag{5.5}$$

Hence, for the 1D system, we define rescaled coupling constants

$$g_S^{1\text{D}} = 2\hbar\sqrt{\omega_y\omega_z}a_S, \qquad U_{ijkl}^{1\text{D}} = \sum_{S,M} g_S^{1\text{D}}\langle ik|SM\rangle\langle SM|jl\rangle, \tag{5.6}$$

such that in the end, both single-particle and interaction Hamiltonian retain their shape

$$\hat{H}_0 = \sum_{mn}\int \mathrm{d}x \hat{\phi}_m^\dagger(x)\left[-\frac{\hbar^2\partial_x^2}{2M}\delta_{mn} + V_{mn}^{\text{ext}}(x)\right]\hat{\phi}_n(x), \tag{5.7}$$

$$\hat{H}_1 = \frac{1}{2}\sum_{ijkl}\int \mathrm{d}x U_{ijkl}^{1\text{D}}\hat{\phi}_i^\dagger(x)\hat{\phi}_k^\dagger(x)\hat{\phi}_l(x)\hat{\phi}_j(x). \tag{5.8}$$

This kind of systems has been studied in greater detail in Ref. [80], however, throughout this thesis, we remain in a regime where we can neglect the confinement-induced resonance when a_S approaches the transversal system size $\sqrt{\hbar/M\omega_\perp}$.

5.2 Mean-field equations in 1D

The mean-field equation of motion is derived completely analogously to the 3D case in chapter 3, using the Hamiltonian derived in the preceding section. We define the one-dimensional Wigner function according to

$$W_{mn}(x,p) = \frac{1}{2\pi\hbar}\int \mathrm{d}y \mathrm{e}^{ipy/\hbar}\left\langle \hat{\phi}_m(x-y/2)\hat{\phi}_n(x+y/2)\right\rangle . \tag{5.9}$$

The mean field potential now contains the rescale coupling constants

$$V^{\mathrm{mf}}_{mn}(x) = 2\sum_{kl}\int d^3p U^{1\mathrm{D}}_{klnm} W_{kl}(x,p). \tag{5.10}$$

and the semi-classical equation of motion is given by

$$\frac{\mathrm{d}}{\mathrm{d}t}\hat{W}(x,p) + \frac{p}{M}\partial_x \hat{W}(x,p) = \frac{i}{\hbar}\left[\hat{V}(x),\hat{W}(x,p)\right] + \frac{1}{2}\left\{\partial_x\hat{V}(x),\partial_p\hat{W}(x,p)\right\}, \tag{5.11}$$

where $V(x)$ now contains the axial trap and 1D mean-field potential (5.10). This equation allows for a simpler numerical treatment, having only 3 variables (x,p,t) and is used in chapter (7) to generate the numerical data.

5.3 Boltzmann equation in 1D

The derivation of the full Boltzmann equation using the generalized method of Lhuillier and Laloë is analogous to the 3D case in chapter 4, but we encounter additional difficulties. Therefore, we derive the 1D Boltzmann equation in more detail than the mean-field theory above. We start from the 1D-equivalent of equations (4.18) and (4.19),

$$\begin{aligned} W^{T}_{ijmn}(r,R,p,P) = \frac{-i}{4\pi\hbar^2}&\int dK\int d\kappa\int dk_1\int dk_2 \mathrm{e}^{iKR}\mathrm{e}^{i\kappa r}\\ &\times\sum_{abcd}\left(\delta(k_2-k_-)\delta_{cj}\delta_{dn} - \delta(k_2+k_-)\delta_{nc}\delta_{jd}\right)\delta(\epsilon_{k_+}-\epsilon_{k_1}+Q_{imab})\\ &\times\left(T_{imab}(k_+,k_1) - T_{miab}(-k_+,k_1)\right)\langle K_+,k_1,a,b|\hat{\rho}(1)\otimes\hat{\rho}(2)|K_-,k_2,c,d\rangle + \text{h.c.}, \end{aligned} \tag{5.12}$$

$$\begin{aligned} W^{T^2}_{ijmn}(r,R,p,P) = \frac{1}{2\hbar^2}&\int dK\int d\kappa\int dk_1\int dk_2 \mathrm{e}^{iKR}\mathrm{e}^{i\kappa r}\sum_{abcd}\delta(\epsilon_{k_+}-\epsilon_{k_1}+Q_{imab})\\ &\times\delta(\epsilon_{k_2}-\epsilon_{k_-}+Q_{cdjn})\left(T_{imab}(k_+,k_1) - T_{miab}(-k_+,k_1)\right)\\ &\times\left(T^*_{jncd}(k_-,k_2) - T^*_{njcd}(-k_-,k_2)\right)\langle K_+,k_1,a,b|\hat{\rho}(1)\otimes\hat{\rho}(2)|K_-,k_2,c,d\rangle. \end{aligned} \tag{5.13}$$

The inverse Wigner transform of the product of density matrices $\rho(1) \otimes \rho(2)$ is given by

$$\langle K_+, k_1, a, b|\hat{\rho}(1) \otimes \hat{\rho}(2)|K_-, k_2, c, d\rangle = \hbar^2 \int dR' \int dr' \mathrm{e}^{-iKR'} \mathrm{e}^{i(k_2-k_1)r'} \\ \times W_{ac}(R' + \tfrac{r'}{2}, \tfrac{P+\hbar k_1+\hbar k_2}{2}) W_{bd}(R' - \tfrac{r'}{2}, \tfrac{P-\hbar k_1-k_2}{2}). \tag{5.14}$$

in one dimension. We obtain the intermediate result

$$W^T_{ijmn}(r, R, p, P) = \frac{-i}{2} \int d\kappa \int dk_1 \int dk_2 \int dr' \mathrm{e}^{i\kappa r} \mathrm{e}^{i(k_2-k_1)r'} \sum_{abcd} \delta(\epsilon_{k_+} - \epsilon_{k_1} + Q_{imab}) \\ \times (\delta(k_2 - k_-)\delta_{cj}\delta_{dn} - \delta(k_2 + k_-)\delta_{nc}\delta_{jd}) (T_{imab}(k_+, k_1) - T_{miab}(-k_+, k_1)) \\ \times W_{ac}(R + \tfrac{r'}{2}, \tfrac{P+\hbar k_1+\hbar k_2}{2}) W_{bd}(R - \tfrac{r'}{2}, \tfrac{P-\hbar k_1-\hbar k_2}{2}) + \text{h.c.}, \tag{5.15}$$

$$W^{T^2}_{ijmn}(r, R, p, P) = \pi \int d\kappa \int dk_1 \int dk_2 \int dr' \mathrm{e}^{i\kappa r} \mathrm{e}^{i(k_2-k_1)r'} \sum_{abcd} \delta(\epsilon_{k_+} - \epsilon_{k_1} + Q_{imab}) \\ \times \delta(\epsilon_{k_2} - \epsilon_{k_-} + Q_{cdjn})(T_{imab}(k_+, k_1) - T_{miab}(-k_+, k_1))\big(T^*_{jncd}(k_-, k_2) - T^*_{lncd}(-k_-, k_2)\big) \\ \times W_{ac}(R + \tfrac{r'}{2}, \tfrac{P+\hbar k_1+\hbar k_2}{2}) W_{bd}(R - \tfrac{r'}{2}, \tfrac{P-\hbar k_1-\hbar k_2}{2}), \tag{5.16}$$

before performing the trace operation

$$I^{(T,T^2)}_{ij}(x_1, p_1) = \frac{1}{\Delta t} \int dx_2 \int dp_2 \sum_{mn} \delta_{mn} W^{(T,T^2)}_{ijmn}(r, R, p, P)$$

on the second particle. This provides us the next expressions

$$I^T_{ij}(x_1, p_1) = \frac{-i}{2\Delta t} \int d\kappa \int dk_1 \int dk_2 \int dr' \int dr \int dq \mathrm{e}^{i\kappa r} \mathrm{e}^{i(k_2-k_1)r'} \\ \times \sum_{abcdl} \delta(\epsilon_{k_+} - \epsilon_{k_1} + Q_{ilab}) (\delta(k_2 - k_-)\delta_{cj}\delta_{dl} - \delta(k_2 + k_-)\delta_{lc}\delta_{jd}) \\ \times (T_{ilab}(k_+, k_1) - T_{liab}(-k_+, k_1)) W_{ac}(x_1 - \tfrac{r-r'}{2}, p'_1) W_{bd}(x_1 - \tfrac{r+r'}{2}, p'_2) + \text{h.c.}, \tag{5.17}$$

$$I^{T^2}_{ij}(x_1, p_1) = \frac{\pi}{\Delta t} \int d\kappa \int dk_1 \int dk_2 \int dr' \int dr \int dq \mathrm{e}^{i\kappa r} \mathrm{e}^{i(k_2-k_1)r'} \\ \times \sum_{abcdl} \delta(\epsilon_{k_+} - \epsilon_{k_1} + Q_{ilab}) \delta(\epsilon_{k_2} - \epsilon_{k_-} + Q_{cdjl}) (T_{ilab}(k_+, k_1) - T_{liab}(-k_+, k_1)) \\ \times \big(T^*_{jlcd}(k_-, k_2) - T^*_{ljcd}(-k_-, k_2)\big) W_{ac}(x_1 - \tfrac{r-r'}{2}, p'_1) W_{bd}(x_1 - \tfrac{r+r'}{2}, p'_2). \tag{5.18}$$

for the two parts of the 1D collision integral. The semi-classical gradient expansion (4.27) is valid in 1D systems as well, where we expand the Wigner function as

$$W_{ij}(x_1 - \tfrac{r \pm r'}{2}, p) = W_{ij}(x_1, p) - \tfrac{r \pm r'}{2} \partial_{x_1} W_{ij}(x_1, p) + \ldots \tag{5.19}$$

and consequently obtain the expansion

$$\begin{aligned}W_{ac}(x_1 - \tfrac{r-r'}{2}, p_1')W_{bd}(x_1 - \tfrac{r+r'}{2}, p_2') &= W_{ac}(x_1, p_1')W_{bd}(x_1, p_2')\\ &- \tfrac{r}{2}\partial_{x_1}\left(W_{ac}(x_1, p_1')W_{bd}(x_1, p_2')\right) + \tfrac{r'}{2}W_{bd}(x_1, p_2')\partial_{x_1}W_{ac}(x_1, p_1')\\ &- \tfrac{r'}{2}W_{ac}(x_1, p_1')\partial_{x_1}W_{bd}(x_1, p_2') + \dots \end{aligned} \tag{5.20}$$

for their product. Introducing the same renamed variables $k_\pm \to k$, $k_1 \to k'$, $x_1, p_1 \to x, p$ and $p_\pm \equiv p - \hbar(k \pm k')$, as in the 3D case, we arrive at the expressions

$$\begin{aligned}I^T_{ij}(x,p) &= \frac{-i}{4\pi}\int dq \int dk' \sum_{abcdl} \delta(\epsilon_k - \epsilon_{k'} + Q_{ilab})\left(\delta(k-k')\delta_{jc}\delta_{ld} - \delta(k+k')\delta_{lc}\delta_{jd}\right)\\ &\times \left(T_{ilab}(k_+, k_1) - T_{liab}(-k_+, k_1)\right) W_{ac}(x, p_-)W_{bd}(x, p_+) + \text{h.c.}, \end{aligned} \tag{5.21}$$

$$\begin{aligned}I^{T^2}_{ij}(\vec{x},\vec{p}) &= \frac{1}{4\pi}\int dq \int dk' \sum_{abcdl} \delta(\epsilon_k - \epsilon_{k'} + Q_{ilab})\delta(\epsilon_{k'} - \epsilon_k + Q_{cdjl})\\ &\times \left(T_{ilab}(k_+, k_1) - T_{liab}(-k_+, k_1)\right)\left(T^*_{jlcd}(k_-, k_2) - T^*_{ljcd}(-k_-, k_2)\right) W_{ac}(x, p_-)W_{bd}(x, p_+). \end{aligned} \tag{5.22}$$

for the local terms.

The approximations for a product of two delta functions of energy obviously does not depend on the dimensionality. However, the proof of the relation

$$\delta(\epsilon_k - \epsilon_{k'})\delta(k-k') \approx \frac{\Delta t}{2\pi\hbar}\delta(k-k') \tag{5.23}$$

works different in the one-dimensional case. Here

$$\delta(\epsilon_k - \epsilon_{k'}) = \delta\left(\frac{\hbar^2 k^2}{2\mu} - \frac{\hbar^2 k'^2}{2\mu}\right) = \frac{\mu}{\hbar^2|k'|}\delta(|k| - |k'|)\delta_{\text{sgn}(k),\text{sgn}(k')}, \tag{5.24}$$

such that we have

$$\begin{aligned}\delta\left(\frac{\hbar^2 k^2}{2\mu} - \frac{\hbar^2 k'^2}{2\mu}\right)\delta(k-k') &= \frac{\mu}{\hbar^2|k'|}\delta(|k|-|k'|)\delta(|k|-|k'|)\delta_{\text{sgn}(k),\text{sgn}(k')}\\ &= \frac{\hbar^2|k'|}{\mu}\delta_{\text{sgn}(k),\text{sgn}(k')}\left[\delta\left(\frac{\hbar^2 k^2}{2\mu} - \frac{\hbar^2 k'^2}{2\mu}\right)\right]^2\\ &\approx \frac{\hbar|k'|\Delta t}{2\pi\mu}\delta_{\text{sgn}(k),\text{sgn}(k')}\delta\left(\frac{\hbar^2 k^2}{2\mu} - \frac{\hbar^2 k'^2}{2\mu}\right)\\ &= \frac{\Delta t}{2\pi\hbar}\delta(k-k') \end{aligned} \tag{5.25}$$

and we see, that the approximation (5.23) also holds in the one-dimensional case.

The T-matrix is the part, which strongly depends on the dimensionality of the system. This is not surprising, considering that in the Boltzmann approach (chapter 4), we have incorporated the part of the T-matrix that described lateral collisions, which in a 1D

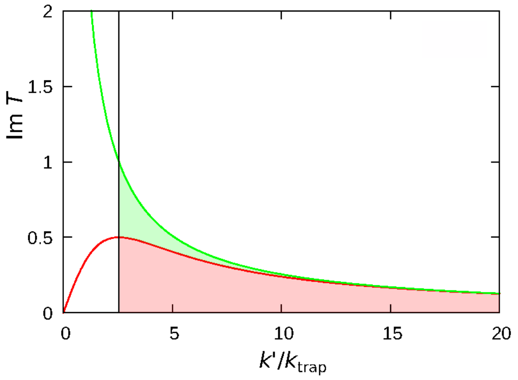

Figure 5.1: Comparison of the imaginary part of the T-matrix (5.30) (red) with the expansion (5.32) (green) for a small coupling constant $g_S^{1\text{D}}$. To avoid the singularity at $k' = 0$ we choose $T_S = 0$ inside the region $|k'| \leq \frac{Mg_S^{1\text{D}}}{2\hbar^2}$ indicated by the black line. The wave vector is scaled in terms of the trapping frequency: $k_{\text{trap}} = \sqrt{M\omega/\hbar}$. Figure taken from Ref. [59].

system are naturally restricted to backwards scattering and hence expected to differ considerably from the 3D case, and other geometries as well.

In the one-dimensional two-body scattering problem, in the center-of-mass frame, the Hamiltonian reads

$$H = \frac{-\hbar^2}{2\mu}\frac{\mathrm{d}^2}{\mathrm{d}x^2} + g_S^{1\text{D}}\delta(x), \tag{5.26}$$

where $g_S^{1\text{D}}$ is the 1D coupling constant introduced above. The wave function is of the form

$$\psi(x) = \mathrm{e}^{ikx} + \psi_{\text{sc}}(x), \tag{5.27}$$

where the scattered wave function is now given by $\psi_{\text{sc}}(x) = f_{k'}\mathrm{e}^{ik'|x|}$. Solving the stationary Schrödinger equation yields

$$f_{k'} = \frac{-1}{1 - i\hbar^2 k'/\mu g_S^{1\text{D}}} \tag{5.28}$$

for the scattering amplitude.

The Green's function, which related the scattered wave function with the T-matrix has the one-dimensional form

$$G(x) = \frac{2\mu}{\hbar^2}\int dk' \frac{\mathrm{e}^{ik'x}}{k^2 + k'^2 + i0^+} = 2\pi\frac{i\mu}{\hbar^2 k}\mathrm{e}^{ik|x|}, \tag{5.29}$$

such that

$$T_S(k,k') = \frac{1}{2\pi}\frac{ik'\frac{2\hbar^2}{M}}{1 - ik'\frac{2\hbar^2}{Mg_S^{1\text{D}}}}. \tag{5.30}$$

Likewise, in the case of spin-changing collisions, where the particles are subject to a quadratic Zeeman shift, incoming and outgoing wave vectors are related by $|k'| = \sqrt{k^2 + Q}$.

When we now perform the next step, the low energy expansion of the T-matrix, we encounter a problem absent in the 3D case. Now, the imaginary part of the T-matrix is given by

$$\mathrm{Im}T_S(k,k') = \frac{1}{2\pi} \frac{k' \frac{2\hbar^2}{M}}{1 + \frac{k'^2 4\hbar^4}{(M g_S^{1\mathrm{D}})^2}} \tag{5.31}$$

and an expansion in powers of g_S produces a singularity for $k' = 0$, since

$$\mathrm{Im}T_S(k,k') = \frac{1}{2\pi} \frac{(g_S^{1\mathrm{D}})^2 M}{2\hbar^2 k'} + \dots . \tag{5.32}$$

This singularity is artificial and we use a cutoff to circumvent it. We choose the cutoff to be the maximum of $\mathrm{Im}T$ at $k' = \frac{M g_S}{2\hbar^2}$, as depicted in Figure 5.1. So we use the expression

$$T_S(k,k') \approx \frac{g_S^{1\mathrm{D}}}{2\pi} - \begin{cases} 0 & \text{if } |k'| < \frac{M g_S^{1\mathrm{D}}}{2\hbar^2} \\ \frac{iM(g_S^{1\mathrm{D}})^2}{4\pi\hbar^2 k'} + \dots & \text{if } |k'| \geq \frac{M g_S^{1\mathrm{D}}}{2\hbar^2} \end{cases} . \tag{5.33}$$

to expand the T-matrix. Transformation into the basis of individual spins using the identity

$$T_{klmn}(k,k') = \sum_{SM} T_S(k,k') \left\langle km|SM\right\rangle \left\langle SM|ln\right\rangle \tag{5.34}$$

yields

$$T_{klmn}(k,k') \approx \frac{U_{knml}^{1\mathrm{D}}}{2\pi} - \begin{cases} 0 & \text{if } |k'| < \frac{M U_{knml}^{1\mathrm{D}}}{2\hbar^2} \\ \frac{iM\tilde{U}_{knml}^{1\mathrm{D}}}{4\pi\hbar^2 M k'} + \dots & \text{if } |k'| \geq \frac{M U_{knml}^{1\mathrm{D}}}{2\hbar^2} \end{cases} , \tag{5.35}$$

where

$$U_{klmn}^{1\mathrm{D}} = \sum_{SM} g_S^{1\mathrm{D}} \left\langle km|SM\right\rangle \left\langle SM|ln\right\rangle , \qquad \tilde{U}_{klmn}^{1\mathrm{D}} = \sum_{SM} (g_S^{1\mathrm{D}})^2 \left\langle km|SM\right\rangle \left\langle SM|ln\right\rangle . \tag{5.36}$$

With all approximations performed for the 1D case, we obtain an expression for the Boltzmann equation also in this regime. Here we note as well, that the terms linear in

a_S match the mean-field result (5.11)

$$\begin{aligned}
\frac{d}{dt}W_{mn}(x,p) + \frac{p}{M}\cdot\partial_x W_{mn}(x,p) + \frac{i}{\hbar}\sum_l \left[V_{nl}(x)W_{ml}(x,p) - W_{lm}(x,p)V_{ln}(x)\right] \\
- \frac{1}{2}\sum_l \left\{\partial_x V_{nl}(x)\cdot\partial_p W_{ml}(x,p) + \partial_p W_{lm}(x,p)\cdot\partial_x V_{ln}(x)\right\} \\
= -\frac{M}{\hbar^2}\sum_{abl}\Bigg[\int_{q^2>\epsilon_m} dq\frac{\tilde{U}^{\mathrm{1D}}_{malb}}{\sqrt{q^2+\Delta_{mlab}}}W_{an}(x,p)W_{bl}(x,p-q) \\
+ \int_{q^2>\epsilon_n} dq\frac{\tilde{U}^{\mathrm{1D}}_{nalb}}{\sqrt{q^2+\Delta_{nlab}}}W_{ma}(x,p)W_{lb}(x,p-q) \\
- \sum_{abcdl}\int_{q^2>\epsilon'} dq\frac{U^{\mathrm{1D}}_{malb}U^{\mathrm{1D}}_{ncld}}{\hbar\bar{k}}W_{ac}(x,p-\tfrac{1}{2}(q-\hbar\bar{k}))W_{bd}(x,p-\tfrac{1}{2}(q+\hbar\bar{k}))\Bigg].
\end{aligned} \tag{5.37}$$

The infrared cutoffs are given by $\epsilon_1 = \frac{MU_{malb}}{\hbar} - \Delta_{mlab}$, $\epsilon_2 = \frac{MU_{nalb}}{\hbar} - \Delta_{nlab}$ and $\epsilon_3 = \frac{MU_{nalb}}{2\hbar}(U_{malb} + U_{ncld}) - \Delta_{mnlabcd}$. This equation is a main result of this thesis. We implement it numerically without further approximations (apart from those performed in the numerical implementation, see appendix C for details) and use it to generate the theoretical results in chapter 10, where it shows very good agreement with experimental results.

A comparison of this equation with the 3D result Eq. (4.54) yields an interesting feature. While the mean-field terms (3.22) and (5.11) differ only in a rescaled coupling constant, the collision integral has a different dependence on momenta in both cases. In the 3D case, the pair of Wigner functions has a prefactor $\propto k$, while in 1D it is $\propto k^{-1}$. This means, that we can expect different dependence of the incoherent scattering processes on crucial parameters such as density. In fact, our results in chapter 10 (see e.g. Figure 10.3)) show that the 1D system does not simply act as a rescaled 3D system. The relative strength of coherent (mean-field) collisions compared to incoherent scattering is expected to increase for higher densities in the 1D case but decrease in three dimensions.

Chapter 6

Dynamically induced long-range interactions

In this section we investigate the case, where the interaction-induced dynamics of the system, such as spin-waves or spin oscillations, are very slow compared to the free particle motion induced by the harmonic trap. If this is the case, we can derive a simplified kinetic equation by time-averaging the mean-field potential (3.17) over a trapping period and eliminate the kinetic and trapping terms from the equation (3.22). This simplified description – when valid – has a large impact, since it can stabilize the initial phase-space distribution of the system while the dynamics of the system effectively only occur in spin space, leading to a suppression of spatial dephasing and collective spin dynamics even in nondegenerate Bose and Fermi systems [56, 58].

6.1 Dimensionless units

For our purposes, it is convenient here to switch to dimensionless units. In the case, where the trap is the dominating source of dynamics, we choose to scale our units with the trapping frequencies ω_i, $i = x, y, z$. Lengths are then given in units of $\sqrt{\hbar/M\omega_i}$ and momenta in units of $\sqrt{M\hbar\omega_i}$, and energy, angular frequency and time with $\hbar\bar{\omega}$, $\bar{\omega}$, and $1/\bar{\omega}$, where $\bar{\omega} = \sqrt[3]{\omega_x\omega_y\omega_z}$. With this choice of units, the leading order of the collisionless kinetic equation (3.22) reads

$$\frac{\mathrm{d}}{\mathrm{d}t}\hat{W}(\vec{x},\vec{p}) + \vec{p}\cdot\nabla_x\hat{W}(\vec{x},\vec{p}) - \vec{x}\cdot\nabla_p\hat{W}(\vec{x},\vec{p}) = i\left[\hat{V}^{\mathrm{mf}}(\vec{x}),\hat{W}(\vec{x},\vec{p})\right]. \tag{6.1}$$

The anticommutator in Eq. (3.22) is generally very small, and in this case of weak interactions it is often safe to neglect it completely, with the exception of the trap and external field gradients. Here, we neglect inhomogeneous external fields, and have split the term corresponding to the harmonic trap from the usual combined potential term, meaning that the (classical) terms describing free motion in the trap are on the left hand side of (6.1), and the mean-field interactions on the right hand side. In dimensionless

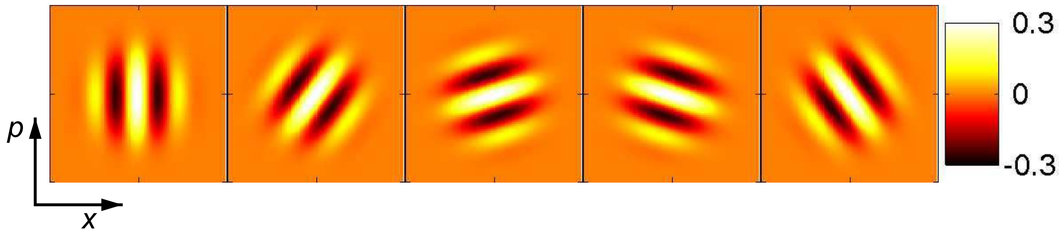

Figure 6.1: Motion of the Wigner function in a harmonic trap for a non-interacting system. During a single trapping cycle $\tau_{\text{trap}} = 2\pi/\omega$ the function rotates around the origin. Each point in phase-space follows its classical trajectory.

units, the mean-field potential is given as

$$V_{mn}^{\text{mf}}(\vec{x}) = \int d^3p \sum_{kl} \bar{U}_{klnm} W_{kl}(\vec{x}, \vec{p}), \tag{6.2}$$

with $\bar{U}_{klmn} = \sum_{SM} \bar{g}_S \langle km|SM\rangle \langle SM|ln\rangle$ and dimensionless 3D coupling constants $g_S = 4\pi\sqrt{\frac{\bar{\omega}M}{\hbar}} a_S$.

6.2 One-dimensional case

To show the essence of the effect of dynamically induced long-range interaction with a far less technical description, let us first consider the 1D system introduced above in section (5.1). The effect of the trap, in the phase-space picture, is a rotation of the Wigner function around the origin with frequency ω (see Figure 6.1). Hence, the spin state of a volume element in phase space moves along the classical trajectory (see Figure 6.1). If this rotation is faster than any interaction-induced dynamical processes, such that we can separate the time-scales, we can average it over a trapping cycle and obtain an effective interaction. For this purpose, we change coordinates and transform into the frame, which rotates with the trapping frequency:

$$x' = x\cos(t) - p\sin(t) \qquad p' = p\cos(t) + x\sin(t), \tag{6.3}$$

where functions transform according to

$$f'(x', p', t) = f(x(x', p', t), p(x', p', t), t). \tag{6.4}$$

In this coordinate system, the kinetic energy and trap vanish from the equation, and only the interaction part remains, described by the mean-field potential

$$V'^{\text{mf}}_{mn}(x', p', t) = 2\sum_{kl} \int ds \bar{U}^{\text{1D}}_{klnm} W'_{kl}(x' - s\sin(t), p' + s\cos(t), t), \tag{6.5}$$

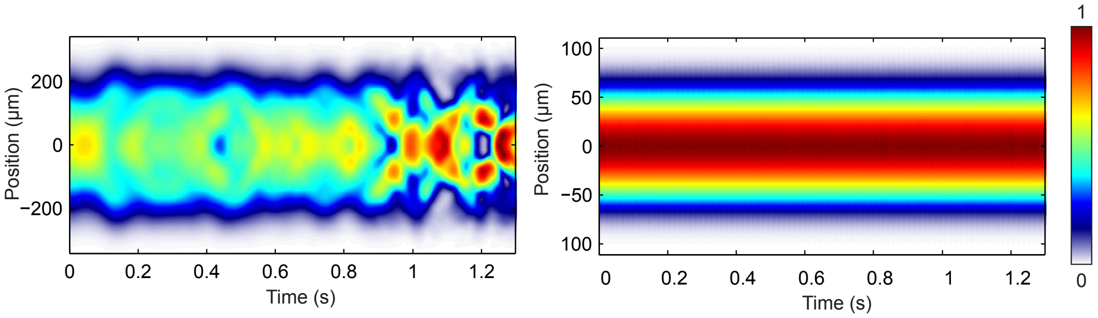

Figure 6.2: Effect of dynamically induced long-range interactions on spinor dynamics in a $F = 9/2$ system of ^{40}K. Evolution of the normalized spatial density $n(x,t)/N$ of the $m = 1/2$ component during spin-oscillations and interactions with the other spin-components [58]. Left: Low axial frequency, complex spatial structures evolve and spin oscillations are suppressed by dephasing. Right: High axial frequency, dynamically induced long-range interactions remove spatial dephasing. In both cases, trapping frequencies are chosen such that the, density, particle number and Fermi energy remain the equal. Figure taken from Ref. [58].

where $W'_{kl}(x',p',t) = W_{kl}(x(x',p'),p(x',p'),t)$ is the Wigner function in the new coordinates and we introduced the dimensionless 1D coupling constants

$$\bar{U}^{\mathrm{1D}}_{klmn} = \sum_{SM} \bar{g}^{\mathrm{1D}}_S \langle km|SM\rangle \langle SM|ln\rangle$$

with $\bar{g}^{\mathrm{1D}}_S = 2\sqrt{M\omega_y\omega_z/\hbar\omega} a_S$. Without kinetic and trapping term, Eq. (6.1) in the rotating frame becomes

$$\frac{\mathrm{d}}{\mathrm{d}t}\hat{W}'(x',p',t) = i\left[\hat{V'}^{\mathrm{mf}}(x',p',t), \hat{W}'(x',p',t)\right]. \tag{6.6}$$

A time-average of (6.5) over a trapping period, $(2\pi)^{-1}\int_0^{2\pi} dt V^{\mathrm{mf}}_{mn}(x',p',t)$, results in the effective potential

$$\begin{aligned} V^{\mathrm{eff}}_{mn}(x',p',t) &= \frac{1}{\pi}\sum_{kl}\int_0^{2\pi} dt \int ds \bar{U}_{klnm} W'_{kl}(x' - s\sin(t), p' + s\cos(t), t) \\ &= \sum_{kl}\int d\tilde{x}\int d\tilde{p} \frac{\bar{U}_{klnm}}{\pi\sqrt{\tilde{x}^2+\tilde{p}^2}} W'_{kl}(x'+\tilde{x}, p'+\tilde{p}, t), \end{aligned} \tag{6.7}$$

which is long-range in both position and momentum, as well as isotropic in phase-space. The intuition here is, that while in the original coordinates, interactions are short-range in position space, but infinite range in momentum space, the rapid motion ensures that each atom interacts with all atoms in the trap during a cycle, but not equally, resulting in the $\propto (x^2+p^2)^{-1/2}$-behavior of this effective interaction.

If we slightly reformulate the expression for the effective time-averaged mean-field potential (6.7),

$$V_{mn}^{\text{eff}}(x', p', t) = \sum_{kl} \int d\tilde{x} \int d\tilde{p} \frac{\bar{U}_{klnm}}{\pi\sqrt{(\tilde{x}-x')^2 + (\tilde{p}-p')^2}} W'_{kl}(\tilde{x}, \tilde{p}, t), \tag{6.8}$$

we see that it is of the form of an integral transformation $g(x) = \int dy K(x-y) f(y)$. Its effect here is to blur out spatial structures of the Wigner function, while keeping the overall shape intact. This broadening of the mean-field potential counteracts dephasing. We illustrate this in Figure 6.2, where the time evolution of a spin component is shown for two 1D systems, where in one case the trapping frequency is low and in the other case it is sufficiently high to justify the time average in (6.7).

6.3 Two or three dimensions: Commensurate trap frequencies

In the case of $d > 1$ dimensions, the discussion above becomes more complicated and technical, since there are now more than one trapping period involved, making the notion of time-averaging less trivial. In the following, we distinguish two cases.

If the trap frequencies are commensurate, we can average over a time span given by the least common divisor T_{lcd} of the periods $T_i = 2\pi/\omega_i$, provided that T_{lcd} is much smaller than the timescale T_{int} associated with interaction induced dynamics dominated by the commutator in Eq. (3.22), $T_{\text{lcd}} \ll T_{\text{int}}$. This gives

$$V_{mn}^{\text{eff}}(\vec{x}', \vec{p}', t) = \frac{2}{T_{\text{lcd}}} \sum_{kl} \int_0^{T_{\text{lcd}}} d\tau \int d^d a \bar{U}_{klnm} W'_{kl}\left(\vec{x}' + \vec{u}(a,\tau), \vec{p}' + \vec{v}(a,\tau), t\right). \tag{6.9}$$

Thus each phase space point $(\vec{x}', \vec{p}')$ interacts via the mean-field potential with the $d+1$-dimensional subspace of the $2d$-dimensional phase space covered by the coordinates $(\vec{x}' + \vec{u}(a,\tau), \vec{p}' + \vec{v}(a,\tau), t)$ during integration. It is not possible to find a compact general expression.

6.4 Incommensurate trap frequencies

If the trap frequencies are pairwise incommensurate, such that $T_{\text{lcd}} \to \infty$ or simply if T_{lcd} becomes large compared to the individual periods T_i, we can still approximate the mean-field potential by an effective time-averaged one. However, in this case a double separation of timescales $\max(T_i) \ll T_{\text{av}} \ll T_{\text{int}}$ is required, with T_{av} denoting the interval over which the time average is to be taken. This interval must be large compared to the individual periods T_i, such that $T_{\text{av}} \approx n_i T_i$ with integers $n_i \gg 1$. Excluding resonance effects between the dynamics along the different trap directions one can, in a second step, assume independent averages along the individual trap dimensions

$$
\begin{aligned}
V^{\mathrm{eff}}_{mn}(\vec{x}',\vec{p}',t) &= \frac{2}{T_{\mathrm{av}}}\sum_{kl}\int_0^{T_{\mathrm{av}}} d\tau \int d^d a \bar{U}_{klnm} W'_{kl}\left(\vec{x}'+\vec{u}(a,\tau),\vec{p}'+\vec{v}(a,\tau),t\right) \\
&\approx \frac{1}{\pi}\sum_{kl}\int_0^{2\pi} d\phi_1 \int_{-\infty}^{\infty} da_1 \ldots \int_0^{2\pi} d\phi_d \int_{-\infty}^{\infty} da_d \bar{U}_{klnm} W'_{kl}\left(\vec{x}'+\vec{u}(a,\tau),\vec{p}'+\vec{v}(a,\tau),t\right) \\
&\approx \sum_{kl}\bar{U}_{klnm}\int d^d u \int d^d v \left[\prod_{i=1}^{d}\frac{\pi^{-1}}{\sqrt{u_i^2+v_i^2}}\right] W'_{kl}\left(\vec{x}'+\vec{u},\vec{p}'+\vec{v},t\right). \qquad (6.10)
\end{aligned}
$$

Thus, we arrive at a mean-field potential corresponding to an anisotropic long-range interaction of the type

$$
\bar{g}_S \sum_{i=1}^{d} \pi^{-1}\left((x^{(1)}-x^{(2)})^2+(p^{(1)}-p^{(2)})^2\right)^{-1/2} \qquad (6.11)
$$

between two particles 1 and 2 in phase space. Later in this thesis, in chapter 9, we will see, that this effect reduces spatial dephasing and thus allows for the observation of long-lived large-amplitude spin oscillations [58].

6.5 Quasi-1D approximation

The effect of a dynamically induced long-range interaction described above has important consequences. If we assume a trapped 3D system to have two trapping frequencies ω_y, ω_z sufficiently high to induce this effect, we can again assume a quasi stationary behavior of the Wigner function in these two directions. This means we can define the *quasi 1D* regime, in which the spatial dynamics of the system is effectively suppressed in two dimensions by the rapid oscillation in the trap, as a result of dynamically induced long-range interactions. This is different from the 1D case described in chapter 5, where we can assume there is no dynamics along these directions, because all particles occupy the transversal ground state. Here, the levels of the harmonic trap are macroscopically occupied in all directions.

In this regime, we obtain a one-dimensional Wigner function by integrating out the radial dimensions

$$
W^{\|}_{mn}(x,p) = \int dy \int dz \int dp_y \int dp_z W_{mn}(\vec{x},\vec{p}). \qquad (6.12)
$$

As we show later in this thesis, we generally consider initial Wigner functions of the product form

$$
W_{mn}(\vec{x},\vec{p},t=0) = M_{mn} f_0(\vec{x},\vec{p}), \qquad (6.13)
$$

where $f_0(\vec{x},\vec{p})$ is a phase-space distribution corresponding to the equilibrium state of a two-component gas. The matrix M_{mn} describes a global spin state occupied by all particles, which is usually prepared sufficiently rapidly, that f_0 remains unchanged. We approximate f_0 with the phase-space distribution for a non-interacting Fermi gas,

$$f_0(\vec{x},\vec{p}) = \frac{1}{(2\pi\hbar)^3}\left\{\exp\left(\frac{1}{k_\mathrm{B}T}\left[\frac{\vec{p}^2}{2M}+\frac{1}{2}M\left(\omega_x^2x^2+\omega_y^2y^2+\omega_z^2z^2\right)-\mu\right]\right)+1\right\}^{-1}. \tag{6.14}$$

The dimensionally reduced Wigner function (6.13) is then given by

$$W^{||}_{mn}(x,p,t=0) = M_{mn}f_0^{||}(x,p), \tag{6.15}$$

where $f_0^{||}(x,p) = \int dy \int dz \int dp_y \int dp_z f_0(\vec{x},\vec{p})$. Seeing, how in general the spin dynamics driven by the commutator in Eq. (3.22) dominate, while the anticommutator, which governs changes to the shape of the total density, has only a negligible effect (see e.g. chapter 8, where in the experiment no deformation is observed), we assume the Wigner function (6.14) to maintain its transversal component at each phase-space position (x,p). Hence, we we make the Ansatz

$$W_{mn}(\vec{x},\vec{p},t) = W^{||}_{mn}(x,p,t)\Lambda(\vec{x},\vec{p}) \tag{6.16}$$

for the full Wigner function at time t to close the connection between the 3D Wigner function and the one in reduced dimensions. Integrating Eq. (6.16) over the radial dimensions and comparing it at $t=0$ with (6.13) yields

$$\Lambda(\vec{x},\vec{p}) = \frac{f_0(\vec{x},\vec{p})}{f_0^{||}(x,p)}. \tag{6.17}$$

Note the explicit dependence of Λ on x, p. This is different from similar work on thermal gases [40, 41, 65], where the Wigner function can be expressed as a Boltzmann distribution, a Gaussian, which automatically separates into a product of its x, y and z components: $f_0(\vec{x},\vec{p}) = f_x(x,p)f_y(y,p_y)f_z(z,p_z)$, where each factor can be integrated out separately. For large temperatures, our distribution (6.14) also becomes a Gaussian and $\Lambda(\vec{x},\vec{p})$ loses its phase-space dependence.

Next, we substitute (6.16) into the mean-field equation of motion (3.22), and obtain its quasi 1D-version by integrating out the radial phase-space coordinates:

$$\frac{\mathrm{d}}{\mathrm{d}t}\hat{W}^{||}(x,p)+\frac{p}{M}\partial_x\hat{W}^{||}(x,p) = \frac{i}{\hbar}\left[\hat{V}^{||}(x,p),\hat{W}^{||}(x,p)\right]+\frac{1}{2}\left\{\partial_x\hat{V}^{||}(x,p),\partial_p\hat{W}^{||}(x,p)\right\}. \tag{6.18}$$

The axial part of the mean-field potential is given by

$$V^{||}_{mn}(x,p) = 2\sum_{kl}U_{klnm}\int dy\int dz\int dp_y\int dp_z\Lambda(\vec{x},\vec{p})\Lambda(\vec{x},\vec{p})\int dpW^{||}_{kl}(x,p), \tag{6.19}$$

hence it has a dependence on momentum as well. This equation describes systems well, where two trapping frequencies are very high and all spatial dynamics appears along the radial direction. The experiments on spin waves in chapter 8 were performed in this regime with very good agreement of results obtained using Eq. 6.18 to the experiment.

6.6 Single-mode approximation

6.6.1 3D case

A special case happens when all three trapping frequencies are sufficiently high, such that we can assume a time-dependent long-range interaction in every direction. If we take the initial Wigner function to be of a product form (6.13), as we approximate the experimentally generated initial states as (see section 8.1), we can assume it to approximately keep this product form over time,

$$W_{mn}(\vec{x},\vec{p},t) = M_{mn}(t) f_0(\vec{x},\vec{p}), \tag{6.20}$$

without significant changes to its phase-space distribution. Hence we can completely integrate out the phase-space dependence and end up with a simple equation for the spin-components only,

$$\frac{d}{dt} M_{mn}(t) + Q(n^2 - m^2) M_{mn} = \frac{2\eta}{i\hbar} \sum_{jkl} \left[U_{mjlk} M_{jn} M_{kl} - U_{jnkl} M_{mj} M_{lk} \right], \tag{6.21}$$

where

$$\eta = \frac{1}{N} \int d^3x \int d^3p \int d^3q f_0(\vec{x},\vec{p}) f_0(\vec{x},\vec{q}). \tag{6.22}$$

Due to its similarity to the single-mode approximation (SMA) used to describe spinor BEC, we also call our approach single-mode approximation, but keep in mind that in a Fermi gas, many modes are occupied. The very simple equation (6.21) rather accurately describes spin dynamics in the regime, where all three trapping frequencies are sufficiently high. The consequence is that the dynamically induced long-range interactions stabilize the phase-space distribution of the system and reduce spatial dephasing. The spin degree of freedom then evolves collectively for all particles, despite their Fermi statistics [58].

We can go further and substitute the product expression (6.20) into the collision integral as well. This leads to an extension of Eq. (6.18),

$$\begin{aligned}
\frac{d}{dt} M_{mn}(t) + Q(n^2 - m^2) M_{mn} = {} & \frac{2\eta}{i\hbar} \sum_{jkl} \left[U_{mjlk} M_{jn} M_{kl} - U_{jnkl} M_{mj} M_{lk} \right] \\
& - \frac{M}{4\pi\hbar^4} \left\{ \sum_{abl} \left(\lambda^{(1)}_{mlab} \tilde{U}_{malb} M_{an} M_{bl} + \lambda^{(1)}_{nlab} \tilde{U}_{nalb} M_{ma} M_{lb} \right) \right. \\
& \left. - \sum_{abcdl} \lambda^{(2)}_{mnlabcd} U_{malb} U_{ncld} M_{ac} M_{bd} \right\},
\end{aligned} \tag{6.23}$$

where the spin-dependent integrals $\lambda^{(1,2)}$ are given by

$$\lambda^{(1)}_{abcd} = \frac{1}{N} \int d^3x \int d^3p \int d^3q \sqrt{\vec{q}^2 + \Delta_{abcd}} f_0(\vec{x},\vec{p}) f_0(\vec{x},\vec{p}-\vec{q}), \tag{6.24}$$

and

$$\lambda^{(2)}_{mnlabcd} = \frac{1}{N}\int d^3x \int d^3p \int d^3q \sqrt{\vec{q}^2 + \Delta_{mnlabcd}} f_0(\vec{x},\vec{p}) f_0(\vec{x},\vec{p}-\vec{q}), \tag{6.25}$$

respectively. However, this approximation neglects variations in the phase-space distribution of the individual spin components from recombination via lateral collisions. Despite this, the agreement with experimental results is still very good, as shown in chapter 9.

6.6.2 1D case

A true 1D system can also be treated in the single-mode approximation. In this case, the momentum dependence of the integrals λ is different, given by

$$\lambda'^{(1)}_{abcd} = \frac{1}{N}\int dx \int dp \int_{q^2>\epsilon_{1,2}} dq \frac{f_0(x,p) f_0(x,p-q)}{\sqrt{q^2 + \Delta_{abcd}}}, \tag{6.26}$$

and

$$\lambda'^{(2)}_{mnlabcd} = \frac{1}{N}\int dx \int dp \int_{q^2>\epsilon_3} dq \frac{f_0(x,p) f_0(x,p-q)}{\sqrt{q^2 + \Delta_{mnlabcd}}}, \tag{6.27}$$

The single-mode equation of motion in a 1D system reads

$$\begin{aligned}
\frac{d}{dt}M_{mn}(t) + Q(n^2-m^2)M_{mn} = {} & \frac{2\eta}{i\hbar}\sum_{jkl}\left[U^{\mathrm{1D}}_{mjlk}M_{jn}M_{kl} - U^{\mathrm{1D}}_{jnkl}M_{mj}M_{lk}\right] \\
& - \frac{M}{4\pi\hbar^4}\left\{\sum_{abl}\left(\lambda'^{(1)}_{mlab}\tilde{U}^{\mathrm{1D}}_{malb}M_{an}M_{bl} + \lambda'^{(1)}_{nlab}\tilde{U}^{\mathrm{1D}}_{nalb}M_{ma}M_{lb}\right)\right. \\
& \left. - \sum_{abcdl}\lambda'^{(2)}_{mnlabcd}U^{\mathrm{1D}}_{malb}U^{\mathrm{1D}}_{ncld}M_{ac}M_{bd}\right\},
\end{aligned} \tag{6.28}$$

in the 1D case. Here, $f_0(x,p)$ denotes the 1D equilibrium distribution

$$f_0(x,p) = \frac{1}{2\pi\hbar}\left\{\exp\left(\frac{1}{k_{\mathrm{B}}T}\left[\frac{p^2}{2M} + \frac{1}{2}M\omega^2x^2 - \mu\right]\right) + 1\right\}^{-1}. \tag{6.29}$$

In the 1D case, we can directly compare the full Boltzmann equation (5.37) to single-mode results. We find good agreement when it comes to describing purely mean-field dynamics [58], but the application of the single-mode approximation to the collision integral cannot be considered accurate. Spin-conserving lateral collisions will naturally lead to a deformation of the phase-space distribution, which is unaccounted for in the single-mode approximation, hence we expect effects related to these collisions to be strongly underestimated.

Part II

Application to trapped Fermi gases

Chapter 7

Spin segregation for $F = 1/2$

In this chapter we discuss mean-field driven spin segregation in a spin-1/2 system. Before dealing with larger spins and spin-changing collisions, we would like to first study mean-field dynamics in phase space in the collisionless regime and in order to illustrate the role of the trap on spin dynamics. In such a two-component system, mean-field interactions take the form of an effective magnetic field [56, 64, 65, 77], that is proportional to the local spin polarization. We will see in this chapter, as well as in the subsequent chapters, that mean-field driven dynamics strongly depend on the off-diagonal elements of the single-particle Wigner function (3.3). Here, in the spin-1/2 case, these matrix elements correspond to the components of this effective magnetic field, which are orthogonal to the quantization axis. These matrix elements are responsible for the fastest interaction-driven processes in spinor Fermi gases, since they appear in the leading term of the semi-classical expansion, the commutator in equations (3.22) and (4.55). Here, we study scenarios, in which the atoms in the two spin components $\uparrow, \downarrow$ separate dynamically as a transient effect into two domains in phase-space.

We start with a reproduction of the results of Ref. [65], a theoretical discussion of the effect termed *anomalous spin segregation* in Ref. [81] and observed in ultracold ^{6}Li. This work was performed as a test of the simulation created to numerically integrate equation (3.22). The second study on spin segregation explores the time evolution of a spin spiral created using a magnetic field gradient [56]. In both cases, we use the parameters of a cold-atom system of ^{6}Li, where the atoms are trapped in two hyperfine ground states, $|\uparrow\rangle$ and $|\downarrow\rangle$, which makes the system an effective spin 1/2 gas. The scattering length between the two hyperfine states can be modified using a Feshbach resonance, and we consider the regime close to a zero crossing, where interactions are particularly weak, and a description using the collisionless mean-field equation (5.11) is adequate. We consider a 1D system as described in section 5.1, but in this section omit the superscript “1D” of the coupling constant.

7.1 The system

A magnetic field only contributes a linear Zeeman splitting to a two-level system, of which a constant (homogenous) part can be removed from the Hamiltonian by going into the rotating Larmor frame. Interactions in the spin 1/2 case are SU(2) symmetric [56] and thus the coupling constants (5.6) are given by

$$U_{ijkl} = g \sum_{S,M} \langle ik|SM\rangle \langle SM|jl\rangle = \frac{g}{2} \left(\delta_{ij}\delta_{kl} - \delta_{il}\delta_{kj} \right), \tag{7.1}$$

which further simplifies the Hamiltonian. It has the simple form

$$\begin{aligned} \hat{H} = \int dx \Bigg\{ & \sum_m \hat{\psi}^\dagger_m(x) \left[-\frac{\hbar^2 \partial_x^2}{2M} + \frac{1}{2} M \omega^2 x^2 \right] \hat{\psi}_m(x) + \sum_{mn} \vec{B}(x) \cdot \vec{\sigma}_{mn} \hat{\psi}^\dagger_m(x) \hat{\psi}_n(x) \\ & + \frac{g}{2} \hat{\psi}_\uparrow(x) \hat{\psi}_\uparrow(x) \hat{\psi}^\dagger_\downarrow(x) \hat{\psi}_\downarrow(x) \Bigg\}, \end{aligned} \tag{7.2}$$

where $\vec{\sigma}$ denotes the Pauli-matrices.

7.2 Anomalous spin segregation

The first effect we describe with this Hamiltonian is the anomalous spin segregation, which was observed in 2008 in the group of J. E. Thomas at Duke University [81]. It was later described theoretically by Natu and Mueller [65] using what corresponds to a spin 1/2 version of Eq. (5.11) in this thesis. Hence, section 7.2 of this thesis contains a reproduction of the results of Natu and Mueller and was used as the first test of our numerical simulations of Eq. (5.11), using its spin 1/2 special case. In the experimental setup, the behavior of the ^{6}Li Fermi gas was investigated close to a zero-crossing of a Feshbach resonance. It was found, that both spin components separate, one forming a shell around the other. In the theoretical work [65, 77], the mechanism was identified to be a slight mismatch of the trapping frequency experienced by atoms in the $\uparrow$ and $\downarrow$ states. Such a mismatch can e.g. occur in the presence of a magnetic field gradient, a common experimental problem. Tuning Feshbach resonances often requires very strong magnetic fields, which may have slight inhomogeneities along the atomic cloud in the trap. Here we use a 1D configuration to illustrate this effect, with an axial trapping frequency of $\omega_x \equiv \omega = 2\pi \times 60\,\text{Hz}$ and a radial frequency of $\omega_y = \omega_z \equiv 2\pi \times 36\,\text{kHz}$. The scattering length is tuned to be at $a = 4.55 a_0$, where a_0 is the Bohr radius. With a particle number of $N = 600$ at $T \approx 6\,\mu\text{K}$, the mean collision time in this system is $\tau \approx 1\,\text{s}$, justifying a collisionless description.

We assume the system to be prepared in a single spin-component ($\uparrow$), so it is initially non-interacting. The initial Wigner function in this thermal regime is approximately a Gaussian, as the gas is non-degenerate. It can be considered the same for both spin components $m, n = \uparrow, \downarrow$, so we assume each component to have the phase-space distribution

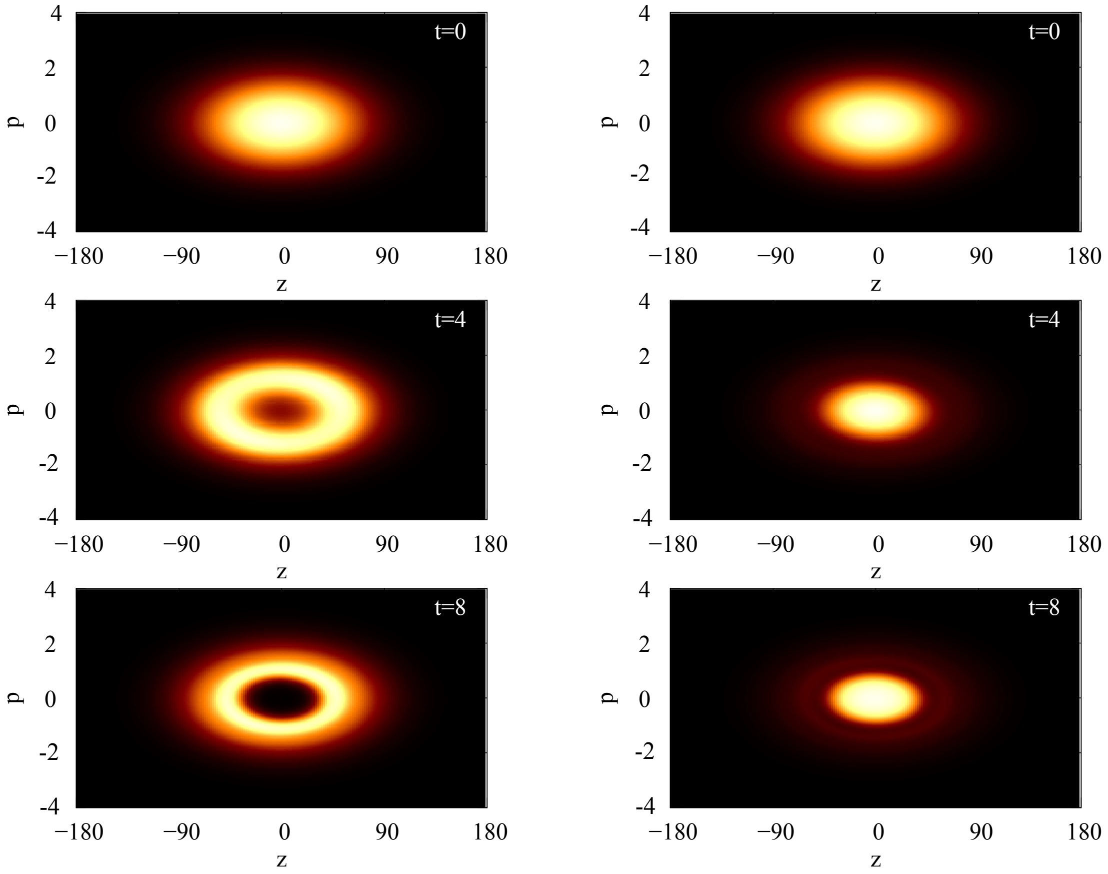

Figure 7.1: Snapshots of the phase-space-distribution for the spin components (↑ left, ↓ right) at $t = 0, 4, 8$ trapping periods.

of the spinless Fermi gas

$$W_{\uparrow\uparrow}(x, p, t = 0) = A \exp\left(-\beta \left[\frac{p^2}{2M} + \frac{1}{2}M\omega^2 x^2\right]\right). \tag{7.3}$$

This is a stationary state of the harmonic trap. Using a $\pi/2$-pulse, the spins are then rotated from pointing along the z-axis to the x-axis, where the Wigner-function reads

$$W_{mn}(x, p, t = 0) = A\sigma^x_{mn} \exp\left(-\beta \left[\frac{p^2}{2M} + \frac{1}{2}M\omega^2 x^2\right]\right). \tag{7.4}$$

In Figure 7.1, we show the time evolution of $W_{\uparrow\uparrow}$ and $W_{\downarrow\downarrow}$ from the initial state above in the case, that the ↓-component experiences a trapping frequency, which is slightly detuned from ω by $\delta\omega \approx 2\pi \times 10\,\text{mHz}$. The spin segregation occurs in the presence of interaction and this slight difference in the trap frequencies provides a symmetry break in spin space for the onset spin segregation [65, 77]. In Figure 7.2 we show the difference in

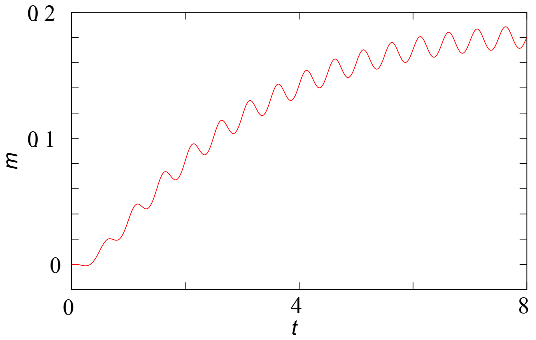

Figure 7.2: Difference of spin components ↑ and ↓ at the center of the trap during the time-evolution.

densities of the up and down-components at the center of the trap as a function of time. Both figures reproduce the results of Ref. [65, 77, 81], where a more detailed description of he effect can be found.

7.3 Spin-segregation via dynamically-induced long-range interactions

We now turn towards another effect, the spinor dynamics of a two-component Fermi gas far from equilibrium. The initial state now is created out of the spin-polarized equilibrium (6.29) by rotating the spins spatially into a spiral configuration (as was done for a Bose condensate [22] and proposed for strongly interacting fermions for the purpose of probing the Stoner transition [82]). Here, spin segregation builds up over time on a time-scale that is long compared to the oscillatory motion of the atoms in the trap and is explained as a consequence of dynamically created long-range interactions (see chapter 6).

The Hamiltonian is again given by Eq. (7.2), without the magnetic term that is absent in this setup, since we consider only a homogenous field during the time-evolution. The corresponding kinetic equation is

$$\left(\frac{\mathrm{d}}{\mathrm{d}t} + \frac{p}{M}\partial_x - M\omega^2 x\partial_p\right)\hat{W}(x,p) = -\frac{ig}{\hbar}\left[\hat{W}(x,p), \hat{n}(x)\right]$$
$$-\frac{g}{2}\left\{\partial_x\hat{n}(x), \partial_p\hat{W}(x,p)\right\} + g\mathrm{Tr}\left(\hat{n}(x)\right)\hat{W}(x,p). \tag{7.5}$$

Next, we note that in the spin 1/2 case, the Wigner function is a 2 × 2 hermitian matrix in spin-space. Hence we can expand it in the basis of Pauli matrices

$$W_{mn}(x,p) = W_0(x,p)\delta_{mn} + \vec{W}(x,p)\cdot\vec{\sigma}_{mn}, \tag{7.6}$$

into a scalar part

$$W_0(x,p) = \sum_m W_{mm}(x,p), \tag{7.7}$$

equal to the total phase-space density, and a vector part

$$\vec{W}(x,p) = \sum_{mn} W_{mn}(x,p)\vec{\sigma}_{nm}, \tag{7.8}$$

all of which are real. Interactions can be likewise expanded in Pauli-matrices

$$U_{ijkl} = \frac{g}{2}\left(\delta_{ij}\delta_{kl} - \delta_{il}\delta_{kj}\right) = g\left(\frac{1}{4}\delta_{ij}\delta_{kl} - \vec{\sigma}_{ij}\cdot\vec{\sigma}_{kl}\right). \tag{7.9}$$

This ferromagnetic shape of the interactions, as illustrated by the negative sign in front of the spin-spin-coupling term, can be understood intuitively from Pauli blocking. Due to Pauli blocking, parallel spins cannot interact, hence avoid repulsion, which leads to a ferromagnetic mean-field coupling. The resulting mean-field potential is given by

$$V^{\mathrm{mf}}_{mn}(x) = V_{\mathrm{mf}}(x)\delta_{mn} + \vec{B}_{\mathrm{mf}}(x)\cdot\vec{\sigma}_{mn}. \tag{7.10}$$

Noting the way in which the mean-field potential acts in the equation of motion, we can identify its scalar part,

$$V_{\mathrm{mf}}(x) = \frac{1}{2}gn_0(x), \tag{7.11}$$

as a correction to the trapping potential, and its spin-vector component,

$$\vec{B}_{\mathrm{mf}}(x) = -2g\vec{n}(x), \tag{7.12}$$

as an effective magnetic field.

Using equations. (7.10)-(7.12), the mean-field equation of motion (5.11) is given by

$$\begin{aligned}\frac{d}{dt}W_{mn}(x,p) = &-\frac{p}{M}\partial_x W_{mn}(x,p) + \left(\partial_x V(x)\right)\partial_p W_{mn}(x,p)\\ &-\frac{i}{\hbar}\vec{B}(x)\cdot\sum_k\left(\sigma_{mk}W_{nk}(x,p) - \sigma_{kn}W_{km}(x,p)\right)\\ &+\frac{1}{2}\left(\partial_x\vec{B}(x)\right)\cdot\partial_p\left(\sigma_{mk}W_{nk}(x,p) + \sigma_{kn}W_{km}(x,p)\right)\end{aligned} \tag{7.13}$$

and we can reformulate it into equations of motion for the scalar and vector components of the Wigner function and obtain

$$\begin{aligned}\frac{d}{dt}W_0(x,p) = &\left[-\frac{p}{M}\partial_x + M\omega^2 x\partial_p + \left(\partial_x V_{\mathrm{mf}}(x)\partial_p\right)\right]W_0(x,p)\\ &+\left(\partial_x\vec{B} + \partial_x\vec{B}_{\mathrm{mf}}(x)\right)\cdot\partial_p\vec{W}(x,p)\end{aligned} \tag{7.14}$$

$$\begin{aligned}\frac{d}{dt}\vec{W}(x,p) = &\left[-\frac{p}{M}\partial_x + M\omega^2 x\partial_p + \left(\vec{B} + \vec{B}_{\mathrm{mf}}(x)\right)\times + \left(\partial_x V_{\mathrm{mf}}(x)\partial_p\right)\right]\vec{W}(x,p)\\ &+\frac{1}{4}\partial_x\vec{B}_{\mathrm{mf}}(x)\partial_p W_0(x,p),\end{aligned} \tag{7.15}$$

where × denotes a vector product.

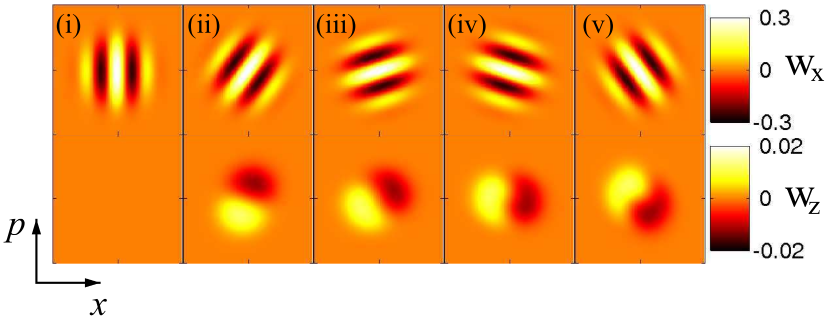

Figure 7.3: Wigner function components $W_x(x,p)$ and $W_z(x,p)$ at five times (i-v, shown in Figure 7.4) during the first half cycle, for $T = T_\mathrm{F}$ and $\lambda_s/\Delta = 0.5$. The motion in phase space is governed by an overall rotation at the trap frequency (see Figure 6.1), during which W_z slowly develops two domains. Figure taken from Ref. [56].

To initialize dynamics, we prepare the system by winding up a spin spiral along its longitudinal axis. For this, it is first prepared in a spin-polarized state, with all spins pointing in the x direction. This is a non-interacting equilibrium state, and the Wigner function of such a state is given by the phase-space distribution (6.29). We chose the same system parameters as above, with, $\omega = 2\pi \times 60\,\mathrm{Hz}$, $\omega_\perp = 2\pi \times 3.6\,\mathrm{kHz}$, $N = 100$ and $a = 4.5\,a_B$, and study the time evolution for different temperatures $T/T_\mathrm{F} = 0.2, 1, 5$. The next step is to apply a magnetic field gradient to the system for a very short time. The magnetic field is polarized along the z-axis, such that $\vec{B}(x) = (0, 0, B(x))$, with $B(x) = qx\delta(t)$. Larmor precession of the spins at different frequencies along x creates a spin spiral of wave length $\lambda_s = 2\pi/q$, and while $W_0(x,p)$ is still given by Eq. (6.29), the vector component of W has changed to

$$\vec{W}(x,p) = (\cos(qx), \sin(qx), 0)\,\frac{W_0(x,p)}{2}, \tag{7.16}$$

or equivalently

$$W_{mn}(x,p) = \exp(iqx(m-n))\frac{W_0(x,p)}{2}. \tag{7.17}$$

This simple manipulation has displaced the system into a state far from thermal equilibrium.

Apart from having created a spiral spin configuration – not favorable with respect to either energy or entropy –, we have also increased the number of available single-particle states from one spin state to two. This means, that the the phase-space density configuration (7.16) is far from being thermal, with the same kinetic energy as before but suddenly only half the number of particle in each spin state. Also, the system has become interacting, being no longer polarized with total magnetization zero.

On a short time scale of a single trapping cycle, the system evolves mainly as determined by the harmonic potential. That is, neglecting interaction completely for the moment, $W_{mn}(x,p)$ simply rotates in phase space at constant angular velocity ω. Everywhere, the Wigner function follows a classical circular orbit. This behavior can be

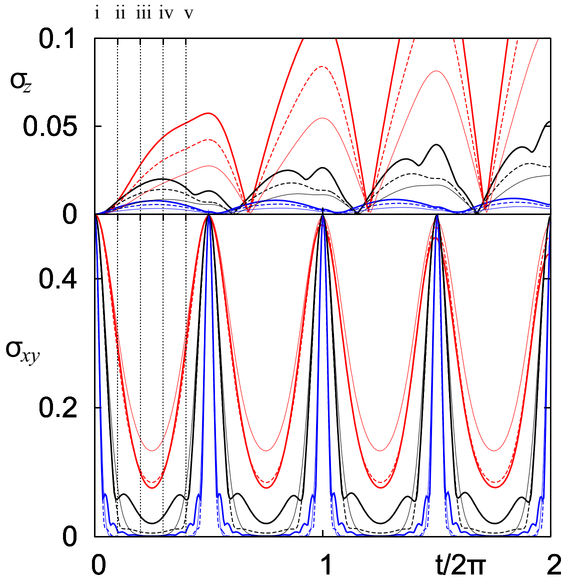

Figure 7.4: Time evolution of the averaged spatial polarizations σ_z and σ_{xy} for $T/T_\mathrm{F} = 0.2, 1, 5$ (thick solid, dashed, and thin solid lines, respectively) and for $\lambda_s/\Delta = 1, 0.5, 0.2$ (top triple of red lines, middle triple of black lines, and bottom triple of blue lines, respectively). While for the shorter wave lengths σ_{xy} shows rapid collapses followed by periodic revivals, the emerging spatial z-polarization undergoes smooth oscillations as a signature of the formation of only two domains in phase space. Figure taken from Ref. [56].

observed clearly in Figure 6.1, which shows the evolution of $W_x(x,p)$ during half a trap cycle. Looking only at the spatial polarization

$$\vec{n}(x) = \int dp\vec{W}(x,p), \tag{7.18}$$

obtained by projecting $\vec{W}(x,p)$ onto the x axis, this rotation manifests as periodic decay and revivals of the mean absolute spatial x-y-polarization

$$\sigma_{xy} = \frac{1}{N}\int dx\sqrt{n_x^2(x) + n_y^2(x)}, \tag{7.19}$$

as seen in Figure 7.4. for the first two cycles. The collapse and revival become more pronounced, the more windings we apply to the spiral.

When we add weak interactions to the picture, during a single cycle of oscillation in the trap they cause only small deviations from the non-interacting behavior. The small modification of the trap frequency and the slight anharmonicities caused by the scalar part of the mean-field potential through the anticommutator in (5.11) are negligible. However, $W_z(x,p)$, which is zero initially, changes and develops a pattern. This pattern is related to the magnetic mean-field $\vec{B}_\mathrm{mf}(x)$. Regardless of the winding number of

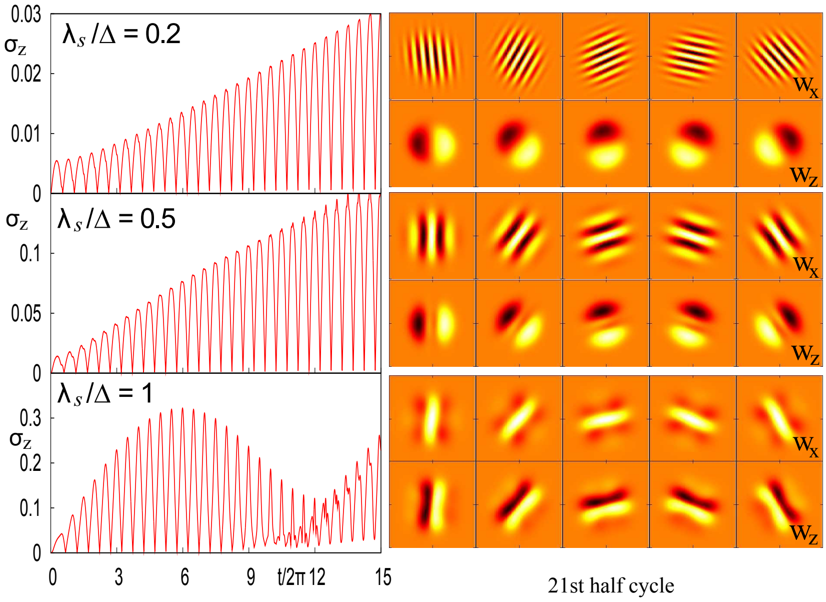

Figure 7.5: Evolution on longer times for $T = T_\mathrm{F}$ and different initial spiral wave lengths λ_s/Δ. (left) Averaged spatial absolute z polarization σ_z vs time. Note the different scaling of σ_z for each wave length. (right) Wigner function components $W_x(x,p)$ and $W_z(x,p)$ plotted for five instants in time as in Figure 7.3, but during the 21st half cycle (arbitrary color scale). Initially, σ_z increases linearly in time with a rate controlled by the wave length λ_s/Δ. Irrespective of the number of windings Δ/λ_s (directly visible in W_x), W_z develops two oppositely polarized domains. Figure taken from Ref. [56].

the initial spiral, two domains of opposite polarization with respect to z form. This formation of always two spin domains is a very robust effect. As a consequence of the spin segregation happening in phase space (see Figure 7.3), the average polarization with respect to the z-axis

$$\sigma_z = \frac{1}{N}\int dx \sqrt{n_z^2(x)}, \tag{7.20}$$

oscillates in time, but because only two domains are formed, it does not feature the same sharp collapses as σ_{xy} does for small values of λ_s/Δ, where Δ denoted the extension of the atomic cloud along the x-axis. This is depicted in Figure 7.4.

The long-time behavior of this spin segregation effect is shown in Figure 7.5 for three different spiral wave lengths λ_s: From cycle to cycle the spin segregation becomes more and more pronounced, as can be seen in the left panel of Figure 7.6, where σ_z during the 21st half cycle is shown. For the spatial dependence only, again the rotation in phase space of the two oppositely polarized domains corresponds to a phase-opposed dipole oscillation of spin components ↑ and ↓ in the trap. While a z-polarization builds up over time, the spiral spin structure in the x-y plane decreases but stays intact (right panel in Figure 7.5) and the scalar part of the Wigner functions $W_0(x,p)$ remains practically

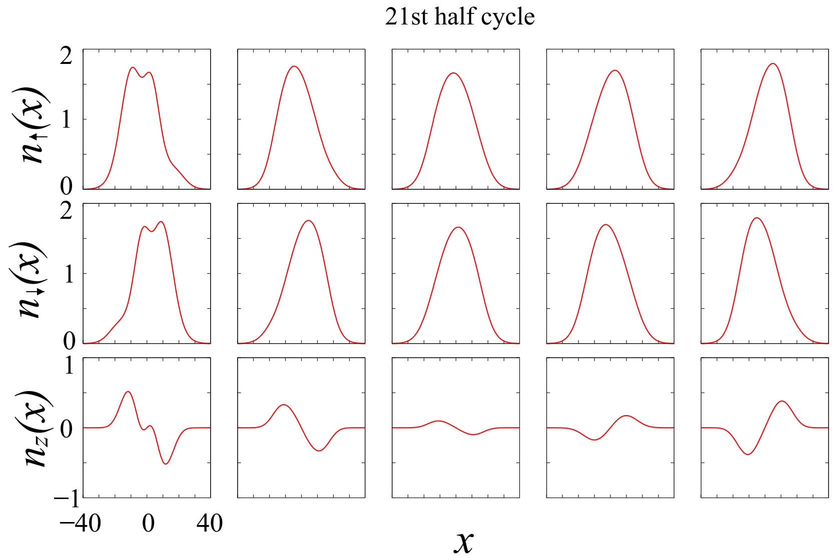

Figure 7.6: Spatial densities $n_\uparrow(x)$ and $n_\downarrow(x)$ as well as z-polarization $n_z(x) = \frac{1}{2}\left[n_\uparrow(x) - n_\downarrow(x)\right]$ at five instants in time during the 21st half cycle for $T = T_\mathrm{F}$ and $\lambda_s/\Delta = 0.2$. Times and parameters correspond to the middle row of panels on the right in Figure 7.5. Spin ↑ and ↓ particles segregate and counter-oscillate in the trap. Figure taken from Ref. [56].

unchanged during the entire time evolution. We can directly control the spin segregation by choosing the number of windings Δ/λ_s of the spin spiral at $t0 =$. With more windings, the segregation builds up slower. The fastest segregation is observed for $\Delta/\lambda_s = 1$, where already after ten half cycles, we find deviations from a linear increase, and a more complex dynamics sets in (Figure 7.5).

The initial buildup of z-polarization and the formation of two domains can be explained intuitively by using the dynamically induced long-range interaction introduced in chapter 6. In dimensionless units (see 6.1) and the the rotating frame (x', p') (6.3), the scalar and vector parts of the mean-field become time-dependent, since it is obtained by projecting onto the x axis, which rotates with respect to the new frame. Applying the rotating-frame formalism derived in section 6.2 to the effective magnetic field (7.12), it assumes the shape

$$\begin{aligned}\vec{B}'_\mathrm{mf}(x', p', t) &\approx \vec{B}^\mathrm{eff}_\mathrm{mf}(x', p', t)\\ &= -\frac{2g}{\pi}\int d\tilde{p}\int d\tilde{x}\frac{1}{\sqrt{\tilde{x}^2+\tilde{p}^2}}\vec{W}'(x'+\tilde{x}, p'+\tilde{p}, t). \end{aligned} \tag{7.21}$$

An equivalent expression can be obtained for the mean-field potential acting on the density,

$$V^\mathrm{eff}_\mathrm{mf}(x', p', t) = \frac{g}{2\pi}\int d\tilde{p}\int d\tilde{x}\frac{1}{\sqrt{\tilde{x}^2+\tilde{p}^2}}W'_0(x'+\tilde{x}, p'+\tilde{p}, t). \tag{7.22}$$

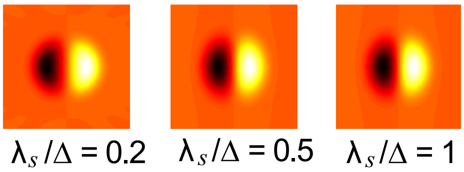

Figure 7.7: Cycle-averaged rate of the creation of z-polarization computed for the initial state $\left[\vec{B}^{\text{eff}}_{\text{mf}}(0) \times \vec{W}'(0)\right]_z$ for $T = T_{\text{F}}$ and different spiral wave lengths λ_s/Δ (arbitrary color scale). This explains the formation of two oppositely polarized domains in W_z, visible in Figure 7.3. Figure taken from Ref. [56].

We simplify the description further and use only the zero-order term in the equation (7.13), we now arrive at the simple effective equations of motion

$$\frac{d}{dt}W'_0(x', p', t) = 0, \tag{7.23}$$

$$\frac{d}{dt}\vec{W}'(x', p', t) = \vec{B}^{\text{eff}}_{\text{mf}}(x', p', t) \times \vec{W}'(x', p', t). \tag{7.24}$$

The second equation describes the time evolution of the polarization field $\vec{W}$ in the x'-p'-plane. At each point the polarization $\vec{W}'$ is rotated by the mean field $\vec{B}^{\text{eff}}_{\text{mf}}$, such that $|\vec{W}'|$ stays constant.

We can now explain the spin segregation by first-order time-dependent perturbation theory and dynamically induced long-range interactions, predicting initially a linear growth of z-polarization,

$$W'_z(x', p', t) \approx t\left[\vec{B}^{\text{eff}}_{\text{mf}}(x', p', 0) \times \vec{W}'(x', p', 0)\right]_z, \tag{7.25}$$

as we can observe in Figure 7.5. Deviations from the linear growth appear as soon as W'_z becomes comparable to $|\vec{W}'|$, as seen in Figure 7.5. In Figure 7.7 we show the rate $\left[\vec{B}^{\text{eff}}_{\text{mf}}(0) \times \vec{W}'(0)\right]_z$ obtained for an intermediate temperature $T = T_{\text{F}}$ and different winding numbers Δ/λ_s. Notably, W'_z always shows the same pattern with two oppositely polarized domains, independent of the initial number of windings. The formation of two domains only can be understood as follows. At any point in phase-space, the vector component of the Wigner function $\vec{W}'(x', p')$ experiences a magnetic field that is mainly determined by the polarization of the nearby phase-space areas. Within the phase-space neighborhood of (x', p'), phase-space areas showing the largest polarization perpendicular to z have the largest effect. Since, for the initial state, $|\vec{W}'| = W'_0/2$ increases toward the origin at a given point (x', p'), the effective magnetic mean field $\vec{B}^{\text{eff}}_{\text{mf}}$ is dominated by the polarization in the direction of the spiral toward the origin. On one side of the spiral this results always in the creation of a positive z polarization; on the other side it results always in the creation of a negative z polarization. This explains the creation of two domains.

The relatively simple example of spin dynamics presented in this section illustrates very well the role of the trap for the dynamics of weakly-interacting systems. Moreover, the phase-space treatment in combination with a semi-classical approximation is shown to provide an adequate and intuitive theoretical framework. We find, that while the anti-commutator of Eq. (3.22) can be neglected for our purposes, the commutator is sufficient to generate dynamical phenomena with long lifetimes and large amplitudes, which we describe in the following chapters for the situation of larger spins and consequently more complex interactions.

Chapter 8

Spin waves in a trapped large-spin Fermi gas

Spin waves are collective excitations of the spin degree of freedom, characterized by currents of spin-components within the bulk system. Transverse spin waves, where the excitation propagates perpendicular to to the oscillation direction, were first observed in experiments on liquid Helium [69, 72] and Hydrogen [71, 73], where exchange interactions were identified as the mechanism behind these effects [70, 74, 75]. These systems can be considered homogeneous systems, while trapped cold-atom systems are inhomogeneous due to the trap. Spin waves are also a prominent feature of ultracold trapped spinor gases, and longitudinal spin waves (the spin wave propagates parallel to the oscillation direction) were observed in a thermal Bose gas of ^{87}Rb [44, 83]. In this chapter, we present a theoretical description of long wavelength excitations observed in a trapped Fermi gas with an effective spin of $F = 3/2$ by the Hamburg group [57]. These results extend beyond preceding work on spin-1 Bosons [40, 41] and show new physical phenomena related to the emergence of higher order (octupole) components. The four-component case is the simplest fermionic system with a larger spin than 1/2. While as of now there still is no true spin-3/2 system experimentally available[1], we consider a four-component subsystem of the spin-9/2 atomic species of ^{40}K. The four spin states are $|F = 9/2, m\rangle$ with $m = \pm 1/2, \pm 3/2$. If the system is prepared in a superposition of these states the remaining states with $|m| > 3/2$ are never sufficiently populated on the time scale we consider in this chapter. This assumption breaks down on the far longer time scales investigated in chapter 10. This chapter is based on Ref. [57].

We investigate the spin waves for small amplitudes, where a linearized description can be applied and dipolar oscillations (sloshing modes) dominate, to the nonlinear regime of large amplitudes, in which also quadrupolar spatial modes (breathing modes) turn out to be relevant. We further show how by engineering the initial state, spin-currents in the trap can be reversed for some spin components relative to others. In order to explain these effects, we expand the Wigner function in terms of tensors in spin space,

---

[1] Proposed atomic species are ^{132}Cs, ^{9}Be, ^{135}Ba, ^{137}Ba and ^{201}Hg [84].

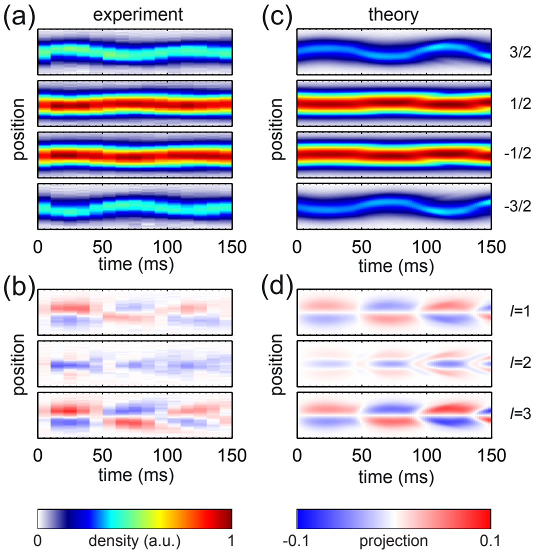

Figure 8.1: (a) In situ time evolution of the spatial distribution $n(z)$ of all four spin components after a 10 ms pulse with a magnetic field gradient of $B = 3.4\,\mathrm{G/m}$. Shown are the column densities at different times after the excitation. (b) Deviation from the initial population of the $m = 0$ component of the vector ($l = 1$), nematic ($l = 2$) and octupole ($l = 3$) components (diagonal tensors T_l^0, see appendix E). The vector and octupole component show spatial dipole oscillations, while the nematic component clearly exhibits quadrupolar spatial oscillations. (c,d) Numerical calculations in the quasi 1D regime for the same parameters of (a,b). Figure taken from Ref. [57].

which allow us to categorize the observed excitations and how they couple. Moreover, we derive a linearized theory with which we calculate the spin wave frequencies in the low-amplitude regime in good agreement with the experimental results.

8.1 Initialization of spin waves

We consider a sample of ^{40}K atoms prepared in the $F = 9/2$ hyperfine manifold. The atoms are cooled down evaporatively to degeneracy in a two-component mixture of the states $|F = 9/2, m = \pm 1/2\rangle$ in an elongated optical dipole trap with frequencies $\omega_{x,y,z} = 2\pi \times (70, 70, 12)\,\mathrm{Hz}$ (see appendix B) and [57, 58, 85] for details on the experiment). From this point, an rf-pulse can be used to create a superposition of the states with $m = \pm 12$ and $m = \pm 3/2$. Mathematically, this amounts to a rotation of the initial 2-component mixture around an axis in the x, y-plane (x without loss of generality) about an angle θ:

$$\hat{W}_{\mathrm{ini}}(\vec{x}, \vec{p}) = f_0(\vec{x}, \vec{p}) \mathrm{e}^{-i\hat{S}_x\theta} \hat{M} \mathrm{e}^{i\hat{S}_x\theta}, \tag{8.1}$$

where $M \propto \mathrm{diag}(0, 1/2, 1/2, 0)$ and f_0 denotes the phase-space distribution of the evaporated two-component mixture, which we approximate as a non-interacting distribution

(2.3). The spin waves are then initialized by applying a magnetic field gradient of variable strength ΔB, described by a magnetic field $\vec{B} = z\Delta B\vec{e}_z$ for a very short time ($\sim 10\,\mathrm{ms}$). This gradient applies a force proportional to m to each spin component (see the anti-commutator in Eq. (3.22)), and leads to a phase spiral for coherent superpositions of different spin-components, as sketched in Figure 8.3. This amounts to a transformation

$$\hat{W}(\vec{x},\vec{p},t=0) = \mathrm{e}^{-ig\mu_B\Delta B\hat{S}_z z}\hat{W}_{\mathrm{ini}}(\vec{x},\vec{p})\mathrm{e}^{ig\mu_B\Delta B\hat{S}_z z}, \tag{8.2}$$

where μ_B denotes the Bohr magneton and g the gyromagnetic ratio. While all particles are still in the same spin superposition state – the atoms are initially still spin-polarized locally – the phase-twist initializes a dynamics in the trapping potential, which allows for interactions in a trapped gas and the potential induces spatial dynamics [56].

The resulting mean-field interaction couples the spin degrees of freedom to the modes of the external trap and lead to the emergence of spin waves.

8.2 Observed dynamics

During the subsequent time evolution, the magnetic field is assumed to be homogenous. This is in contrast to other work on spin-waves, where the gradient was present at all times [21]. A break in spatial symmetry such as the one induced by the gradient is only necessary for the initialization of spin waves, not their propagation [83]. Since experimentally, magnetic field inhomogeneities can be hard to remove, undesired spin-waves may be excited (see chapter 9) and are difficult to suppress.

In Figure 8.1(a), we show a typical picture of a spin wave as observed in the experiment and induced using the prescriptions above. The initial state here is created as described in Eq. (8.1) by an rf-pulse and corresponds to a rotation angle of $\theta = 0.44\,\pi$ with respect to the initial two-component mixture. The applied magnetic field gradient is $3.4\,\mathrm{G/m}$. An interesting feature is the reversed direction of the $\pm 1/2$-components compared to the $\pm 3/2$ components. This effect cannot be explained by an intuitive picture of the gradient "pushing" the spin components with a force proportional to m alone and must be an interaction-induced effect.

In the elongated trap we consider, the gradient is applied along the z-axis and all relevant spin wave dynamics take place in this direction, which is why we can describe the time-evolution in the quasi 1D regime (section 6.5) by integrating out the phase-space coordinates x, y, p_y, p_y. It is also observed, that the total density distribution $N(\vec{x}) = \sum_m \int d^3p W_{mm}(\vec{x},\vec{p})$ does not change at all during the time evolution, such that we can describe the dynamics with a simplified version of Eq. (6.18),

$$\left(\frac{\mathrm{d}}{\mathrm{d}t} - \frac{p}{M}\partial_z + M\omega_z^2 z\partial_p\right)\hat{W}(z,p) = \frac{i}{\hbar}\left[\hat{V}^{\mathrm{mf}}(z,p), \hat{W}(z,p)\right], \tag{8.3}$$

with mean-field potential

$$V_{mn}(x,p) = 2\sum_{kl}\bar{U}_{klnm}\int dp W_{kl}(x,p). \tag{8.4}$$

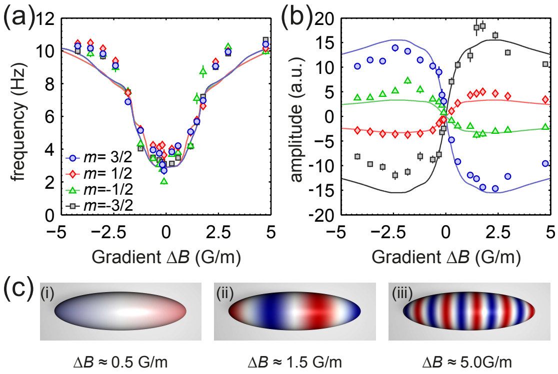

Figure 8.2: (a) Frequency and (b) oscillation amplitude of spin-waves excited with different magnetic field gradients. Negative amplitudes denote an inverted initial direction. Solid lines are numerical data for each component. The trapping frequency is $\omega_z = 12\,\text{Hz}$. All error bars solely correspond to fit errors, representing one standard deviation. The experimental amplitudes, which are taken after time-of-flight and the numerical amplitudes calculated in situ are rescaled onto each other by a global factor. (c) Sketch of the phase windings across the atom cloud for different gradients. Figure taken from Ref. [57].

Here, we have omitted the $\|$-superscripts and defined $p \equiv p_z$. We have introduced one further approximation, namely that we neglect the explicit dependence on z, p of the coupling constants in the quasi-1D regime (see Eq. (6.17)), which we found to be very small for the system geometry considered in this chapter. Hence, here the coupling constants are given by their peak value

$$\bar{U}_{klmn} = \frac{\int dx \int dy [f_0(x,y,z)]^2}{[\int dx \int dy f_0(x,y,z)]^2} \times \bar{U}_{klmn} \approx \frac{\int dx \int dy [f_0(x,y,0)]^2}{[\int dx \int dy f_0(x,y,0)]^2} \times \bar{U}_{klmn}. \tag{8.5}$$

Working in a 4-component subsystem of a spin 9/2 system, one has to keep in mind, that the coupling constants $\bar{U}_{klmn}$ depend on the Clebsch-Gordan coefficients for $F = 9/2$, not for $F = 3/2$. With these considerations, we find Eq. (8.3) to describe spin-waves with good agreement to the experiment. Figure 8.1(c) depicts the results of numerical simulations of Eq. (8.3) with the experimental parameters.

In Figure 8.2, we show the oscillation frequencies (a) and amplitudes (b) of the sloshing oscillations of each spin component, as depicted in Figure 8.1, for different strengths of the magnetic field gradient, while the angle θ corresponding to the rf-pulse before the application of the gradient remains constant at $\theta = 0.44\,\pi$. Also here, results obtained using Equation Eq. (8.3) show good agreement with the experiment. In Figure 8.2(c), we sketch the initial phase spiral along the cigar-shaped Fermi gas. For strong gradients, the number of windings increases and we observe an increase in the oscillation frequency, which seems to approach the trapping frequency. We also notice that for weak gradients, the amplitude depends linearly on the gradient, which indicates the possibility of describing this regime with a linearized theory. We call this the linear regime, where

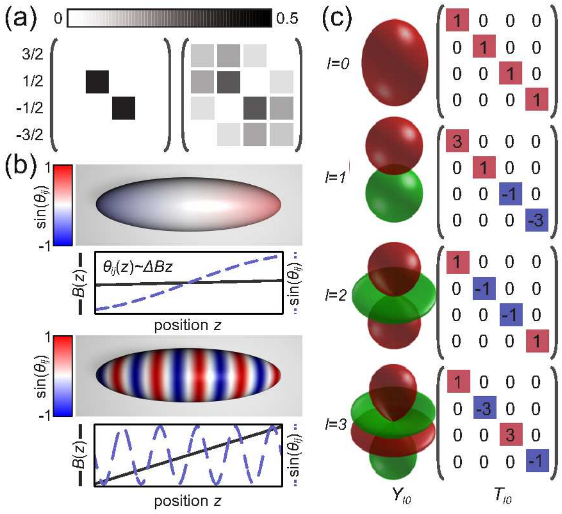

Figure 8.3: (a) Spin components of the Wigner function for an incoherent mixture of $|m = 1/2\rangle$ and $|m = -1/2\rangle$ and the resulting coherent superposition of all four components after a resonant rf-pulse (right). Diagonal elements W_{ii} are real and represent the populations of the four spin components. Off-diagonal elements are complex $W_{ij} = |W_{ij}|e^{i\theta_{ij}}$ and include the phase θ_{ij} between different components. Plotted is only the absolute value $|W_{ij}|$. (b) Sketch of the local phase across the Fermi gas after pulses with magnetic field gradients of different magnitudes. (c) $m = 0$ (diagonal) components of the $l = 0, 1, 2, 3$ tensors T_l^m for spin 3/2 in comparison to the corresponding spherical harmonics Y_l^m. Figure taken from Ref. [57].

the linearized theory we derive later in section 8.4 can be applied. A calculation using the linearized equations with the experimental parameters yields $\omega = 2\pi \times 2.3\,\mathrm{Hz}$ and hence describes well the frequency minimum seen in Figure 8.2(a). For large gradients, the frequency approaches the trapping frequency and again depends only weakly on the excitation amplitude. This can be intuitively understood, if we consider that for such strong gradients, the spin components are so strongly separated, that interactions play only a minor role. In the intermediate regime, the system behaves non-linearly which results in an amplitude-dependent oscillation frequency.

8.3 Tensor expansion of the Wigner function for spin 3/2

In this section, we analyze more closely the spin wave behavior depicted in Figure 8.3, motivated by the finding, that spin components of equal sign, e.g. $m = 1/2, 3/2$ counter-oscillate, despite being subject to a force along the same direction when under the influence of the gradient used to initialize the spin waves.

To gain more insight, we transform the equation of motion by expanding the Wigner function in terms of irreducible spherical tensors T_l^m (spherical harmonics, see Figure 8.3), as we did with the spin 1/2 case in chapter 7, Eq. (7.4), where the tensors are the Pauli matrices. Here, with $F = 3/2$, the expansion reads

$$\hat{W}(\vec{x}, \vec{p}) = \sum_{l=0}^{3} \sum_{m=0}^{2l} W_l^m(\vec{x}, \vec{p}) T_l^m. \tag{8.6}$$

These tensors transform invariantly under rotations and therefore can be ordered by a total spin l and a magnetic quantum number $m = 0, \dots, 2l$. This means, that for a matrix describing a spin-F rotation matrix around Euler angles $\vec{\theta}$, $D^F(\vec{\theta})$, with matrix elements

$$D_{mn}^F(\vec{\theta}) = \langle Fm | \mathrm{e}^{-i\vec{\theta}\cdot\vec{S}} | Fn \rangle, \tag{8.7}$$

the tensors transform as spin-l vectors:

$$D^F(\vec{\theta}) T_l^m (D^F(\vec{\theta}))^\dagger = \sum_n T_l^n D_{nm}^l(\vec{\theta}). \tag{8.8}$$

For the case of spin 1/2, $l = 0, 1$ and the tensors are the Pauli matrices and the Wigner function can be decomposed into a scalar part ($l = 0$) and a vector part ($l = 1$). For spin 3/2, two further components appear, $l = 2, 3$, which we call spin quadrupole (or nematic) and spin octupole components. At the time this project was done, a general prescription on how to obtain suitable tensors for arbitrary spin did not exist (only $F = 1/2$ and 3/2 were studied). In early 2014 however, a general theory of a tensor expansion for arbitrary spins was published [86].

In this thesis, we define a certain set of basis tensors, related, but not completely identical to the choice of Dirac Gamma-matrices and their anticommutators used in earlier work [84, 87–89], where using this expansion an intrinsic SO(5) symmetry was proven for spin-3/2 quantum gases. The scalar ($l = 0$) and vector ($l = 1$) components are simply given by the identity matrix

$$T_0^0 = \frac{1}{2}\mathbb{1} \tag{8.9}$$

and the three spin-matrices in spin-3/2 representation:

$$T_1^0 = \frac{1}{\sqrt{5}} S_x, \tag{8.10a}$$

$$T_1^1 = \frac{1}{\sqrt{5}} S_y, \tag{8.10b}$$

$$T_1^2 = \frac{1}{\sqrt{5}} S_z, \tag{8.10c}$$

where $\vec{S}$ for spin 3/2 are given explicitly in appendix E.

The pre-factors are chosen to ensure normalization, as we will show later. For the spin quadrupole or nematic ($l = 2$) part we choose five traceless symmetric quadratic linear combinations of S_i,

$$T_2^0 = \frac{1}{2}\left(S_z^2 - \frac{5}{4}\mathbb{1}\right) \tag{8.11a}$$

$$T_2^1 = \frac{1}{2\sqrt{3}}\left(S_x^2 - S_y^2\right) \tag{8.11b}$$

$$T_2^2 = \frac{1}{2\sqrt{3}}\left(S_xS_y + S_yS_x\right) \tag{8.11c}$$

$$T_2^3 = \frac{1}{2\sqrt{3}}\left(S_zS_x + S_xS_z\right) \tag{8.11d}$$

$$T_2^4 = \frac{1}{2\sqrt{3}}\left(S_yS_z + S_zS_y\right). \tag{8.11e}$$

Apart from normalization, these matrices correspond to the Dirac Gamma matrices. The remaining seven matrices for $l = 3$ are chosen to be

$$T_3^0 = \frac{\sqrt{5}}{3}\left(S_z^3 - \frac{41}{20}S_z\right) \tag{8.12a}$$

$$T_3^1 = \frac{\sqrt{5}}{3}\left(S_x^3 - \frac{41}{20}S_x\right) \tag{8.12b}$$

$$T_3^2 = \frac{\sqrt{5}}{3}\left(S_y^3 - \frac{41}{20}S_y\right) \tag{8.12c}$$

$$T_3^3 = \frac{1}{2\sqrt{3}}\left\{S_x, S_y^2 - S_z^2\right\} \tag{8.12d}$$

$$T_3^4 = \frac{1}{2\sqrt{3}}\left\{S_y, S_z^2 - S_x^2\right\} \tag{8.12e}$$

$$T_3^5 = \frac{1}{2\sqrt{3}}\left\{S_z, S_x^2 - S_y^2\right\} \tag{8.12f}$$

$$T_3^6 = \frac{1}{\sqrt{3}}\left(S_xS_yS_z + S_zS_yS_x\right). \tag{8.12g}$$

As defined above, the T_l^m obey the transformation properties (8.8). Roughly speaking, the value of l corresponds to the powers of spin matrices $\vec{S}$, out of which the T_l^m are composed. The nematic tensors T_2^m are symmetric linear combinations of products of two spin matrices, the octupole tensors are antisymmetric combinations of products of three spin matrices. In Figure 8.3 (c), the diagonal matrices T_l^0 are depicted, along with the corresponding spherical harmonic Y_{l0} to illustrate their rotational properties. We provide a full list of all T_l^m in appendix E, where one an check that apart from T_0^0, all other tensors are traceless $\mathrm{Tr}(T_l^m) = 0$.

The entire set of 16 hermitian matrices T_l^m forms a complete, orthonormal set with respect to the scalar product defined by the trace:

$$\mathrm{Tr}\left(T_l^m T_{l'}^{m'}\right) = \delta_{ll'}\delta_{mm'}. \tag{8.13}$$

As all 16 T_l^m are Hermitian, any 4×4 Hermitian matrix $\hat{M}$, such as the Wigner function, can then be expanded in terms of these tensors

$$\hat{M} = \sum_{l=0}^{3} \sum_{m=0}^{2l} M_l^m(z,p) T_l^m, \tag{8.14}$$

with coefficients obtained using the formula

$$M_l^m = \mathrm{Tr}\left(T_l^m \hat{M}\right). \tag{8.15}$$

This expansion can be applied to the mean-field potential V^{mf} as well. If we look at the coupling constants (2.16), they are sums of terms of the form $A_{ik}A_{jl}$, where $A_{ik} = \langle ik|SM\rangle$. In general, we can transform such an expression according to

$$A_{ik}A_{jl} = \sum_{\alpha} C_\alpha B_{ij}^\alpha B_{kl}^\alpha, \tag{8.16}$$

where the matrices $\hat{B}^\alpha$ form a complete basis. This is called a *Fierz transformation*. If the target basis $\{B^\alpha\}$ is composed of irreducible representations of a group, all matrices belonging to one representation receive the same coefficient. In our case, the tensors T_l^m belong to the scalar, vector, etc. representation of SU(2), so we can apply this theory here and obtain

$$U_{ijkl} = \sum_{l=0}^{3} \sum_{m=0}^{2l} \alpha_l^m (T_l^m)_{ij} (T_l^m)_{kl}. \tag{8.17}$$

In a true spin 3/2 system with only two scattering lengths a_0 and a_2, the coefficients are given by

$$\alpha_0^0 = \frac{1}{2}\left(g_0 + 5g_2\right), \quad \alpha_1^m = \frac{1}{2}\left(-g_0 - g_2\right), \quad \alpha_2^m = \frac{1}{2}\left(g_0 - 3g_2\right), \quad \alpha_3^m = \frac{1}{2}\left(-g_0 - g_2\right). \tag{8.18}$$

so there is no dependence on m and α_1 and α_3 are identical, which is a result of an intrinsic SO(5) symmetry in such a system (see e.g. [87]). In our case, where we treat a spin-9/2 system “truncated” to spin 3/2, this degeneracy is lifted. For simplicity, in the following, we will treat the system as a spin-3/2 and omit the m-dependence of the coefficients $\alpha_l^m \to \alpha_l$. For more details on the difference between a truncated and a true spin-3/2 system, we refer to appendix D.

Using the identity (8.17), the mean-field potential (8.4) assumes the shape

$$\hat{V}^{\mathrm{mf}}(z) = \sum_{l=0}^{3} \sum_{m=0}^{2l} V_l^m(z) T_l^m \tag{8.19}$$

in the new basis. We find each l-component to be proportional to the respective l-component of the Wigner function

$$V_l^m(z) = \mathrm{Tr}\left(\hat{V}^{\mathrm{mf}}(z) T_l^m\right) = \alpha_l \int d^3p W_l^m(\vec{x}, \vec{p}). \tag{8.20}$$

Roughly speaking, the coupling constants U_{klmn} have been diagonalized by transforming into the basis of irreducible spherical tensors, which results in a simpler equation.

Substituting equations (8.6) and (8.19) into the mean-field equation of motion (8.4), it is transformed into

$$\begin{aligned}\left(\frac{\mathrm{d}}{\mathrm{d}t} - \frac{p}{M}\partial_z + M\omega^2 z\partial_p\right) &\sum_{l=0}^{3}\sum_{m=0}^{2l} W_l^m(z,p)T_l^m \\ &= \frac{i}{\hbar}\sum_{l',l''}\sum_{m',m''}\alpha_{l''}\int dq W_{l'}^{m'}(z,p)W_{l''}^{m''}(z,q)\left[T_{l'}^{m'},T_{l''}^{m''}\right],\end{aligned} \tag{8.21}$$

from which we obtain the equation for W_l^m by multiplying with $T_{l'''}^{m'''}$ and taking the trace, to obtain

$$\left(\frac{\mathrm{d}}{\mathrm{d}t} - \frac{p}{M}\partial_z + M\omega^2 z\partial_p\right) W_l^m(z,p) = \frac{i}{\hbar}\sum_{l',l''}\sum_{m',m''}\alpha_{l''}\int dq W_{l'}^{m'}(z,p)W_{l''}^{m''}(z,q)\Lambda_{l'l''l}^{m'm''m}. \tag{8.22}$$

The coefficients on the right hand side are derived from the commutation relations of the T_l^m and are defined as

$$\Lambda_{l'l''l}^{m'm''m} = \mathrm{Tr}\left(T_l^m\left[T_{l'}^{m'},T_{l''}^{m''}\right]\right), \tag{8.23}$$

or in other words as the l,m-components of the commutators of two tensors T_l^m. While it would be too cumbersome to write down a complete list of all $\Lambda_{l'l''l}^{m'm''m}$, we note that for many combinations of (l,l',l'',m,m',m''), they vanish. In fact, only for certain combinations, they are non-zero, given in the following table:

l	(l', l'')
1	(1,1), (2,2), (3,3)
2	(1,2), (2,1), (2,3), (3,2)
3	(2,2), (3,3), (1,3), (3,1).

(8.24)

In combination with Eq. (8.22), this allows us to know which excitations to expect depending on the type of initial state we prepare the system in. For instance, the time evolution of the dipolar components $l = 1$ depends only on excitations, where a component with angular momentum l' couples to one with the same value of $l'' = l'$. We visualize this by writing down the equations (8.22) in a short symbolic notation, suppressing the m-indices:

$$\begin{aligned}\partial_t W_0 &\cong \partial_0 W_0,\\ \partial_t W_1 &\cong \partial_0 W_1 + \frac{i}{\hbar}\left([W_1,V_1]+[W_2,V_2]+[W_3,V_3]\right),\\ \partial_t W_2 &\cong \partial_0 W_2 + \frac{i}{\hbar}\left([W_2,V_1+V_3]+[W_1+W_3,V_2]\right),\\ \partial_t W_3 &\cong \partial_0 W_3 + \frac{i}{\hbar}\left([W_3,V_1]+[W_1+W_3,V_3]+[W_2,V_2]\right).\end{aligned} \tag{8.25}$$

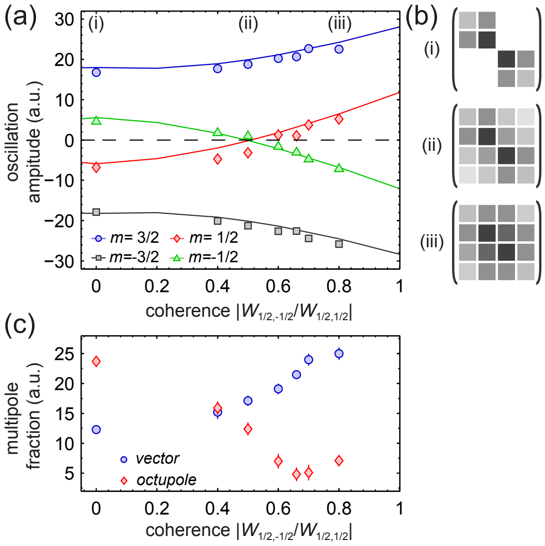

Figure 8.4: (a) Spatial oscillation amplitude of the spin-wave excitations for different initial coherences but equal populations of the four components at $B = 3.6, \mathrm{G/m}$: Solid lines show the initial spin-wave amplitude extracted from numerical calculations. (b) Exemplary spin Wigner functions for different initial coherences. (c) Amplitude of the dipole and octupole tensor components W_1^0 and W_3^0. (d) Vector and octupole tensors T_1^0 and T_3^0 evaluated in (c). All error bars solely correspond to fit errors, representing one standard deviation. The experimental amplitudes, which are taken after time of flight and the numerical amplitudes calculated in situ are rescaled onto each other by a global factor. Figure taken from Ref. [57].

We now go back to the initial spin configuration, we considered so far (8.1), which we obtained by applying a rotation to a two-component mixture, described by a matrix $W_{mn}(z, p) \propto \mathrm{diag}(0, 1, 1, 0)$. This matrix is a purely nematic spin state, since it can be expanded according to

$$\mathrm{diag}(0, 1, 1, 0) = \frac{1}{2}\mathbb{1} + \frac{1}{2}\mathrm{diag}(-1, 1, 1, -1) = T_0^0 - T_2^0. \tag{8.26}$$

Due to the rotational properties of the tensors T_l^m, the rotation induced by the rf-pulse does not change this fact. Hence, according to Eq. (8.25), excitations on top of this nematic initial state should be dipolar and octupolar, but not nematic themselves. And indeed, as shown in Figure (8.1) (b), where the spatial densities of the diagonal components W_l^0 are plotted, we see that dipolar and octupolar excitations dominate. The motion of the $l = 2$ component is only a weak perturbation and has the shape of a quadrupolar spatial mode (breathing mode), which we can attribute to imperfect state preparation and the influence of the higher order anticommutator term in the equation of motion. We have included this term in the simulations used to calculate the data for the plots in Figure (8.1) (d), which show very good agreement to the experimental results.

In order to further understand the interplay between the tensor degrees of freedom, we can also use a different procedure to create initial spin configurations that are not purely nematic. Using a different technique (see [57] for details), not only the full Wigner-function can be rotated at a certain angle, but also such rotations can be applied to two-component subsets of the Wigner-function. Mathematically, an exemplary operation of this kind would be

$$W_{\mathrm{ini}}(z,p) = f_0(z,p)\left(\mathrm{e}^{-i\vec{\theta}\cdot\vec{\sigma}} \otimes \mathbb{1}_{2\times 2}\right) \hat{M} \left(\mathrm{e}^{i\vec{\theta}\cdot\vec{\sigma}} \otimes \mathbb{1}_{2\times 2}\right), \tag{8.27}$$

where σ denote Pauli matrices and $\mathbb{1}_{2\times 2}$ the 2× identity matrix. This operation only performs a rotation around Euler angles $\vec{\theta}$ within the components $m = 1/2, 3/2$, while leaving the other components unchanged.

With this technique, it is possible to create initial states $\hat{W}_{\mathrm{ini}}(z,p)$ with non-zero dipolar and octupolar components from an initial two-component mixture of $m = \pm 1/2$. A good measure to quantify these new initial states is the ratio of coherences to the corresponding diagonal matrix element $c = |W_{1/2,-1/2}/W_{1/2,1/2}|$, which for the nematic states considered earlier is always zero. In Figure 8.4, we tune c and plot the resulting amplitude of the four spin components. At $c \approx 0.5$, the inner components $|\pm 1/2\rangle$ change direction. An investigation in terms of the tensor expansion of section 8.3 yields that for small values of c, the spin wave is dominated by the octupole component, while at large c, the dipole component takes over. The second increase of the octupole amplitude at large c is due to higher order spatial excitations, possible in the nonlinear regime, where the measurements were performed. At $c = 0.5$, the vector and octupole component contributions cancel, and the $|\pm 1/2\rangle$ components are quasi stationary.

8.4 Linearized equations

In this section, we derive a linearized theory to analytically obtain the minimum of the spin-wave frequencies shown in Figure 8.2. We apply a moment method technique, to a linearized kinetic equation, in which we categorize excitation on top of the initial state in terms of their dependence on powers of x, p, similar to the tensor expansion in section 8.1, where we expand the excitations in powers of $\vec{S}$. It captures the long-wavelength collective behavior of the trapped gas. This method is valid for small amplitudes spin waves in the linear regime, i.e. for small gradients ΔB. For this purpose, we consider small changes with respect to a stationary state $W^0_{mn}(z,p)$, such that $W^m_l(z,p,t) \approx W^m_{0l}(z,p) + \delta W^m_l(z,p,t)$. Thus we investigate the spin waves for short times and small amplitudes. The mean-field, as a function of the Wigner function itself likewise separates into a stationary part and a small perturbation: $(V^{\mathrm{mf}})^m_l(z,t) = V^m_{0l}(z) + \delta V^m_l(z,t)$. We substitute both expressions into the simplified equation (8.22), keep only the linear terms, and obtain

$$\left(\frac{\mathrm{d}}{\mathrm{d}t} - \frac{p}{M}\partial_z + M\omega_z^2 z\partial_p\right)\delta W_l^m(z,p) = \\ \frac{i}{\hbar}\sum_{l',l''}\sum_{m',m''} \Lambda_{l'l''l}^{m'm''m}\left(\delta W_{l'}^{m'}(z,p)V_{0l''}^{m''}(z) + W_{0l'}^{m'}(z,p)\delta V_{l''}^{m''}(z)\right), \tag{8.28}$$

the linearized kinetic equation.

For a good description of the observed spin-wave effects, we need to choose the stationary part accordingly. We use the spin state of the system after an rf-pulse is applied to the initial $m = \pm 1/2$ mixture, but before the magnetic field gradient is used to excite the spin waves. Assuming an infinitely fast rf-pulse, we approximate $W_{0l}^m(z,p)$ with a product of the equilibrium phase space distribution $f_0(z,p)$ and the spin-state created by the rf-pulse:

$$W_{0l}^m(z,p) = f_0(z,p)M_l^m. \tag{8.29}$$

In our weakly-interacting regime, $f_0(z,p)$ can be approximated by the non-interacting equilibrium distribution (3.21), such that in our quasi-1D description,

$$f_0(z,p) = \frac{1}{(2\pi\hbar)^3}\int dx \int dy \int dp_x \int dp_y \left(\mathrm{e}^{\frac{1}{k_\mathrm{B}T}\left[\frac{p^2}{2M}+\frac{1}{2}M\left(\omega_x^2x^2+\omega_y^2y^2+\omega^2z^2\right)-\mu\right]} + 1\right)^{-1}. \tag{8.30}$$

This function is rotationally invariant in phase-space, using units rescaled with the trap frequency ω. Hence $\left(\frac{p}{M}\partial_z - M\omega^2 z\partial_p\right) f_0(z,p) = 0$. The stationary part of the mean-field now reads

$$V_{0l}^m(z) = \tilde{\alpha}_l M_l^m n_0(z), \tag{8.31}$$

where $n_0(z) = \int dp f_0(z,p)$.

We are interested in the long-wavelength excitations, which in a harmonic trap are given by the sloshing (dipolar), breathing (quadrupolar) and higher modes. In order to study these modes, we expand the phase-space degrees of freedom in *moments* of the position and momentum operators. Let $\chi(z,p)$ be a polynomial in z and p, then we define the stationary and dynamic moments

$$\langle\chi\rangle_0 = \int dz \int dp\chi(z,p)f_0(z,p), \tag{8.32}$$

$$\langle\chi\rangle_l^m(t) = \int dz \int dp\chi(z,p)\delta W_l^m(z,p,t). \tag{8.33}$$

If $\chi = p^l, x^l$ we call $\langle p^n\rangle_l^m$ the n-th moment of p, the same holds for powers of z.

The time dependent part of the linearized equation (8.28) is expanded into moments of x and p:

$$\delta W_l^m(z,p) = f_0(z,p)\left(A_l^m(t) + zB_l^m(t) + pC_l^m(t)\right), \tag{8.34}$$

$$\delta V_l^m(z) = \tilde{\alpha}_l n_0(z)\left(A_l^m(t) + zB_l^m(t)\right). \tag{8.35}$$

a_0	a_2	a_4	a_6	a_8
119.92	147.83	161.11	166.00	168.53

Table 8.1: Partial scattering lengths for ^{40}K in units of Bohr radii. Source: Ref. [90] (Supplemental material).

The expansion goes up to first order in (z, p), such that we can calculate the frequencies of the dipole modes without complications. Taking the appropriate moments of the equations (8.34,8.35), we obtain the relationship between the coefficients A, B, C and the moments in z, p:

$$A_l^m(t) = \frac{1}{N}\langle \mathbb{1}\rangle_l^m(t), \tag{8.36a}$$

$$B_l^m(t) = \frac{\langle z\rangle_l^m(t)}{\langle z^2\rangle_0}, \tag{8.36b}$$

$$C_l^m(t) = \frac{\langle p\rangle_l^m(t)}{\langle p^2\rangle_0}. \tag{8.36c}$$

We note here, that the inclusion of higher moments can lead to more complicated relationships than (8.36) and the matrix connecting coefficients and moments may no longer be diagonal [44].

Next, we substitute (8.34) and (8.35) into (8.28) and obtain

$$\begin{aligned}\left(\frac{\mathrm{d}}{\mathrm{d}t} - \frac{p}{M}\partial_z + M\omega_z^2 z\partial_p\right) f_0(z,p)\left[A_l^m(t) + zB_l^m(t) + pC_l^m(t)\right] = \\ \frac{i}{\hbar} f_0(z,p) n_0(z) \sum_{l',l''}\sum_{m',m''} \tilde{\alpha}_{l''}\Lambda_{l'l''l}^{m'm''m}\left(\left[A_{l'}^{m'} + zB_{l'}^{m'} + pC_{l'}^{m'}\right] M_{0l''}^{m''}\right. \\ \left. + M_{0l'}^{m'}\left[A_{l''}^{m''} + zB_{l''}^{m''}\right]\right).\end{aligned} \tag{8.37}$$

We integrate this equation over z, p to obtain the following set of equations for A, B, C:

$$\dot{A}_l^m(t) = I_0 \frac{1}{i\hbar}\sum_{l',l''}\sum_{m',m''} \tilde{\alpha}_{l''}\Lambda_{l'l''l}^{m'm''m}\left[A_{l'}^{m'}(t) M_{0l''}^{m''} + M_{0l'}^{m'} A_{l''}^{m''}(t)\right], \tag{8.38a}$$

$$\dot{B}_l^m(t) - M\omega_z^2 C_l^m(t) = I_1 \frac{1}{i\hbar}\sum_{l',l''}\sum_{m',m''} \tilde{\alpha}_{l''}\Lambda_{l'l''l}^{m'm''m}\left[B_{l'}^{m'}(t) M_{0l''}^{m''} + M_{0l'}^{m'} B_{l''}^{m''}(t)\right], \tag{8.38b}$$

$$\dot{C}_l^m(t) + \frac{1}{M} B_l^m(t) = I_2 \frac{1}{i\hbar}\sum_{l',l''}\sum_{m',m''} \tilde{\alpha}_{l''}\Lambda_{l'l''l}^{m'm''m} C_{l'}^{m'}(t) M_{0l''}^{m''}, \tag{8.38c}$$

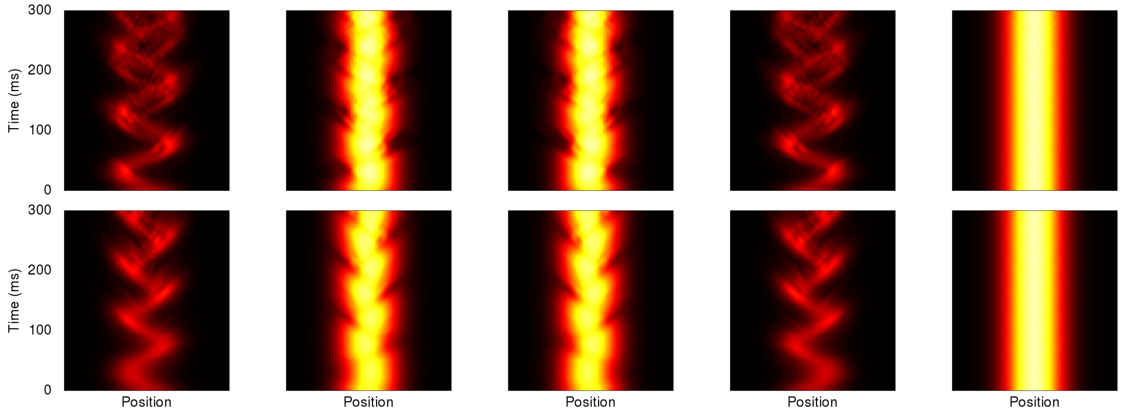

Figure 8.5: Comparison of spin waves for the real scattering lengths of ^{40}K (top) and the SU(4) case (bottom). The dominating frequency of the dipole oscillations of all four spin components is identical, but in the SU(N) case there are less spatial modulations and dephasing in each individual component. Hence to obtain the main frequency, we describe the system with the simpler SU(4) interactions. In both cases, the total density (rightmost column) is stationary, supporting our simplification of Eq. (8.31) by omitting the gradient term.

where

$$I_0 = \frac{1}{N}\int dz[n_0(z)]^2, \tag{8.39a}$$

$$I_1 = \frac{1}{\langle z^2\rangle_0}\int dzz^2[n_0(z)]^2, \tag{8.39b}$$

$$I_2 = \frac{1}{\langle p^2\rangle_0}\int dz\int dpp^2 f_0(z,p)n_0(z). \tag{8.39c}$$

The first equation (8.38a) is decoupled from the others and does not lead to spatial dynamics (it describes spin dynamics such as that laid out in chapter 9), so we ignore it here. Equations (8.38b) and (8.38c) describe dipole oscillations of all spin components of the Wigner function and the frequencies can be obtained by a Fourier transform and solving the eigenvalue equations.

A justification for further simplification can be seen in Figure 8.5, where we depict spin waves for two systems, that are identical except for their scattering lengths. The results were obtained by integrating the quasi-1D equation (8.3), including the anticommutator term, which nevertheless has negligible effect here. In Figure 8.5(a), we use the scattering lengths for ^{40}K (see Table 8.4), while in 8.5(b) we use a single scattering length, $a_0 = a_2 = a_4 = a_6 = a_8 \equiv a_0$. If there is only a single scattering length present, the coupling constants (8.19) simplify to $\alpha_0 = 3g/2$ and $\alpha_1 = \alpha_2 = \alpha_3 = -g$ (see appendix D for more details). The interaction Hamiltonian then becomes SU(N)-invariant [32–34]. In this case, spin-changing collisions are absent. We observe that for the study of spin waves, spin-changing collisions are not very relevant and we can describe them sufficiently well with a simplified SU(4) model. A further justification lies in the fact, that in ^{40}K, the differences of the values for all a_S are very small. If we apply the SU(N)-interactions to equations (8.38), the first equation (8.38a) becomes zero on the right hand side. The remaining two equations reduce to

$$\dot{B}_l^m(t) = M\omega_z^2 C_l^m(t) \tag{8.40a}$$

$$\dot{C}_l^m(t) + \frac{1}{M}B_l^m(t) = I_2\frac{g}{i\hbar}\sum_{l',l''}\sum_{m',m''}\Lambda_{l'l''l}^{m'm''m}C_{l'}^{m'}(t)M_{0l''}^{m''}. \tag{8.40b}$$

In order to decouple these equations, we take the time derivative of (8.40a) and substitute it into (8.40b):

$$\ddot{C}_l^m(t) + \omega_z^2 C_l^m(t) = I_2\frac{g}{i\hbar}\sum_{l',l''}\sum_{m',m''}\Lambda_{l'l''l}^{m'm''m}\dot{C}_{l'}^{m'}(t)M_{0l''}^{m''}. \tag{8.41}$$

After a Fourier transform with respect to time, $\dot{C} \to -i\omega C$, we obtain the eigenvalue equation

$$\left(\omega^2 - \omega_z^2\right)C_l^m(t) = 2\omega\omega_{\mathrm{mf}}\sum_{l',l''}\sum_{m',m''}\Lambda_{l'l''l}^{m'm''m}\dot{C}_{l'}^{m'}(t)M_{0l''}^{m''}. \tag{8.42}$$

Here, we have introduced the mean-field frequency $\omega_{\mathrm{mf}} = gI_2/2\hbar$. As a result of our simplification of the interactions, we obtain only a single mean-field frequency, instead of a matrix of slightly different frequencies, which simplifies our analysis here. The solutions of Eq. (8.42) lead to the frequencies of the dipole modes. There are trivial solutions $\omega = \pm\omega_z$ that describe the Kohn-mode [91], harmonic oscillations of the entire atomic cloud in the trap, for instance if the atoms are somehow prepared off-center. The other solutions apply to the propagation of dipolar oscillations and are given as

$$\omega = -\omega_{\mathrm{mf}} \pm \sqrt{\omega_{\mathrm{mf}}^2 - \omega_z^2}. \tag{8.43}$$

8.5 Conclusions

In this chapter, we have described excitations of a four-component spinor Fermi gas in a harmonic trap. We have performed an expansion of both spin and spatial modes, which leads to a transparent theory for long-wavelength spin waves. Using this expansion, we showed why the most visible spin waves in the experiments are dipole oscillations of the spin dipole and octupole components, namely because only those modes appear in the leading order term of the semiclassical equation of motion. We achieved very good agreement with the experimental results for short time-scales, where damping is not an issue yet, using the collisionless mean-field theory.

Chapter 9

Coherent spin-changing dynamics

With spin-changing dynamics, we denote the time evolution of the macroscopic population of individual spin components in a large system. This requires spins $F > 1/2$, because s-wave collisions, which change the spin of a pair of atoms, conserve the total spin, hence more than two spin components are required. In the case of bosons, spinor dynamics has been studied in spinor Bose-Einstein condensates, where several spin states are trapped in an optical dipole trap [92–94]. Spinor BEC with spins $F = 1$ [22, 37, 40, 95, 96], $F = 2$ [16, 23, 38, 97] and $F = 3$ [17, 18, 45, 98] have been created and larger spins up to $F = 11$ [99] may become available, for recent reviews see [4, 36]. In the case of Fermions, large spin gases have been experimentally available for a long time – ^{40}K was even used in the first demonstration of a degenerate Fermi gas [8] – and degenerate Fermi gases with spins up to $F = 21/2$ are possible [100], but only recently interest in spinor dynamics [90, 101] and other large spin effects [86, 102–104] has arisen. This chapter is based on Ref. [58].

As we pointed out earlier, the mechanism behind spinor dynamics are spin-changing collisions. In the regime of s-wave scattering, as well as due to the Pauli principle, not all scattering processes $\{m_1, m_2\} \to \{m_3, m_4\}$ are allowed. S-wave scattering conserves total spin $m_1 + m_2 = m_3 + m_4$, and the Pauli principle prohibits binary collisions, where the incoming or outgoing atoms are in the same spin state. The exception happens, when noticeable anisotropic long-range dipole-dipole interactions are present in the system, such that a transfer of total spin into orbital angular momentum can occur [22, 105–107]. There are also predictions for Dysprosium atoms, where even contact interactions may be sufficiently anisotropic to break the conservation of total spin in a collision [108]. However, for the system of ^{40}K considered in this chapter, such anisotropic effects do not play a role. Atoms with large spins in an external magnetic field experience not only a linear Zeeman splitting, which due to the conservation of total spin does not play a role for spin-changing collisions. Quadratic or higher orders play a role. As a possible consequence, a very large quadratic Zeeman splitting can suppress spin-changing collisions.

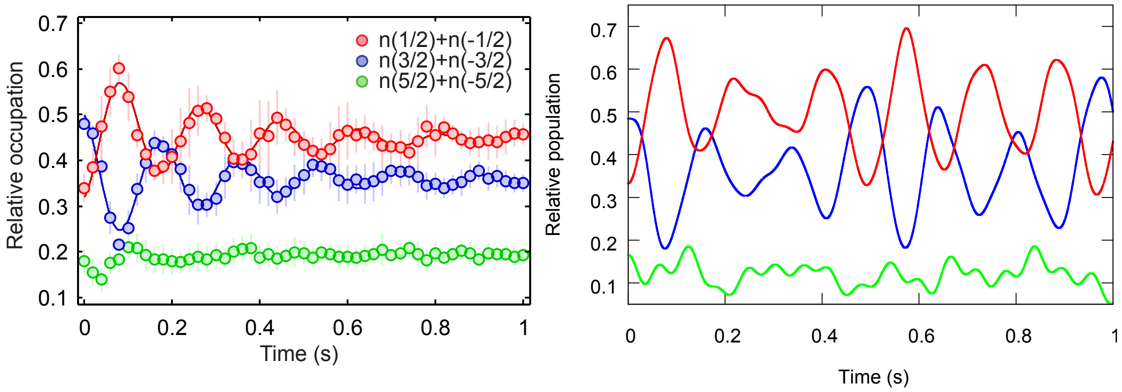

Figure 9.1: Collective spinor dynamics in a Fermi gas. The system is prepared in a coherent spin configuration with large populations in the states $|\pm 1/2\rangle$ and $|\pm 3/2\rangle$, corresponding to a rotation angle of $\theta = 0.44$. We plot the relative populations of the sum of two components $|\pm m\rangle$, which remain equal during the time evolution due to total spin conservation. Left: Experimental plot. Points denote measured values, lines are fits to the data. Right: Theoretical plot obtained using the collisionless Boltzmann equation in the quasi-1D regime (6.18). In both cases, the frequencies are $\vec{\omega} = 2\pi \times (32, 33, 137)\,\mathrm{Hz}$ and other parameters $B = 0.12\,\mathrm{G}$, $n_p = 5.9 \times 10^{12}\,\mathrm{cm}^{-3}$ and $T = 0.13\,T_{\mathrm{F}}$. Left figure taken from Ref. [58].

9.1 Giant spin oscillations

The results presented in this chapter were again obtained in collaboration with the experimental group of Klaus Sengstock in Hamburg, using the same experimental setup as in the preceding chapter 8, but with different parameters and different initial states. Now we use all the 10 spin states of the ^{40}K atoms in its $F = 9/2$ ground state hyperfine manifold. Otherwise, the initial state preparation and theoretical description remains similar to the spin waves in chapter 8. The equation of motion is given by

$$\frac{\mathrm{d}}{\mathrm{d}t}\hat{W}(\vec{x},\vec{p}) = \nabla_0 \hat{W}(\vec{x},\vec{p}) + \frac{i}{\hbar}\left[\hat{V}^{\mathrm{mf}}(\vec{x}), \hat{W}(\vec{x},\vec{p})\right] - \frac{1}{2}\left\{\nabla_r \hat{V}(\vec{x}), \nabla_p \hat{W}(\vec{x},\vec{p})\right\} + \hat{I}_{\mathrm{coll}}(\vec{x},\vec{p}), \tag{9.1}$$

where now the matrices are of size 10 × 10.

Using an initial state created via an rf-pulse (8.1), with a homogenous external magnetic field, the dynamics of the spin components is found to be oscillatory, as depicted in Figure 9.1. We find large-amplitude long-lived spin-changing oscillations of the relative populations of the $m = \pm 12$ and $m = \pm 3/2$ components, while the other spin components hardly participate. This is because of the initial state, in which only coherences between these components are sufficiently populated. A comparison with numerical simulations of the collisionless ($\hat{I}_{\mathrm{coll}}(\vec{x},\vec{p}) = 0$) Boltzmann equation (9.1) in the quasi-1D regime reproduces the measured behavior, except for damping. In the simulations, we also observe oscillations in the population of the $m = \pm 5/2$ component, with a small

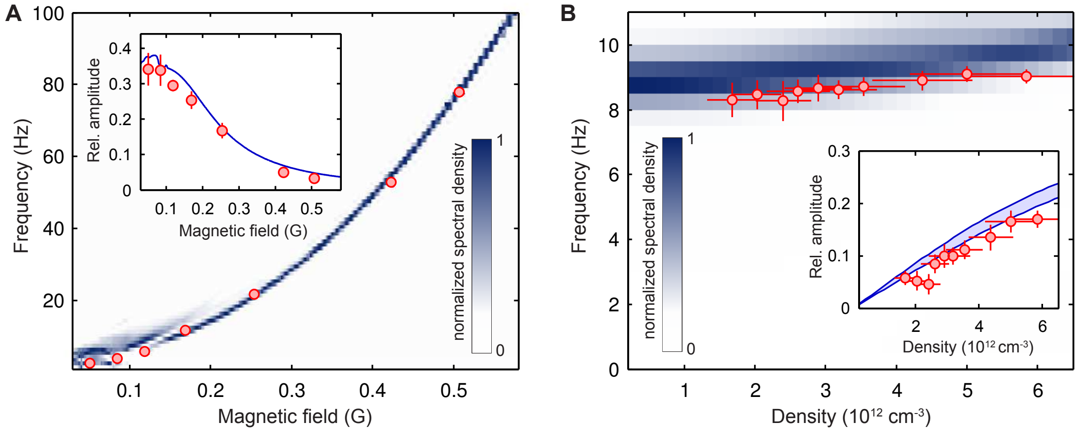

Figure 9.2: Frequency (main plots) and amplitude (inset) of coherent spin oscillations as functions of magnetic field (A) and density (B). The initial state is the same as in Figure 9.1. Red points denote experimental data obtained from fits (see [58, 85] for details), blue data are calculations using a collisionless single-mode equation. The shaded area in (B) denotes fluctuations in particle number. Parameters are $n_p = 1.0 \times 10^{13}\,\mathrm{cm}^{-3}$, $T = 0.22\,T_\mathrm{F}$ in (A); $B = 0.17\,\mathrm{G}$ and $T = 0.18\,T_\mathrm{F}$ in (B). Taken from Ref. [58].

amplitude, likely too small to be observed experimentally. A striking feature of these giant spin oscillations is that the atoms, despite being fermions, behave collectively, and seem to change their internal state all at once. In the numerical data, we see no spatial dynamics such as dephasing, which is why we obtain good agreement even if the trapping frequencies do not justify a quasi-1D treatment. In the next section, we explain this effect theoretically.

9.2 Collective behavior of a Fermi sea

The spin oscillations depicted in Figure 9.1 are governed by microscopic s-wave scattering events. We can expect two energy scales to be involved in such a spin-changing collision, the differential interaction energy and quadratic Zeeman energy. Hence, we have measured the dependence of the oscillation frequency and amplitude on the applied external magnetic field as well as the density at constant T/T_F. The results are plotted in Figure 9.2. We find, that the oscillation frequency is determined by the quadratic Zeeman energy for large magnetic fields, which becomes evident from the quadratic dependence in Figure 9.2A. For weak magnetic field, we find superposition of oscillation with different frequencies, which indicates that in this regime, spin-changing collisions determine the frequencies. These collisions have different scattering amplitudes for each spin configuration, thus we observe more than a single frequency.

The behavior of the amplitude in 9.2A (inset) can also be understood intuitively. At large magnetic fields, initial and final spin configurations during a spin-changing collision

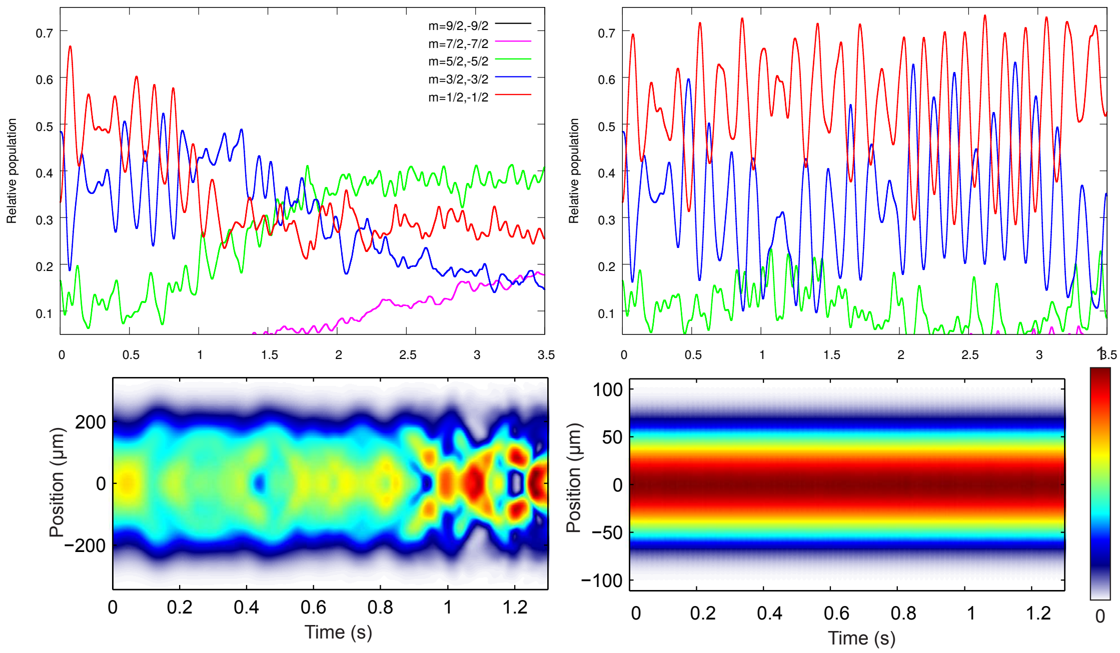

Figure 9.3: Comparison of numerical simulations of the collisionless equation 6.18 in the quasi-1D regime for the two different trap geometries depicted in Figure 6.2. However, here, in addition, the spin component populations are depicted in the top row. Left: Trapping frequencies are $\vec{\omega} = 2\pi \times (5, 200, 200)$ Hz, hence the axial frequency is far too low to induce a time-averaged long-range interaction, leading to strong dephasing. This plot shows how spatial dephasing (bottom row depicts the normalized spatial distribution of the $m = 1/2$-component, see also Figure 6.2), leads to a reduction of oscillations, even without taking into account incoherent collisions. Right: Trapping frequencies are $\vec{\omega} = 2\pi \times (33, 34, 137)$ Hz and lead to long-lived undamped collective behavior, without visible spatial structure. Note that in both cases, the average frequency $\bar{\omega} = (\omega_x \omega_y \omega_z)^{1/3}$ is approximately equal. Bottom row taken from Ref. [58].

are energetically separated further, such that this difference cannot be overcome by the interaction energy. The density dependence in 9.2B is taken at a rather low magnetic field of $B = 0.17$ G in the interaction dominated regime, where we expect frequency and amplitude to depend on density, which determines the overall collision rate. As can be expected, we observe an increase of oscillation frequency and amplitude with density.

Now, we focus on the most striking effect observed and depicted in Figures 9.1 and 9.2, the apparently collective dynamics of the spins in the system. In a Fermi gas, each particle occupies a different single-particle mode, apart from spin degeneracy, which even for $F = 9/2$ is very small compared to typical particle numbers of the order of 10^5. Hence, we would expect spatial dephasing in the system, where the spin oscillations would have different frequencies at different positions in the trap, and as a consequence no clear oscillations as shown in Figure 9.1 with a well-defined global frequency as shown

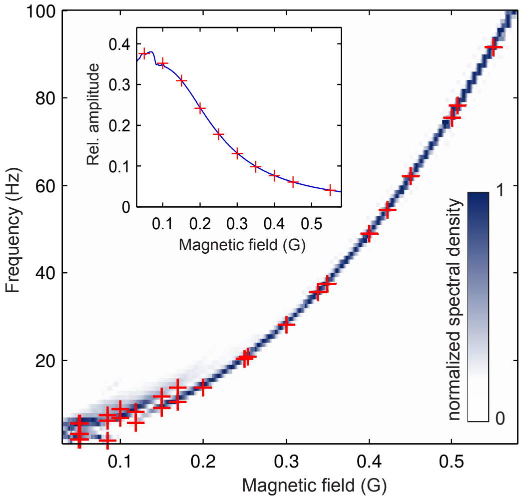

Figure 9.4: Simulation of spin oscillation frequency (main graph) and amplitude (inset) as a function of the applied magnetic field. The experimental parameters from the measurements in Figure 9.2 A are used. Solid lines in insets correspond to the amplitude and the shading in main graph to a Fourier spectrum, both deduced from calculations within a single-mode approximation. Crosses are the extracted amplitudes and frequencies from calculations using the mean-field equation in the quasi 1D-regime, with full momentum and spatial resolution in one dimension. The very good agreement justifies the use of the simple single-mode description in this parameter regime. Taken from Ref. [58].

in Figure 9.2 would be visible.

As the key mechanism for the observed collective spinor dynamics, we identify the trap. As laid out in chapter 6, a sufficiently high trapping frequency leads to the preservation of the symmetry of the original phase-space distribution. A lower trap frequency leads to spatial dephasing, where the frequency of spin oscillations depends on the position in the trap and the oscillations of the total populations of each component wash out in time due to this. In Figure 9.3 we compare theoretical results using two different geometries. In the left frame, the axial trapping frequency is 5 Hz and hence on the order of magnitude as the spin-oscillations, in the right frame we use the experimental trapping frequencies. In both cases, the Fermi energy $\propto (\omega_x \omega_y \omega_z)^{1/3}$ is identical, as are particle number, T/T_F and magnetic field. We see that in the highly elongated case, the oscillation amplitude of the relative spin populations decreases over time, and spin states with higher m become populated, while for the case with the experimental parameters, the oscillations between the components $m = \pm 1/2$ and $m = \pm 3/2$ continue with approximately fixed amplitude and frequency. The reason for this qualitatively different behavior is depicted in the bottom row of Figure 9.3. There, we plot the spatial density of the $m = 1/2$-component, normalized by its population. In the trap with low axial frequency, we observe strong spatial dephasing, while for the experimental geometry, no

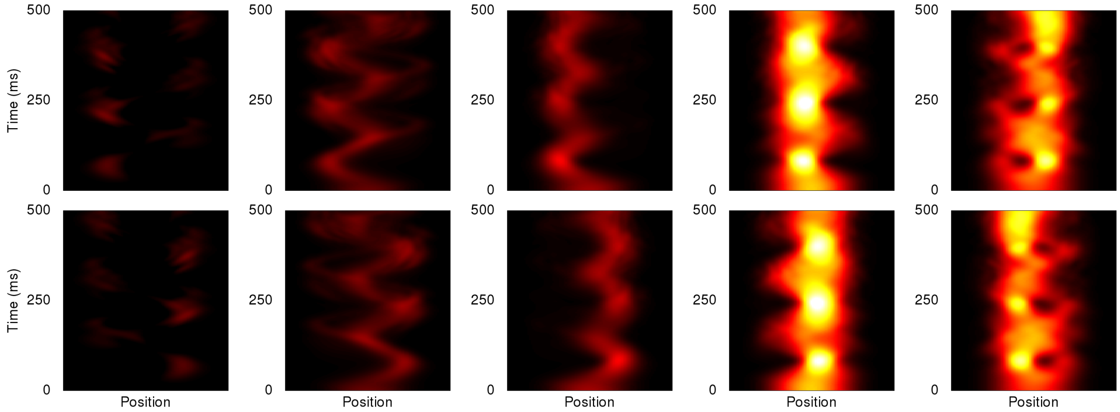

Figure 9.5: Spin waves in a full spin 9/2 system, using the initial spin state with a rotation angle of $\theta = 0.44\,\pi$ and a small magnetic field gradient. Unlike in chapter 8, here the gradient is permanently present, to simulate a residual inhomogeneity present in the experiment if not actively compensated for. The spatial separation of the spin components, especially pronounced for $m = \pm 1/2, \pm 3/2$, leads to strongly suppressed spin-changing dynamics. Top row, from left to right: Spatial densities of $m = 9/2, 7/2, 5/2, 3/2, 1/2$, bottom row: negative m showing the mirrored motion.

dephasing occurs at all.

The complete absence of spatial structures induced by strong harmonic confinement in all spatial directions for in all spin component justifies the description of spinor dynamics in the experimental setup with the single-mode approximation derived in section 6.6.1. This description leaves the initial phase-space density intact and only describes the time-evolution of the collective spins of the system (see e.g. Eq. (6.23)). To further support the validity of the single-mode picture for the trapping frequencies used in the experiment, in Figure 9.4 we compare numerical results using a quasi-1D collisionless Boltzmann equation (9.1) with single-mode results, showing very good agreement.

9.3 Damping of coherent spin oscillations

Now that we have established, that spatial dephasing is prevented by dynamically-induced long-range interactions, the damping of oscillations observed in Figure 9.1 must have a different origin. First, we rule out another possible mechanism, namely the possibility of having excited spin-waves (as studied in chapter 8) in the system. The initial spin configuration used to induce the coherent spin oscillation is created in the same way as for the spin-waves, by applying an rf-pulse to a balanced mixture of atoms in spin states $m = \pm 1/2$ (see Eq. (8.1)). This means that in the experiment, even the presence of a small gradient will initiate spin-wave excitations characterized by periodic spatial separation of the spin components. This separation would decrease the collision rate.

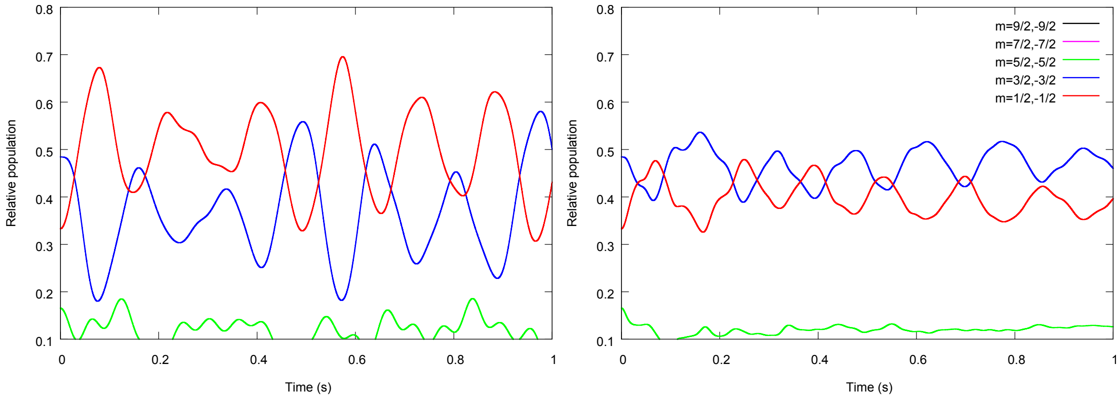

Figure 9.6: Oscillations of spin populations in a homogeneous magnetic field (left, identical to Figure 9.1,right) and in the presence of a gradient (right). Results are obtained using the collisionless equation in the quasi-1D regime. The parameters are identical to Figure 9.1 except for the gradient of $\partial_x B(x) = 0.6\,\mathrm{G/m}$. Compared to Figure 9.1, oscillation amplitudes are greatly reduced. This shows how even a small gradient can strongly suppress spin oscillations to the point, where they are hardly visible in an experiment.

Residual gradients are a common feature in experimental setups. In Figure 9.5, we plot the time evolution of the spatial density profile of all ten spin states, using the same parameters as in Figure 9.1 B, but in the presence of a weak gradient of $\Delta B = 0.6\,\mathrm{G/m}$. We observe strong separation, especially between the spin components of $m = 1/2$ and $m = -1/2$ (rightmost column).

With the spin components separating during the time-evolution, we expect a reduction of spin-changing interactions, and indeed spin oscillations can become strongly suppressed even by small magnetic field gradients. In Figure 9.6, we show the time-evolution of the population of the spin-components for two almost identical systems, which differ only in the gradient. The gradient is zero in Figure 9.6 (left) and $0.6\,\mathrm{G/m}$ in 9.6 (right), which corresponds to the density profiles plotted in Figure 9.5. We realize that even such a small gradient leads to a noticeable reduction of amplitude, which outlines the importance of reducing or actively canceling inhomogeneities in the magnetic fields in experiments in order to observe visible spinor dynamics with a large amplitude. However, we also observe that the gradient does not lead to a damping of the spin oscillation, hence there must be another mechanism not described on a mean-field level.

This means, the damping of oscillations in Figure 9.1 is not described by the collisionless version of Eq. (9.1) and must be a consequence of lateral scattering. As we established in chapter 4, spin-conserving lateral collisions are much stronger than spin-changing ones and are expected to be the relevant process here. In order to estimate the damping rates observed in the experiment, we now take into account the collision integral (4.55) describing the effect of lateral collisions and derive a simplified collision term in the relaxation approximation. Similar to chapter 8, we use linearized theory but this time also apply it to the collision integral

$$\begin{aligned}I^{\mathrm{coll}}_{mn}(\vec{r},\vec{p}) = &-\frac{M}{4\pi\hbar^4}\int d^3q\Bigg\{\sum_{abc}\Big(\sqrt{q^2+\Delta_{mcab}}\tilde{U}_{macb}W_{an}(\vec{r},\vec{p})W_{bc}(\vec{r},\vec{p}-\vec{q})\\ &+\sqrt{q^2+\Delta_{abnc}}\tilde{U}_{anbc}W_{ma}(\vec{r},\vec{p})W_{cb}(\vec{r},\vec{p}-\vec{q})\Big)\\ &-\frac{1}{2\pi}\int d\Omega\sum_{abcdl}\hbar\bar{k}U_{malb}U_{ncld}W_{ac}(\vec{r},\vec{p}-\tfrac{1}{2}(\vec{q}-\vec{p}')W_{bd}(\vec{r},\vec{p}-\tfrac{1}{2}(\vec{q}+\vec{p}')\Bigg\}.\end{aligned} \tag{9.2}$$

Again, we separate the Wigner function into a stationary part and a time-dependent perturbation $W_{mn}(\vec{r},\vec{p},t) = W^0_{mn}(\vec{r},\vec{p}) + \delta W_{mn}(\vec{r},\vec{p},t)$. The stationary part is given by a product of phase-space distribution and spin density matrix $W^0_{mn}(\vec{r},\vec{p}) = M_{mn}f_0(\vec{r},\vec{p})$, with

$$f_0(\vec{r},\vec{p}) = \frac{1}{(2\pi\hbar)^3}\left\{\exp\left(\frac{1}{k_{\mathrm{B}}T_0}\left[\frac{\vec{p}^2}{2M}+\frac{1}{2}M\left(\omega_x^2x^2+\omega_y^2y^2+\omega_z^2z^2\right)-\mu_0\right]\right)+1\right\}^{-1}. \tag{9.3}$$

Since the rf-pulse used to generate M_{mn} is applied to a two-component mixture, the Wigner function is normalized, and temperature T_0 and chemical potential μ_0 chosen, such that $\int d^3r\int d^3pf_0(\vec{r},\vec{p}) = N/2$. For short times, we can linearize the collision integral around $W^0_{mn}(\vec{r},\vec{p})$, but for longer times on which damping appears, this may not be optimal. The experimental results 9.1 show that the system reaches a pre-equilibrium state, where coherent oscillations have stopped, but the populations of the other spin states such as $m = \pm 7/2, \pm 9/2$ are still negligible. We assume the phase-space distribution of this state to be approximated by a second distribution

$$f_1(\vec{r},\vec{p}) = \frac{1}{(2\pi\hbar)^3}\left\{\exp\left(\frac{1}{k_{\mathrm{B}}T_1}\left[\frac{\vec{p}^2}{2M}+\frac{1}{2}M\left(\omega_x^2x^2+\omega_y^2y^2+\omega_z^2z^2\right)-\mu_1\right]\right)+1\right\}^{-1}, \tag{9.4}$$

where T_1 and μ_1 are chosen such that total single-particle energy and particle number are conserved with respect to f_0. Because this distribution has 4 spin states populated it is normalized differently: $\int d^3r\int d^3pf_1(\vec{r},\vec{p}) = N/4$ and we assume an approximately balanced population of all four non-zero components. We model the system's evolution from f_0 to f_1 with the simple Ansatz

$$\delta W_{mn}(\vec{r},\vec{p},t) = \left(f_0(\vec{r},\vec{p}) - f_1(\vec{r},\vec{p})\right)A_{mn}(t). \tag{9.5}$$

We introduce

$$A_{mn}(t) = \frac{4}{N}\int d^3r\int d^3p\delta W_{mn}(\vec{r},\vec{p},t), \tag{9.6}$$

which corresponds to the lowest term in the moment expansion (8.36) in chapter 8. The linearized equation can now be written in matrix notation as

$$\frac{d}{dt}A - \frac{1}{i\hbar}\Omega_{\mathrm{MF}}(A) = -\Gamma A + I\left[W_0\right], \tag{9.7}$$

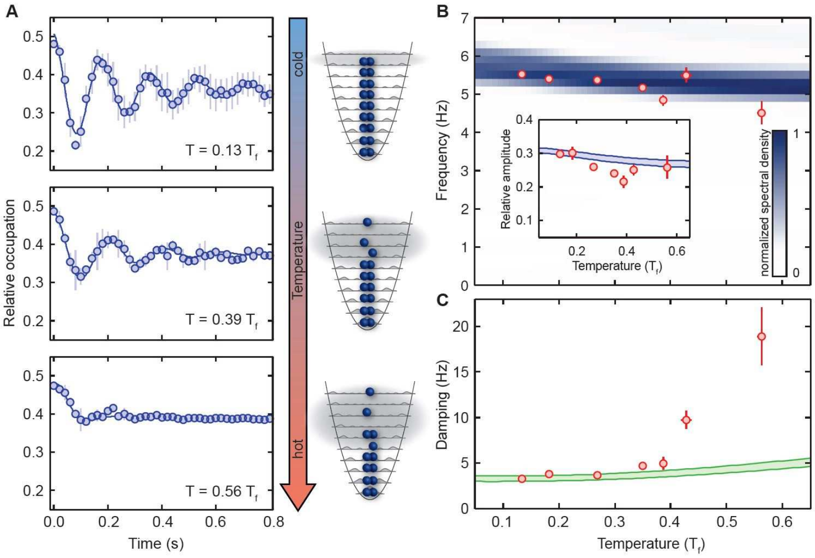

Figure 9.7: The influence of temperature on collective spinor dynamics. **A** Time evolution of the occupations of spin states $|m = \pm 3/2\rangle$ for three different temperatures (experimental data and fitted curves). **B** Frequency (main graph) and amplitude (inset) for different temperatures. **C** Damping rate versus temperature. The initial state was prepared as for the measurements in Figure 9.1 and the experimental parameters are $B = 0.12\,\mathrm{G}$ and $n_p = 5.2 \times 10^{12}\,\mathrm{cm}^{-3}$. Experimental data (red points) is deduced from fits. Amplitude and frequency calculations in **B** are performed within a single-mode approximation, damping calculations in **C** within a relaxation approximation. Taken from Ref. [58].

where Ω_{MF} denotes a tensor of mean-field frequencies similar to the one appearing in Eq. (8.43). In $I[W_0]$ only the stationary parts of the collision integral appear, it is quadratic in W_0 and does not depend on δW. The tensor Γ contains the damping rates for each element of the Wigner function. With respect to spin it has the form $\Gamma_{klmn} = \gamma_{klmn} I(k_{\mathrm{B}}T)$, where

$$I(k_{\mathrm{B}}T) = \int d^3r \int d^3p \int d^3q |\vec{p} + \vec{q}| f_0(\vec{r}, \vec{p}) \left(f_0(\vec{r}, \vec{q}) - f_1(\vec{r}, \vec{q})\right) \tag{9.8}$$

is a spin-independent function of temperature.

Results in Figure 9.7 C show the comparison of the relevant matrix element of Γ for the damping of the spin component $W_{3/2,3/2}$. It captures the general trend with respect to temperature, but the increase for large temperatures is lower than the experimental value. The reason for this lies in our strongly simplified model derived above, but also in the fact that our Boltzmann equation is not a true quantum Boltzmann equation. It is derived from two-body collisions (see section 4.1), but does not take Pauli blocking into account, which arises from three-body effects. Here, where spin-conserving collisions are involved,

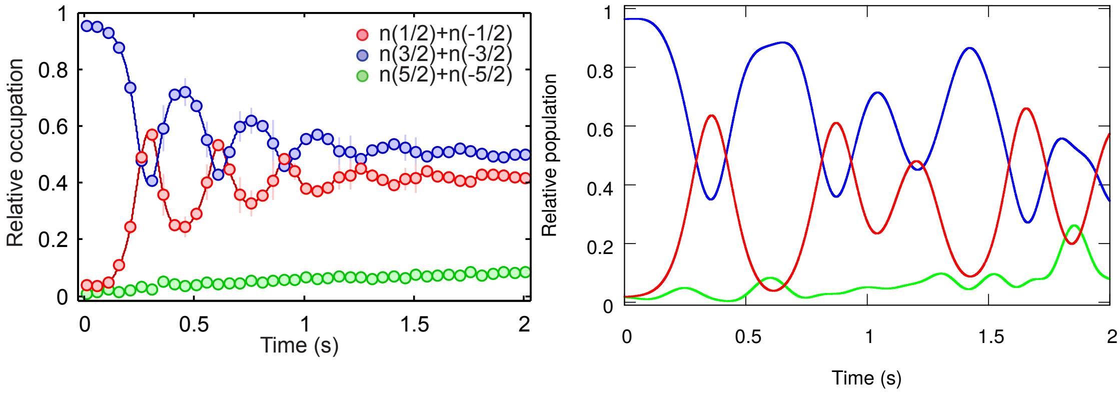

Figure 9.8: Time evolution of a magnetically excited spin configuration with only very small initial coherences, given by fluctuations. The particles quickly populate the other spin states and coherences, leading to oscillations in the long run. Left: Experimental results showing the relative populations of the spin states. Solid lines are a guide to the eye only. Right: Numerical results, obtained using a collisionless Boltzmann equation in the quasi 1D regime 6.18. The simulations show the same drop of the system from its initial configuration, but the absence of collisional decoherence lead to a almost complete return to the initial state. Left figure taken from Ref. [58].

our theory does not take into account that at low temperatures, many possible single-particle states, into which the two colliding atoms could scatter, are already occupied by a third atom. As a consequence, we cannot expect to fully reproduce the temperature behavior of the damping in Figure 9.7 C. The dependence of the oscillation frequency on temperature, depicted in Figure 9.7 B however, is reproduced, as the oscillations are driven by forward scattering, where the colliding atoms stay in the same single-particle mode, such that in this case, three-body Pauli blocking is irrelevant.

9.4 Stability properties

The oscillations described in the preceding sections depend on the preparation of coherences in the initial density matrix using rf-pulses. However, it not not necessary to prepare these coherences, the system can also produce them on its own. This happens when it is prepared in a two-state mixture $|\pm m\rangle$, but where $m \geq 1/2$, such that the particles are not in the lowest energy state with respect to the quadratic Zeeman splitting (see appendix A for details). Then such a spin configuration is unstable with respect to the mean-field dynamics and any small perturbation or seed in the coherences leads to a massive redistribution into the lower-lying Zeeman states, while quadratic Zeeman energy is converted into interaction energy through mean-field interactions. This behavior is shown in Figure 9.8, where in the experiment (left), a large-scale redistribution is observed, which then leads to coherent, damped spin oscillations on longer time-scales. Theoretical results (right) obtained using a collisionless quasi-1D equation reproduce this

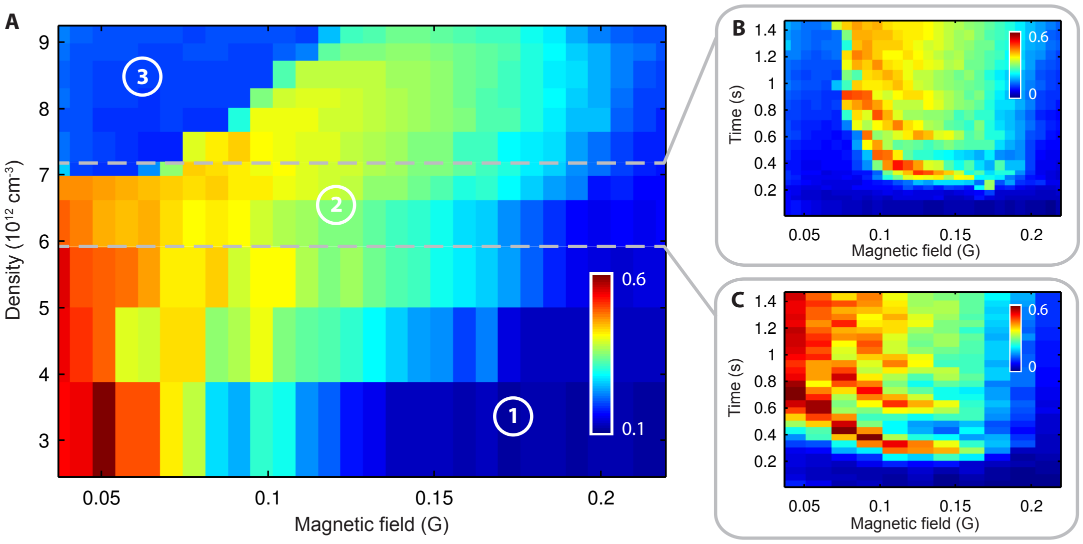

Figure 9.9: Experimental results for the stability of a Fermi gas prepared in an magnetically excited state. **A** Plotted is the occupation of the lowest quadratic Zeeman states $|m = \pm 1/2\rangle$ after 2 s, as a function of magnetic field and initial density. We find three distinct regions: A Zeeman-protected regime ①, where interactions are too weak to overcome the level spacing induced by the magnetic field. The unstable regime ②, where dynamics such as in Figure 9.8 occur appears for higher densities, but at very high densities and weak magnetic fields, the is another stable region ③, where the system does not evolve. **B**| and **C** show the time evolution of the $|m = \pm 1/2\rangle$-components for variable magnetic fields in regions ② and ③, with peak densities $n_p = 7.2 \times 10^{12}\,\mathrm{cm}^{-3}$ **B** and $n_p = 5.9 \times 10^{12}\,\mathrm{cm}^{-3}$ **C**. Taken from Ref. [58].

effect. Without the damping induced by lateral collisions included in the equation, the system almost returns to its initial spin configuration.

The entire effect can be understood as similar to an unstable inverted pendulum (see also [39]), which starts in a state with maximal potential energy (here the quadratic Zeeman energy), but minimal kinetic energy (here interaction energy). Here, in a Fermi gas, the interaction energy is initially low, because in a two-component mixture, each atom can only interact with $N/2$ other atoms, a number, which increases, the more other spin states are populated.

In Figure 9.9, we map the dependence of this instability on magnetic field and density, showing regions, where the dynamics is very fast, but also, where the instability does not occur. In the region (2), the quadratic Zeeman and interaction energy are resonant and hence spinor dynamics occur. This is the region corresponding to Figure 9.8. For larger magnetic fields (1), the quadratic Zeeman levels are too strongly detuned, such that collisions cannot overcome the energy differences and spinor dynamics becomes fully suppressed. The more surprising feature is a region of stability (3) for low magnetic fields at large densities, where one would intuitively expect very rapid mean-field dynamics, since the mean-field term in the kinetic equation (9.1) is quadratic in density. But we observe a complete absence of dynamics, the system is stabilized in its initial excited state. This unexpected region of stability can be reproduced using the single-mode description with a simplified collision term in relaxation approximation,

$$I_{mn}^{\mathrm{coll}}(\vec{r},\vec{p}) \approx -\sum_{kl} \Gamma_{klmn} W_{kl}(\vec{r},\vec{p}). \tag{9.9}$$

This is plotted in Figure 9.10. For good agreement, we have to scale the damping rate calculated in section 9.3 with a factor of 2.25. This is necessary because of the many approximations made in this description, e.g. the damping rates are obtained from a linearized theory. However, the same linearized approach with respect to the mean-field level does not reproduce the instability, only spin oscillations such as in section 9.2. This proves that the instabilities are a non-linear effect unlike the oscillations and we cannot simply calculate something as a “growth rate” for the coherences in this case. Nevertheless, the effect of incoherent collisions is that off-diagonal elements of the Wigner function go to zero, and in the stability region for large densities in Figure 9.10 the decoherence caused by an increased rate of such collisions is stronger than the growth of coherences due to the spin instability. In other words, with each collision, the single-particle density matrix is projected back onto its initial state at an increased rate, similar to a measurement-induced quantum Zeno effect. It is worth noting that this stability effect through decoherence is induced by the dominating spin-conserving collisions, which depend on averages of scattering lengths. The effect of incoherent spin-changing collisions is weaker, hence incoherent population transfer appears on a slower time-scale and shall be treated in the next chapter of this thesis.

9.5 Conclusions

In this chapter, we have have identified the mechanism for an entire Fermi sea undergoing collective long-lived large-amplitude spin oscillations. The oscillations are a mean-field effect driven by spin-changing forward scattering and the differential quadratic Zeeman energy. We have discussed possible mechanisms for dephasing, which would suppress such large-amplitude oscillations, such as the presence of gradients. We found that the harmonic trap induces dynamically induced long-range interactions, which suppress spatial dephasing and lead to the observed collective spin oscillations, which can then be described with a simple single-mode approach with good agreement to the experiment. In addition, we investigated instabilities, another mean-field effect that occurs when the system is prepared in an excited quadratic Zeeman state. We found, that the rate of incoherent collisions can outgrow the instability and stabilize the system in an unexpected regime of high densities.

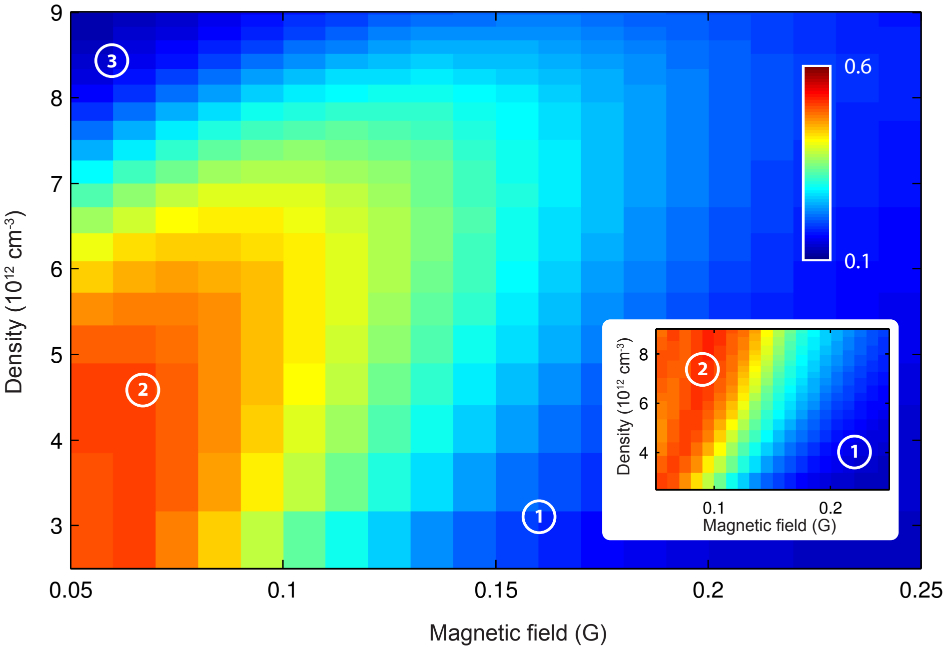

Figure 9.10: Theoretical calculations for the stability of the Fermi gas as plotted in Figure 9.1. Shown is the calculated spin occupation of $|m = \pm 1/2$ after a time evolution of 3.5 s, depending on magnetic field and density. The parameters are the same as in Figure 9.1 and use as initial spin configuration a state prepared in an incoherent mixture of $|m = \pm 3/2$ with a small rf-pulse corresponding to $\theta = 0.1$ to account for fluctuations, that trigger the instability. The calculations are performed in single-mode approximation, with the damping rate taken from Eq. (9.8) and scaled with a factor of 2.25. We can reproduce all the regions of the experimental stability diagram 9.9: a Zeeman-protected regime ①, a spin-oscillation regime ② and the collisionally-stabilized regime ③. In the inset, we plot a stability diagram with a weak density-independent damping rate of 2 Hz. Here, only regimes ① and ② are present. Taken from Ref. [58].

Chapter 10

Relaxation of a large-spin Fermi gas

In this chapter, we study the long-time relaxation dynamics of the trapped fermionic gas of ^{40}K atoms. This chapter is based on Ref. [59]. Different from the preceding chapters 8 and 9, we start from an initial two-state mixture of $m = \pm 12$ without coherences, such that mean-field dynamics and instabilities discussed in section 9.4 are suppressed and investigate its relaxation dynamics caused by the incoherent spin-changing collisions, leading to a redistribution of the atoms among all available spin states on a long time scale, as sketched in Figure 10.1. We again perform a comparison of numerical results from simulations of a Boltzmann equation and experimental data and find good agreement. We study the dependence of the relaxation process on density and magnetic field, where a higher density enhances the spin relaxation in 3D and strong magnetic fields suppress it. This suppression can be used to control the loss of particles from the initially populated two-component subsystem into the remaining empty states and allows us to interpret this subsystem as an open system coupled to the environment given by the initially empty spin states. We observe that the relaxation within such a subset of spin states, driven by incoherent spin-conserving collisions, happens on a much faster time scale than the redistribution among the spin components due to spin-changing collisions, and thus we encounter a situation similar to prethermalization [52], where first a prethermal state is reached, approximately conserving the initial occupations of the single spin states, before the redistribution among all spin states due to a slight symmetry breaking sets in. The resulting separation of time scales also allows us to monitor the increase of (effective) temperature within the subsystem of the initially populated spin states, as it is caused by dissipation into empty spin states.

10.1 Relaxation processes in a large-spin system

A long-time relaxation of the spin 9/2 Fermi gas of ^{40}K is already slightly visible in the experimental measurements depicted in Figure 9.1, and becomes apparent when the experiment is run for longer time scales. This is depicted in Figure 10.2, where we show that long after the coherent oscillations have ceased because of damping, the system continues evolving towards a state with approximately equal population in all

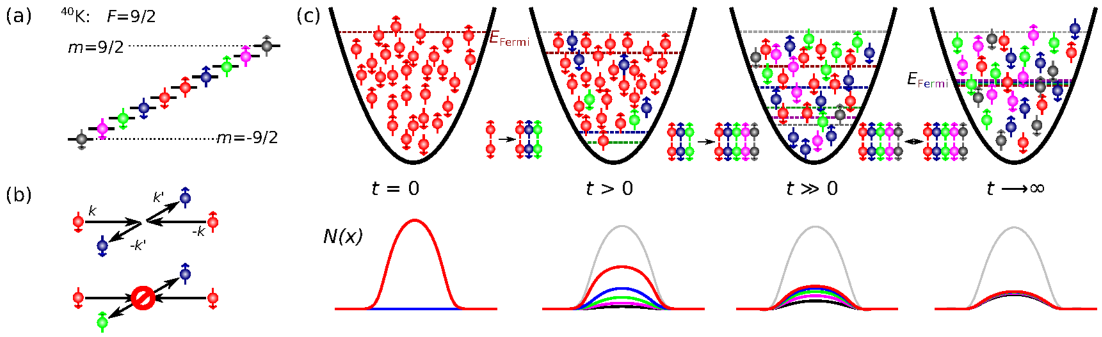

Figure 10.1: Schematic description of the relaxation process in a large-spin Fermi gas involving spin and spatial degrees of freedom. (a) The ten spin states of ^{40}K. (b) A typical spin-changing collision in the center-of-mass frame and another collision forbidden by the Pauli exclusion principle. (c) Top: Initially all atoms are prepared in a binary spin mixture $m = \pm 1/2$. Spin-changing collisions distribute atoms among all other spin states until an approximately balanced population is reached. The Fermi energies for each two-component subsystem is lower than the initial Fermi energy. Bottom: Time evolution of the spatial density for each spin component. Taken from Ref. [59].

spin states. This adds a third effect on another time-scale to the picture. In Figure 10.3 we show a typical time evolution from the same coherent superposition of spin states as in Figure 10.2, but in a 1D setup, where the results are obtained via numerical simulations of the 1D Boltzmann equation

$$
\begin{aligned}
\frac{d}{dt} W_{mn}(x,p) = &-\frac{p}{M}\cdot\partial_x W_{mn}(x,p) - \frac{i}{\hbar}\sum_l \left[V_{nl}(x)W_{ml}(x,p) - W_{lm}(x,p)V_{ln}(x)\right] \\
&+ \frac{1}{2}\sum_l \left\{\partial_x V_{nl}(x)\partial_p W_{ml}(x,p) + \partial_p W_{lm}(x,p)\partial_x V_{ln}(x)\right\} \\
&- \frac{M}{\hbar^2}\sum_{abl}\Bigg[\int_{q^2>\epsilon_m} dq \frac{\tilde{U}_{malb}}{\sqrt{q^2+\Delta_{mlab}}} W_{an}(x,p)W_{bl}(x,p-q) \\
&+ \int_{q^2>\epsilon_n} dq \frac{\tilde{U}_{nalb}}{\sqrt{q^2+\Delta_{nlab}}} W_{ma}(x,p)W_{lb}(x,p-q) \\
&- \sum_{abcdl}\int_{q^2>\epsilon'} dq \frac{U_{malb}U_{ncld}}{\hbar\bar{k}} W_{ac}(x,p-\tfrac{1}{2}(q-\hbar\bar{k}))W_{bd}(x,p-\tfrac{1}{2}(q+\hbar\bar{k}))\Bigg].
\end{aligned}
\tag{10.1}
$$

With this, we can identify the scattering processes responsible for all effects visible in Figures 10.2 and 10.3: (i) The coherent spin-changing oscillations with a periodicity on the order of hundred milliseconds, which we described in chapter 9 as a mean-field effect. Their origin is coherent spin-changing forward scattering and they can be described by the mean-field description of chapter 3. In the Boltzmann equation (10.1), the corresponding

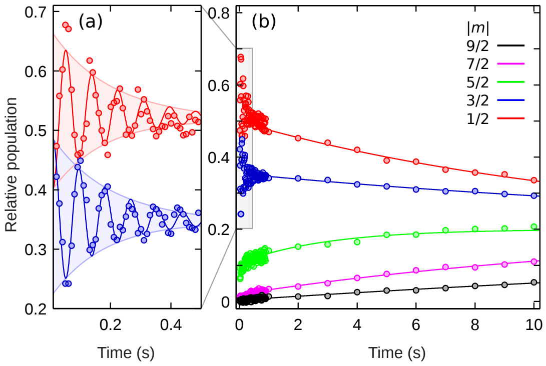

Figure 10.2: (a) Measurement of damped spin oscillations and subsequent relaxation towards equilibrium (b), observed in a 3D fermionic quantum gas with large spin. Depicted is the time evolution of the relative populations of all spin-components $\pm m$, starting from an initial superposition of all ten spin states. For the exact experimental configuration, see [85]. Solid lines are guides-to-the-eye. Note the three time scales of (i) the spin oscillations, (ii) their damping and (iii) the subsequent relaxation of the total system. The redistribution among all spin states occurs on a time scale of 10 s. The magnetic field is $B = 0.17\,\mathrm{G}$, particle number $N = 4.9 \times 10^5$ and temperature $T/T_{\mathrm{F}} = 0.22$. Taken from Ref. [59].

term is linear in scattering lengths and the time scale is determined by the scattering lengths and the external magnetic field. (ii) These oscillations are damped with a rate on the order of several hundred ms, as explained in section 9.3. The mechanism here are spin-conserving lateral (incoherent) collision, whose effect is a dissipation of single-particle spin coherences. They are a beyond mean-field effect and contained in the collision integral derived in chapter 4. This effect appears in a higher order in the Boltzmann equation (10.1) and is quadratic in a_S, but for ^{40}K, the spin-conserving scattering lengths are one order of magnitude greater than the spin-changing scattering lengths (see Table 8.4), hence the time scales of (i) and (ii) are not too distinct. (iii) The slow redistribution among the ten spin states on a much longer time scale on the order of tens of seconds. In this chapter we show that this is the result of spin-changing lateral collisions, also described by the collision integral in (10.1). Since this term is also quadratic in a_S and the corresponding scattering lengths are differences of a_S, hence very small, the time-scale is the longest of all three processes. It is worth noting that of course also spin-conserving forward scattering events exist, which appear in our theoretical description in the anticommutator in Eq. (10.1). We found that for our purposes, these effects are very small and can often be safely neglected. They mainly have an effect on the shape of the density distribution and hence do not affect the population of the spin components, as we show them in Figures 10.2–10.6, in a noticeable way.

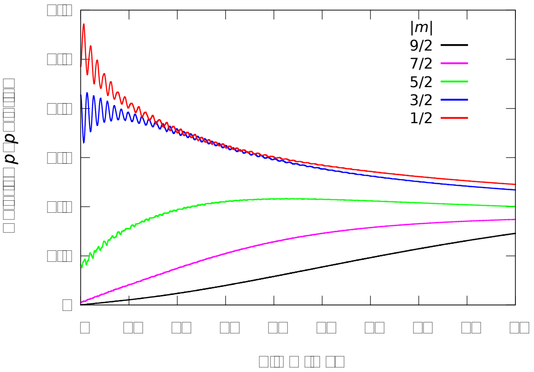

Figure 10.3: Numerical simulation of coherent oscillations, damping and relaxation in the 1D case. The initial spin configuration is the same as in Figure 10.2. Axial trapping frequency is $\omega_x = 2\pi \times 84\,\mathrm{Hz}$ and radial frequencies are $\omega_{y,z} = 2\pi \times 47\,\mathrm{kHz}$, particle number $N = 100$ per tube at temperature $T/T_\mathrm{F} = 0.2$ and magnetic field $B = 1.5\,\mathrm{G}$. As in Figure 10.2, we observe three time scales related to oscillations, damping and relaxation. Taken from Ref. [59].

10.2 Dissipative redistribution of spin occupations

In order to focus on the long-term spin relaxation (iii) shown in Figures 10.2(b) and 10.3, we omit the rf-pulse step in the preparation of the initial state. We leave the system in an incoherent mixture of $m = \pm 1/2$. This removes coherent spin-changing collisions described by the commutator in Eq. (10.1), since in this case the Wigner function and mean-field potential are always diagonal. The time-evolution is then fully determined by the anticommutator and the collision integral. For a direct comparison between theory and experiment, we realize a 1D system employing a deep 2D optical lattice, which confines the atoms into tight elongated tubes [109, 110] as described in chapter 5. As shown in Figure 10.4(a), the system gradually occupies all spin states and evolves towards a state of almost equal spin populations on a time scale of milliseconds. The 1D Boltzmann equation (10.1) reproduces the experimental results with great accuracy and without free parameters.

For experiments in the 3D case, we can again make use of the fact, that our trapping frequencies a sufficiently large to induce an effective long-range interaction (6.7). Hence, we apply the single-mode approximation to the collision integral as well, as described in section 6.6.1. This leads to the equation

$$\frac{d}{dt} M_{mn} = -\lambda \sum_{abcd} T^{abcd}_{mn} M_{ac} M_{bd}, \tag{10.2}$$

for the spin M_{mn}, where

$$T^{abcd}_{mn} = \frac{M}{4\pi\hbar^4} \left(\tilde{U}'_{mabd} \delta_{nc} + \tilde{U}'_{ncbd} \delta_{ma} - \sum_l U'_{malb} U'_{ncld} \right) \tag{10.3}$$

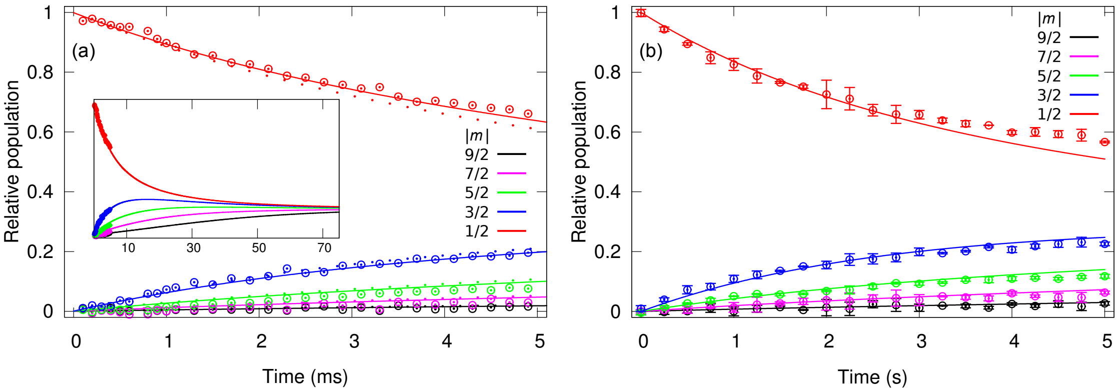

Figure 10.4: Comparison of spin relaxation for 1D and 3D. The initial spin configuration is a mixture of $m = \pm 1/2$. (a) Experimental data in a 1D geometry (circles) compared to numerical results (lines) from the 1D Boltzmann equation (10.1) and (dots) from a 1D version of the single-mode approximation (10.2). The axial trapping frequency is $\omega_x = 2\pi \times 84\,\mathrm{Hz}$ and radial frequencies are $\omega_{y,z} = 2\pi \times 47\,\mathrm{kHz}$, particle number $N = 100$ per tube at temperature $T/T_\mathrm{F} = 0.2$ and magnetic field $B = 0.12\,\mathrm{G}$. Inset: The system approaches a steady state for longer times. (b) Experimental data (circles) in a 3D configuration compared to calculations (lines) in single-mode approximation (10.2), $\vec{\omega} = 2\pi \times (33, 33, 137)\,\mathrm{Hz}$, $N = 1.3 \times 10^5$ and $T/T_\mathrm{F} = 0.15$ at $B = 0.34\,\mathrm{G}$. Adapted from Ref. [59].

and

$$\lambda = \frac{1}{N} \int d^3r \int d^3p \int d^3q |\vec{q}| f_0(\vec{r}, \vec{p}) f_0(\vec{r}, \vec{p} - \vec{q}). \tag{10.4}$$

Results of this equation are compared to experiments in Figure 10.4 (b).

For further insight we can also apply the single-mode approximation to the 1D case, as we derive in section 6.6.1. Here, for simplicity, the quadratic Zeeman shift has been neglected in the above equations, which are thus valid for small magnetic fields only (See chapter 6 for full equations). The comparison of single-mode calculations in Figure 10.4 to the experiment yields a surprisingly good agreement without free parameters. Note the qualitatively comparable behavior on different time scales of milliseconds for 1D and seconds for 3D. On the contrary the damping of the coherent spin oscillations visible in Figures 10.2 and 10.3 is not described by this approach. This results from the assumption for the single-mode approximation, i.e. that it completely neglects the multi-mode character of the fermionic many-body system and thus cannot account for spatial redistribution via lateral scattering events. We first investigate the behavior of this relaxation for different densities. As expected, an increase in density leads to a higher collision rate and hence faster relaxation, as we show in Figure 10.5. The measured redistribution rates are calculated for the transfer of atoms from $m = \pm 1/2$ components into $m = \pm 3/2, 5/2$ only, which are the first spin-components to be populated. The dependence is given by the parameter λ (10.4).

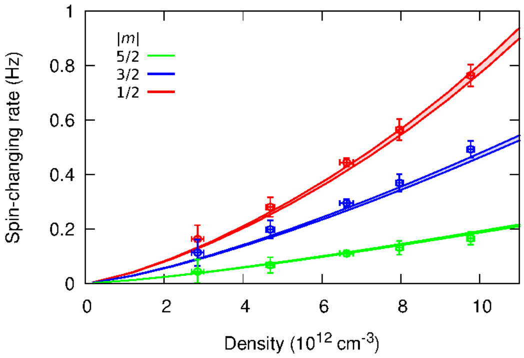

Figure 10.5: Density dependence of the spin relaxation rate in 3D, with an initial mixture of atoms in $m = \pm 1/2$. The spin-changing rate is obtained by fitting the solution of coupled rate equations to experimental (points) and theoretical (lines) data. Theoretical values are obtained using the single-mode approximation using Equation (10.2). The magnetic field is $B = 0.11$ G. We experimentally tune the density by changing the particle number, keeping the temperature constant at $T/T_\mathrm{F} = 0.26$. Taken from Ref. [59].

Of further interest is the influence of the magnetic field on the relaxation process. As the Zeeman energy of a pair of atoms changes during a spin-changing collision, a strong magnetic field suppresses this process by increasing the energy difference between the initial and final spin configuration. In Figure 10.6, we depict the experimentally obtained populations of the spin components after 2 s as a function of the magnetic field strength and compare them to single-mode in 3D (a) and 1D calculations (b) after 2 ms. In both cases, the general behavior is very similar and shows a suppression of spin-changing collisions for large magnetic fields. Spin configurations with high values of $|m|$ are energetically separated from the initially populated $m = \pm 1/2$ by the quadratic Zeeman effect and are only occupied at very low field strengths. By changing the magnetic field we can thus tune the magnitude of spin-changing collisions relative to the unaffected spin-conserving collisions up to a complete suppression. This gives us the possibility to treat the $m = \pm 1/2$ subsystem as a dissipative two-component Fermi gas with a tunable loss mechanism.

10.3 Time evolution of temperature

The collision integral of Eq. (10.1) enables us to determine whether our system is in the collisionless, hydrodynamic or an intermediate regime by calculating the average collision times and comparing them to the trapping frequency. The average collision time in the 3D setup [77],

$$\tau_{\mathrm{3D}} \sim (4\pi a^2 n_p v)^{-1}, \tag{10.5}$$

with the relevant scattering length a, peak density n_p and velocity $v = \max(v_T, v_F)$, where $v_T = \sqrt{k_\mathrm{B}T/M}$ denotes the thermal velocity and $v_F = \sqrt{2E_\mathrm{F}/M}$ the Fermi

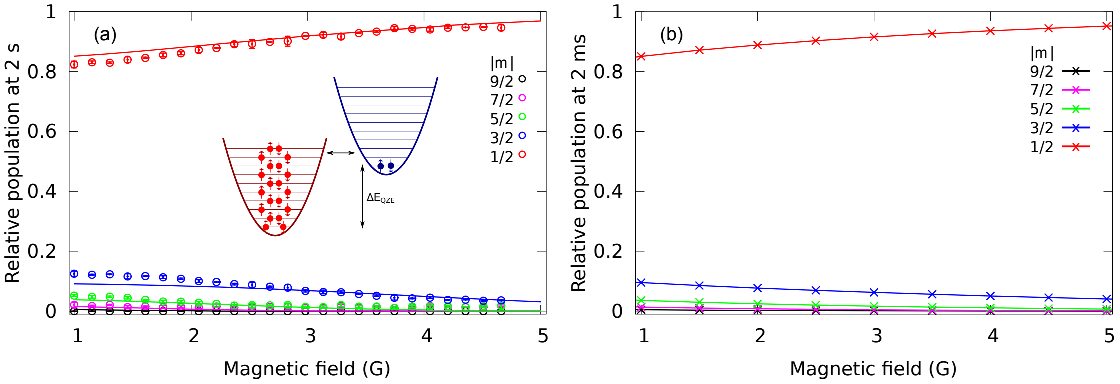

Figure 10.6: Dependence of spin relaxation on magnetic field. (a) Experimental data, obtained from a 3D experiment (circles) and theoretical results from a single-mode approach (lines). Spin populations are measured after 2 s. (b) Spin populations after 2 ms, as obtained from full 1D simulations. The inset sketches how the interplay of differential QZE and Fermi energy determines the probabilities for lateral spin-changing collisions. Adapted from Ref. [59].

velocity. This collision time ranges from $\sim 10\,\mathrm{ms}$ to $\sim 50\,\mathrm{ms}$ for spin-conserving collisions and $\sim 1\,\mathrm{s}$ to $\sim 5\,\mathrm{s}$ in the spin-changing case. Compared to the average trapping frequency of $\bar{\omega} = (\omega_x \omega_y \omega_z)^{1/3} \approx 2\pi \times 58\,\mathrm{Hz}$, we obtain values for $\bar{\omega}\tau_{3\mathrm{D}}$ between 3.5 and 17 for the spin-conserving collisions and between 350 and 1700 in the spin-changing case. The lowest and highest values of $\bar{\omega}\tau_{3\mathrm{D}}$ are reached for the lowest and highest densities shown in Figure 10.5 respectively. This means we can approach the hydrodynamic regime, where the collision rate is larger than $\bar{\omega}$ and local equilibrium can be established. On the other hand our system becomes almost collisionless regarding the spin-changing collisions and generally we are in an intermediate regime. In the 1D case, collision times $\tau_{1\mathrm{D}} \sim (n_p \omega_y \omega_z a^2 / v_T)^{-1}$ are on the order of 1 ms and 110 ms respectively, meaning that $\omega\tau_{1\mathrm{D}} \sim 0.6$ and $\omega\tau_{1\mathrm{D}} \sim 60$, concerning spin-conserving and spin-changing collisions respectively [59].

This discussion allows us to make the following assumption. If we consider the system to be in the hydrodynamic regime regarding the spin-conserving collisions, we can assume that at each time, the atoms in a pair of spin states $\pm 1/2$ are close to an equilibrium state defined by its current particle number and energy and hence can be assigned a well-defined temperature. On the other hand, spin-changing collisions are at least two orders of magnitude weaker and very slowly change the particle number in each subsystem. This situation is similar to prethermalization, where first a "prethermal" state is reached under the assumption of conserved quantities, which on a much longer time scale are actually not fully conserved due to a "slightly broken symmetry", leading eventually to full thermalization [52]. In our case, the role of the nearly conserved quantities is played by the occupation numbers of the ten spin states, which change only on a very long time scale. The "slightly broken symmetry" here would be the SU(N) symmetry one would

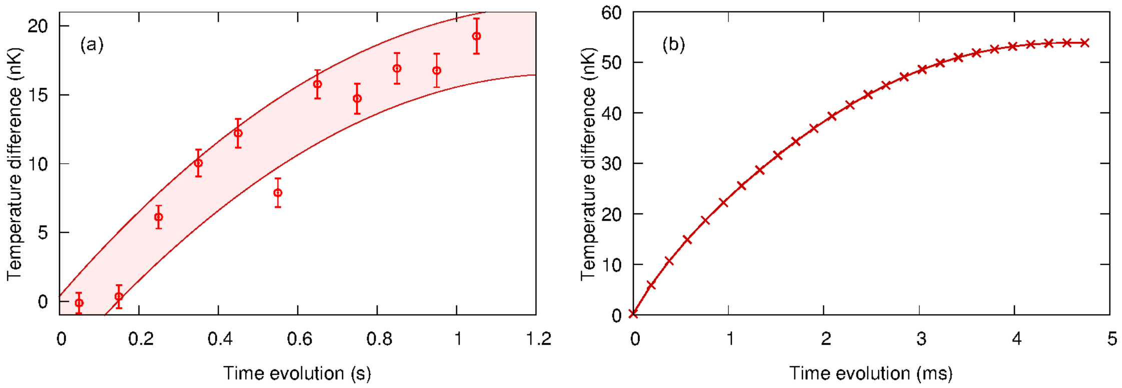

Figure 10.7: Temperature increase due to spin redistribution. (a) Time evolution of the temperature difference between a closed (high magnetic field at $B = 7.6\,\mathrm{G}$) and a maximally open system (low magnetic field at $B = 0.12\,\mathrm{G}$). The shaded area serves as a guide-to-the-eye. The particle number is $N = 3.9 \times 10^5$ at an initial temperature $T = 0.24\,T_\mathrm{F} = 65\,\mathrm{nK}$. (b) Results from a simulation of the 1D equation (10.1) at magnetic fields $B = 0.1$ G and $B = 8$ G. Adapted from Ref. [59].

have if all scattering lengths were equal.

With the results of Figure 10.6 in mind, we compare two situations. We start with all particles in a mixture of $m = \pm 1/2$ and let the system evolve for a weak magnetic field, where spin-changing collisions reduce the particle number in $m = \pm 1/2$ over time, and for a strong magnetic field, where it stays constant. We then measure the temperature in both cases and compare it. In the 1D case, we extract and define the temperature as follows. Since at each time, we have the full Wigner function available, and can compare the distribution of e.g. the $m = 1/2$ component $W_{\frac{1}{2}\frac{1}{2}}(x,p,t)$ to a non-interacting equilibrium distribution $f_0(x,p,t)$ (6.29), that corresponds to the same particle number and single-particle energy as $W(x,p,t)$:

$$N(t) = \int dx \int dp f_0(x,p,t) = \int dx \int dp W_{\frac{1}{2}\frac{1}{2}}(x,p,t) \tag{10.6}$$

$$\begin{aligned} E(t) &= \int dx \int dp \left(\frac{p^2}{2M} + \frac{1}{2}M\omega^2 x^2\right) f_0(x,p,t) \\ &= \int dx \int dp \left(\frac{p^2}{2M} + \frac{1}{2}M\omega^2 x^2\right) W_{\frac{1}{2}\frac{1}{2}}(x,p,t). \end{aligned} \tag{10.7}$$

This distribution is also equivalently fully determined by temperature and chemical potential, so we calculate at each time t the particle number and trap energy of $W(x,p,t)$ and generate a Fermi distribution $f_0(x,p,t) = f_0(N(t),E(t)) = f_0(\mu(t),T(t))$ with the same values for $N(t)$ and $E(t)$. The temperature of this distribution is plotted in Figure 10.7(b) as an estimate for the temperature of W. The overlap between this equilib-

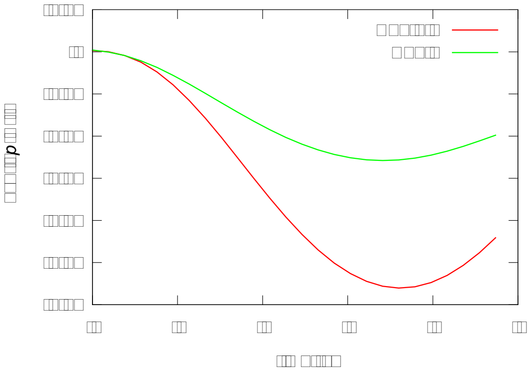

Figure 10.8: Overlap between a non-interacting equilibrium distribution and the Wigner function during the simulations performed to obtain the temperatures in FIG. 10.7(b). Taken from Ref. [59].

rium distribution and the Wigner function,

$$R(t) = \frac{\int dx \int dp f_0(x,p,t) W_{\frac{1}{2}\frac{1}{2}}(x,p,t)}{\int dx \int dp W_{\frac{1}{2}\frac{1}{2}}(x,p,t) W_{\frac{1}{2}\frac{1}{2}}(x,p,t)}, \tag{10.8}$$

is plotted in Figure 10.8 and for the times we consider maintains sufficiently large values.

In the experimental 3D case, for both values of the magnetic field, we observe a small heating rate, which we mainly attribute to inelastic photon scattering. However, at low magnetic fields, the heating rate is significantly increased. In Figure 10.7(a), we plot the temperature difference to extract the heating contributions solely generated by spin-changing collisions. This additional increase in temperature is due to hole creation in the Fermi sea [111] by scattering into the unoccupied spin states. We initially prepare a very cold two-component Fermi sea, with only few unoccupied trap levels below the Fermi energy. Losses through spin-changing collisions "perforate" this Fermi sea with holes, such that the experimentally obtained temperature increases. Simulations of Eq. (10.1) for the 1D case reproduce this behavior (see Figure 10.7(b)).

In summary, the Boltzmann approach derived in chapter 4 provides a theoretical description of non-equilibrium spin-changing dynamics and relaxation with very good agreement to the experimental results and is well suited for the quantitative description of weakly interacting fermionic many-body systems with large spin. Both, the comparison of numerical simulations with full spatial resolution to a 1D experiment as well as the comparison of a simplified single-mode approximation to a 3D experiment yield a very good agreement without free parameters. Moreover, the microscopically derived collision integral allows for a clear identification of several types of scattering processes: Spin-changing vs. spin-conserving collisions, processes depending on density vs. processes depending on gradients of density, and forward vs. lateral scattering. By tuning the magnetic field, we can precisely control the coupling strengths of individual spin-changing collision channels, allowing to tune the character of a subsystem of two spin components within the large-spin Fermi sea continuously from an open to a closed system. The spin relaxation manifests itself in a perforation of the Fermi sea accompanied with a temperature increase.

Chapter 11

Conclusions and outlook

In this thesis, we have addressed a number of fundamental problems concerning the dynamics of ultracold atoms. We have developed a theoretical framework that allows us investigate many facets of the spin dynamics of large-spin Fermi gases and shows remarkable agreement with experiments. Our method is able to simulate non-equilibrium dynamics and relaxation of closed quantum many-body systems even for long time scales and is suitable for systems with arbitrarily large spins and the corresponding large number of scattering channels. We have advanced the knowledge on the dynamics of Fermi gases is several respects.

We have shown that for weakly-interacting systems, the harmonic trap is a very important ingredient and its effect on the dynamics cannot be neglected. It also leads to qualitatively new behavior beyond the local density approximation. We have shown, that the trap can be the dominating dynamical process, when it induces effective long-range interactions. It is crucial if experimentalists want to focus on the internal dynamics of the system, as it prevents dephasing and stabilizes the orbital degrees of freedom. Trapped Fermi systems can hence be engineered such that their dynamics becomes collective, allowing us to describe them in a very simple fashion.

Moreover, the clear distinction we can make between coherent and incoherent processes is vital, when it comes to distinguishing, whether an observed damping of coherent dynamics is caused by true single-particle decoherence induced by collisions, or an accumulation of dephasing caused by mean-field interactions. Our study of spin waves complements earlier work on Helium, Bosons and two-component Fermi gases and we have thoroughly studied means of controlling spin currents in a multicomponent system. By investigating the interplay of higher-order spin tensor components, we contributed to the understanding of the dynamics of such non-trivial phases, which only occur in large-spin systems.

In this thesis, we presented the first study of collective spinor dynamics in a large-spin many-body ultracold Fermi system. This might open a new field such that the spin degree of freedom might become a valuable component for both experimental and theoretical work on ultracold Fermi gases. We showed that spinor dynamics with large amplitudes and long lifetimes can actually be observed, we also discussed reasons, why earlier experiments with Fermions may not have reported seeing such effects. We showed that magnetic field gradients, or trap geometries can lead to almost instant dephasing. We performed a detailed study of the dependence of fermionic spinor dynamics on important system parameter. Further, we found out how a complex interplay of coherent and incoherent interactions creates an unexpected region of stability for an excited state.

Our last contribution is to the currently very active field of the relaxation of closed quantum systems. In this thesis, we showed how processes, which happen on different time scales, lead to relaxation first in subsystems defined by two spin states, before at much larger times the entire system reaches a steady state, a situation that bears some resemblance to prethermalization. We further demonstrated that with a suitable initial state and a change in magnetic field, we can change from a closed system defined by the initially populated spin components to an open system with a controllable loss mechanism.

11.1 Outlook

This thesis opens the path for further work on ultracold Fermi gases, including extensions to the main theory presented here. One possibility would be to include another fermionic feature – pairing – to the description, which could be achieved by adding the anomalous terms in the Wick decomposition (3.15). This way, the dynamics of a quench from a phase without pairing to one, where it becomes relevant could be investigated, with the additional feature of doing it with large spins. Pairing of large spins can lead to very complex situations, where pairs of different total spins form and in general can appear all at once. It may then be possible, to combine a kinetic equation describing the dynamics of the normal component of the Fermi gas and one for the pairs in a similar fashion as the Zaremba-Nikuni-Griffin theory, which describes the dynamics of a BEC coupled to its thermal cloud [112, 113].

Another possibility is the combination of large-spin physics with dipolar physics. A new generation of ultracold atom experiments is currently undergoing progress, which involve degenerate gases of Lanthanide atoms. These atoms have far larger spins than even ^{40}K, up to $F = 11$ for bosonic ^{165}Ho [99] and $F = 21/2$ for fermionic ^{161}Dy and ^{163}Dy [114]. These atoms have a very large magnetic moment, such that dipole-dipole interactions are strong and cannot be neglected. Dipolar interactions lead to the violation of the conservation of total spin during collisions [45], which was a valid assumption throughout this thesis. Without this conservation, even richer spinor dynamics are expected. For spinor BECs, studies have been performed on effects such as the Einstein-De Haas effect in a dipolar BEC [105, 106], where violation if total spin conservation leads to orbital angular momentum. Likewise, such interplay of large spins and orbital angular momentum could be worthwhile to study in Fermions as well.

Acknowledgments

With this thesis coming to its end, it is time to thank all those who have made this work possible. First of all, I thank my supervisors. Maciej Lewenstein deserves the highest praise for his constant support, patience and willingness to grant me great freedom in my work. André Eckardt has been a constant source of fruitful input and support, both during his time at ICFO and later from a distance. My gratitude goes to both of them for, owing to their own previous joint work with that group, making the collaboration with the Hamburg group possible. I would also like to thank the members of my thesis committee, Prof. Sandro Stringari, Prof. Dan Stamper-Kurn, Prof. Darrick Chang and substitutes Prof. Anna Sanpera and Prof. Leticia Tarruell.

The collaboration with the experimental group in Hamburg in a way completely changed the scope of my Ph.D. project. Consequently, I would like to thank all my collaborators in Hamburg. This collaboration made the last three years of my PhD a very different experience, with its high intensity of mutual exchange of knowledge. I would like to thank Jannes Heinze and Jasper Simon Krauser, my main contacts in Hamburg, as well as Nick Fläschner, Christoph Becker, Klaus Sengstock and all members of the Institute for Laser Physics for their hospitality during several visits and many fruitful discussions.

A special mention also has to go to Luis Santos in Hannover, for sparking my interest in cold atoms. He not only encouraged me to do a PhD in Barcelona, but also supported me in getting started there.

For their company and support during my stay at ICFO, as well as bearing with me as the tenacious organizer of the weekly group seminar for five years, I would like to thank all members of the Quantum Optics Theory group at ICFO. In fact, mentioning all members present at one point or another during my very long stay in that group in these acknowledgments bears a non-zero chance of forgetting someone. Hence, I would like to thank Ujjwal and Aditi Sen, Jarek Korbicz, Christian Trefzger, Armand Niederberger, Mirta Rodríguez, Anna Kubasiak, Sibylle Braungardt, Lluìs Masanes, Remigiusz Augusiak, Omjyoti Dutta, John Lapeyre, Pietro Massignan, Fernando Cucchietti, Gergely and Edina Szirmai, Philipp Hauke, Tobias Grass, Alejandro Zamora, Søren Gammelmark, Alessio Celi, Julia Stasińska, Michał Maik, Anna Przysiezna, Simon Moulieras, Christine Muschik, Javier Rodríguez Laguna, Piotr Migdał, Jordi Tura, Luca Tagliacozzo, Bruno Julia, Ravindra Chhaylani, Andy Ferris, Alexander Streltsov, Aniello Lampo, Samuel Mugel and everyone else in the group.

Of those names, special thanks go to my office mates Armand Niederberger, Anna Kubasiak, Søren Gammelmark, Anna Przysiezna, Jordi Tura and Julia Stasińska for their friendship as well as their patience toward someone who would spend entire afternoons talking on the phone with his collaborators.

This work has also been possible due to the support from ICFO's staff, who do a great job in keeping the tedious administrative elements of work away from the scientists as best as possible. A special mention here goes to Susan Horvath, Anne Gstöttner, Mery Gil and the rest of the Human Resources department.

Finally, I would like to express my gratitude to all those friends who made my stay in Barcelona a pleasant one. Om, Bruno, Tobias and Alejandro have been mentioned above already, however they have been far more than just great colleagues for me. Then, there were Josi Fonseca, Chirag Dhara, Can Yao, Roberto Leon, Jiri Svozilik, Yannick de Icaza, Marta Abad, Osamu Takayama, and many other friends. Actually, the city itself deserves a mention for being such a wonderful place – albeit full of distractions – to pursue a PhD.

On the financial side, this work was supported by the Spanish Ministerio de Ciencia e Innovación through an FPI-fellowship, as well as through the projects QOIT, FerMix, AAII-Hubbard and TOQATA. Further support came from european projects EU STREP NAMEQUAM, EU IP SIQS and ERC Grant QUAGATUA and OSYSRIS.

Appendix A

Zeeman effect in Potassium

In this appendix, we give a short overview of some basic properties of ^{40}K, which are relevant for our results. For more details, like Feshbach resonances and properties of other isotopes of Potassium, we refer to the appendix of Ref. [115], on which this appendix is based. The electronic ground state of ^{40}K is $4^2S_{1/2}$, which has electron spin $S = 1/2$ and orbital angular momentum $L = 0$. The electronic total angular momentum $\vec{J} = \vec{L} + \vec{S}$ is then given by a single quantum number $J = 1/2$. The total spin is given by the coupling of electron angular momentum and nuclear spin $\vec{F} = \vec{J} + \vec{I}$. The nuclear spin of ^{40}K is $I = 4$, hence in the ground state, ^{40}K has two hyperfine manifolds, with $F = 7/2$ and $F = 9/2$. In all the experiments featured in this thesis, the atoms are trapped in the $F = 9/2$ manifold. However, the other hyperfine manifold is useful for experimental procedures, in the sense that atoms can be transferred from $F = 9/2$ to $F = 7/2$ to become invisible for the detection light used. This is described in the next appendix B and in far greater detail in Ref. [85].

In a magnetic field $\vec{B}$, the Zeeman interaction is described by the Hamiltonian

$$\hat{H} = \frac{\mu_B}{\hbar}\left(g_J\vec{J} + g_I\vec{I}\right)\cdot\vec{B}, \tag{A.1}$$

where μ_B is the Bohr magneton, and g_J is the electron Landé factors and g_I the nuclear gyromagnetic factor. For ^{40}K, these factors are $g_J = 2.00229421(49)$ and $g_I = 0.000176490(34)$ [116]. The eigenvalues of this Hamiltonian for $L = 0$ and $S = 1/2$ are given by the Breit-Rabi formula [117]

$$E_{\text{hfs}}(B) = -\frac{a_{\text{hfs}}}{4} + g_I\mu_B mB \pm \frac{1}{2}a^{\text{hfs}}(I+1/2)\sqrt{1 + \frac{4mx}{2I+1} + x^2}, \tag{A.2}$$

where

$$x = \frac{(g_J - g_I)\mu_B}{a^{\text{hfs}}(I+1/2)}B. \tag{A.3}$$

The hyperfine structure coefficient is given by $a_{\text{hfs}} = -285.7308(24)\,h \times \text{MHz}$ for the ground state of ^{40}K [116]. The sign $\pm$ corresponds to the manifold with $F = 7/2$ $(-)$ and $F = 9/2$ $(+)$ respectively. In Figure A.1 we plot the Zeeman splitting of

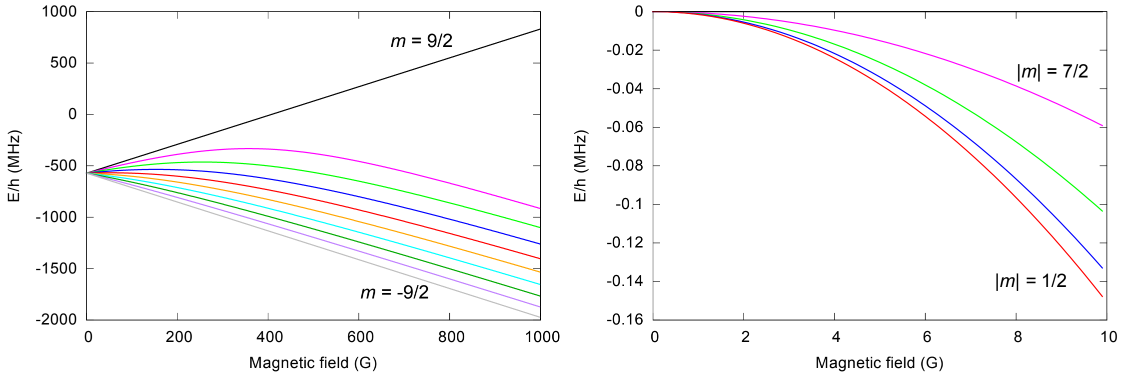

Figure A.1: Zeeman splitting in the $F = 9/2$ hyperfine manifold of ^{40}K. Left: Energy splitting obtained from the full Breit-Rabi formula (A.2) for a wide range of magnetic fields up to 1000 G. Right: Quadratic part of the Breit-Rabi formula for magnetic fields of the order of magnitude relevant for the results in this thesis.

the relevant $F = 9/2$ hyperfine manifold, once with the full Breit-Rabi formula (left), and also subtracting the linear term (in the Larmor frame, right). Since spin-changing collisions preserve total spin, the right figure is the more relevant graph for this thesis. For convenience, throughout this thesis we approximate the non-linear part of the Breit-Rabi formula with its quadratic term,

$$Q = -\frac{a^{\text{hfs}} x^2}{18}, \tag{A.4}$$

as this is a good approximation in the range of magnetic fields we consider, which rarely exceed 1 G.

Appendix B

Experimental techniques

In this appendix, we give a description of the experimental methods used by the Hamburg group to prepare the degenerate gas of ^{40}K and perform measurements on it. This appendix is based on the following publications: [57–59, 90]. For even more details, e.g. on the apparatus itself we refer to [85].

B.1 Preparation of the ultracold Fermi gas

The atoms are first cooled sympathetically to a temperature of typically $0.1\,T_\mathrm{F}$. This process happens in a magnetic trap, in which the atoms are polarized in the hyperfine state $|F=9/2, m=9/2\rangle$, and bosonic bosonic ^{87}Rb is used as a buffer gas. The atoms are then transferred into a crossed circular-elliptical optical dipole trap operated at a wavelength of $\lambda = 812\,\mathrm{nm}$. Using radio-frequency (rf) pulses and rf-sweeps, a spin mixture is created, which is subsequently evaporated to quantum degeneracy by lowering the power of the dipole trap exponentially in 2 s. This results in a sample with particle numbers of the order of $N \sim 10^5$ at temperatures of $T = 0.1 - 0.2\,T_\mathrm{F}$. After the evaporation, the trap is compressed again to avoid particle loss during the experiments, realizing typical trapping frequencies of $\vec{\omega} = 2\pi \times (70, 70, 12)\,\mathrm{Hz}$ for the spin wave experiments described in chapter 8 or $\vec{\omega} = 2\pi \times (33, 33, 137)\,\mathrm{Hz}$ for the experiments on spin dynamics in chapters 9 and 10. Uncertainties for the trapping frequencies are about 10%.

B.1.1 Initial spin configurations

By varying the evaporation sequence and including additional waiting times, the initial temperature and particle number can be controlled independently in the same trap geometry. This allows to modify the density while keeping T/T_F approximately constant, important for the results in chapters 9 and 10, where density effects are studied. Typically, a balanced mixture of atoms in spin states $m = \pm 1/2$ is used as initial state, on which rf-pulses can be applied, as described in section 8.3.

It is also possible to choose a different two-component mixture, e.g. $m = \pm 3/2$ for the stability analysis in section 9.4. This procedure is more elaborate, as only the pair

$m = \pm 12$ with the lowest quadratic Zeeman energy can be evaporatively cooled directly. A mixture of $m = \pm 3/2$ is prepared as follows. At a magnetic field of $B = 50\,\mathrm{G}$, a mixture of $m = -1/2, 3/2$ is evaporated, which unlike $m = \pm 3/2$ is stable to losses, because Pauli blocking prevents spin-changing collisions into spin configurations with lower Zeeman energy. After this mixture has been sufficiently cooled down evaporatively, a short rf-sweep of 2 ms is performed to transfer the atoms from the $m = -1/2$ into the $m = -3/2$-state.

B.1.2 Creation of a 1D geometry

The 1D configuration used in chapter 10 is realized by adiabatically ramping up a 2D optical square lattice over 150 ms. The lattice is created by two orthogonal retro-reflected laser beams at wavelength $\lambda = 1030\,\mathrm{nm}$ with a $1/\mathrm{e}^2$-radius of $200\,\mu\mathrm{m}$ detuned with respect to each other by several tens of megahertz. The lattice depth is $25\,E_{\mathrm{recoil}}$ with $E_{\mathrm{recoil}} = \frac{\hbar^2 k_{\mathrm{L}}^2}{2M}$, where $k_{\mathrm{L}} = \frac{2\pi}{\lambda}$. This creates an array of 1D tubes, where a single tube can be described as a harmonically trapped system with frequencies $\omega_x = 2\pi \times 84\,\mathrm{Hz}$ and $\omega_{y,z} = 2\pi \times 47\,\mathrm{kHz}$. With a particle number of $N \approx 100$ and $E_{\mathrm{F}} = 2\pi\hbar \times 37\,\mathrm{kHz}$, the radial trapping frequencies fulfill $\hbar\omega_{y,z} > E_{\mathrm{F}}$ and at a temperature $k_{\mathrm{B}}T = 0.2\,E_{\mathrm{F}}$, a possible population of excited radial modes can be neglected, hence a true 1D system is created. The extension of the radial ground state is around 1378 Bohr radii and thus one order of magnitude larger than the scattering lengths.

B.2 Measurement

The experimental results shown in this thesis roughly depend on three types of measurement. Either, the relative population of the spin components is counted, like e.g. in chapter 9. In some cases, density profiles are mapped, which can be achieved by in-situ measurement or time-of-flight (TOF) measurement. The former will provide the spatial distribution, the latter the momentum distribution, in the ideal case of an infinite time-of-flight.

B.2.1 Spin populations

The relative populations of spin components are measured as follows: The atoms are released from the trap by suddenly switching off all optical potentials. An inhomogeneous magnetic field is used to separate the spin components during a time-of-flight expansion of typically 18.5 ms. Then, the number of atoms in each spin component is counted with resonant absorption imaging, giving the relative populations of each spin components. Performing the same procedure without the inhomogeneous magnetic field allows to independently total particle number as well.

B.2.2 Spin waves

Two different detection schemes are used to measure the distributions and spatial oscillation frequencies of the individual spin components in the case of spin waves. In most of these experiments, time-of-flight imaging is used, as described above, however, the entire distribution of each spin component is mapped. From this, the center-of-mass position can be calculated for each of the separated clouds individually. This method has the advantage that all spin-components can be detected simultaneously, but with a finite free expansion time of 18.5 ms, the momentum distribution is not obtained perfectly and spatial and momentum components are mixed. This washes out all but the spatial dipole modes.

To obtain more information on the spatial modes of the excited spin-waves, an in situ detection protocol is used as well, which allows us to measure the distribution in position space. With this method, also breathing modes can be measured, in which the center-of-mass is stationary. In this method, instead of separating the different spin components by a Stern-Gerlach procedure in TOF, microwave pulses at 1.3 GHz are used to transfer all but one single component to the $F = 7/2$ manifold of ^{40}K. This manifold is off-resonant to the detection light, and consequently the transferred atoms do not appear in the absorption images and a single spin-component can be measured individually.

This is done by switching off all magnetic fields and optical potentials for 1 ms to detect the atomic sample. To record the time evolution of all four components, it is therefore necessary to repeat the full measurement four times.

B.2.3 Temperatures

To determine the initial temperature of the gas, the initial two-component spin mixture is released from the trap and a fugacity fit is employed, which is independent of the particular trapping frequencies. This is applied after a time-of-flight of typically 21 ms without a Stern-Gerlach field and without spin-changing dynamics. The temperature determination is performed separately to avoid deformations of the cloud due to the Stern-Gerlach field.

In order to extract the change in temperature over time for a two-component subsystem in Figure 10.7, the temperature is determined only in one spin component. This circumventing deviations associated with the imbalance of the spin mixture. For instance, to measure the temperature in $m = 1/2$ a sequence of linearly polarized microwave pulses with a duration of $50\,\mu s$ is applied to transfer all significantly occupied spin components $m \neq 1/2$ into the $F = 7/2$ hyperfine manifold of ^{40}K. In the other hyperfine manifold the atoms are not resonant with the detection light and are thus obscured during the absorption imaging process, and the procedure described above can be applied to the remaining spin component individually.

Appendix C

Numerical simulations

In this thesis, we perform numerical simulations of 1D Boltzmann equations, collisionless (5.11) or with the collision term (5.37). These are partial differential equations with one time t and two phase-space variables x, p. To illustrate how we implement our simulations, let us first remember the dimensionless units we used in chapter 6 in the derivation of the dynamically induced long-range interaction. We scale all relevant quantities with the trapping frequency ω: The length then given in units of $l_0 = \sqrt{\frac{\hbar}{M\omega}}$, momenta as $p_0 = \sqrt{M\hbar\omega}$, time with $t_0 = 1/\omega$ and energies in units of $E_0 = \hbar\omega$. For simplicity, we start with the non-interacting spinless system, which is in dimensionless units described by the equation

$$\frac{\mathrm{d}}{\mathrm{d}t}W(x,p) = -p\partial_x W(x,p) + x\partial_p W(x,p), \tag{C.1}$$

the phase-space representation of the harmonic oscillator. Partial differential equations of this type appear frequently in fluid mechanics, with prominent examples such as Burgers' or Navier-Stokes equations. Terms such as $x\partial_p$ are called advective derivatives. We now want to discretize Eq. (C.1) for numerical treatment. We discretize time, position and momentum by introducing steps of constant length. Hence, the phase space is now defined on a rectangular grid with tiles of size $\Delta x \Delta p$. Throughout this thesis, we use a square grid, where in dimensionless units $\Delta x = \Delta p \equiv \Delta$. We use an even amount of grid points and divide a square of phase-space into a grid of $N \times N$ points defined as $(x_i, p_j) = \Delta(i - N/2, j - N/2)$. The discretized Wigner function is the defined as $W^i_{kl} \equiv W(x_k, p_l, t_i)$.

C.1 Finite differences

To discretize the derivative, we remember that if a function $f(x)$ can be expanded in a Taylor series,

$$f(x+\Delta) = f(x) + \frac{\partial f}{\partial x}\Delta + \frac{\partial^2 f}{\partial x^2}\frac{\Delta^2}{2} + \ldots, \tag{C.2}$$

the first order term corresponds to the first derivative. For a discretized function $f_j = f(x_j)$ with $f(x_j + \Delta) = f_{j+1}$, this means

$$f_{j+1} = f_j + \left(\frac{\partial f}{\partial x}\right)_j \Delta + \left(\frac{\partial^2 f}{\partial x^2}\right)_j \frac{\Delta^2}{2} + \dots . \tag{C.3}$$

If we truncate the Taylor series after the first order to approximate f_{j+1}, we obtain

$$f_{j+1} \approx f_j + \left(\frac{\partial f}{\partial x}\right)_j \Delta, \tag{C.4}$$

and in discretized space, the derivative can be approximated as a finite difference quotient

$$\left(\frac{\partial f}{\partial x}\right)_j = \frac{f_{j+1} - f_j}{\Delta} + \mathcal{O}(\Delta) \tag{C.5}$$

The symbol $\mathcal{O}$ denotes terms of order Δ and above, which tells us the error we have made by truncating the Taylor expansion (C.3). On the grid, Eq. (C.5) means that the derivative of function f at grid point j is given by (C.5) and hence depends on the function at point j and the grid point to the right, $j + 1$.

Hence, this approximation is called the *forward difference.* We can also approximate the expression

$$f_{j-1} \approx f_j - \left(\frac{\partial f}{\partial x}\right)_j \Delta, \tag{C.6}$$

such that the discretized derivative is given by

$$\left(\frac{\partial f}{\partial x}\right)_j = \frac{f_j - f_{j-1}}{\Delta} + \mathcal{O}(\Delta), \tag{C.7}$$

what is called the *backwards difference.* It depends on grid point j and its left neighbor, $j - 1$. The difference of Equations (C.5) and (C.7),

$$f_{j+1} - f_{j-1} = 2\left(\frac{\partial f}{\partial x}\right)_j \Delta + \dots \tag{C.8}$$

provides us another discretized derivative,

$$\left(\frac{\partial f}{\partial x}\right)_j = \frac{f_{j+1} - f_{j-1}}{2\Delta} + \mathcal{O}(\Delta^2). \tag{C.9}$$

This discretized derivative is called the central difference, and is of higher order and hence higher accuracy, as the second term in the Taylor expansion drops out. If we extend this formalism to the two phase-space variables, the right hand side of Eq. (C.1) can be written e.g. in three forms, depending on what finite difference we use to approximate the derivatives of position and momentum:

$$\frac{W_{kl}^{i+1}-W_{kl}^{i}}{\Delta t} = -p_l \frac{W_{k+1,l}^{i}-W_{kl}^{i}}{\Delta} + x_k \frac{W_{k,l+1}^{i}-W_{kl}^{i}}{\Delta} \tag{C.10a}$$

$$\frac{W_{kl}^{i+1}-W_{kl}^{i}}{\Delta t} = -p_l \frac{W_{kl}^{i}-W_{k-1,l}}{\Delta} + x_k \frac{W_{kl}^{i}-W_{k,l-1}^{i}}{\Delta} \tag{C.10b}$$

$$\frac{W_{kl}^{i+1}-W_{kl}^{i}}{\Delta t} = -p_l \frac{W_{k+1,l}^{i}-W_{k-1,l}^{i}}{2\Delta} + x_k \frac{W_{k,l+1}^{i}-W_{k,l-1}^{i}}{2\Delta} \tag{C.10c}$$

Mixed cases, e.g. forward difference in momentum and backward in space would also be possible. In the time domain, we can also choose between the forward difference

$$\left(\frac{\partial W(x,p,t)}{\partial t}\right)_{kl}^{i} = \frac{W_{kl}^{i+1}-W_{kl}^{i}}{\Delta t}, \tag{C.11}$$

we used above, and the backward difference

$$\left(\frac{\partial W(x,p,t)}{\partial t}\right)_{kl}^{i} = \frac{W_{kl}^{i}-W_{kl}^{i-1}}{\Delta t}. \tag{C.12}$$

Numerical methods using (C.11) are called *explicit*, where the function, propagated to the next point in time depends explicitly on the previous function, while methods using (C.12) are called *implicit*, as the (known) previous function depends on the function after the time step, hence the map on the right hand side of a partial differential equation must be inverted to obtain the time step. Mixed methods are also possible, with the Crank-Nicolson technique [118] as a famous example.

C.2 MacCormack's method

After the preparatory steps in the previous sections, we now introduce our numerical method of choice, the MacCormack method. This method is an explicit method, simple to implement and second-order accurate in space and time, even though it only uses forward and backward differences ([119]). It was first developed in 1969 for Navier-Stokes equations to describe impact craters of small hypervelocity projectiles on spacecraft [120]. It is easy to program [119] and does not introduce artificial numerical diffusion. In this method, the time step is calculated as an "average" time derivative $(\partial W/\partial t)_{\text{avg}}$ in between the points t and $t+\Delta t$ in time. This is calculated using two steps, a *predictor* step and a *corrector* step.

In MacCormack's method, we first evolve the function W_{kl}^{i} in time using only forward derivatives on the right hand side of Eq. (C.1):

$$\left(\frac{\partial W}{\partial t}\right)_{kl}^{i} = -p_l \frac{W_{k+1,l}^{i}-W_{kl}^{i}}{\Delta} + x_k \frac{W_{k,l+1}^{i}-W_{kl}^{i}}{\Delta}. \tag{C.13}$$

The predicted value of the Wigner function after the time step,

$$\bar{W}_{kl}^{i+1} = W_{kl}^{i} + \Delta t \left(\frac{\partial W}{\partial t}\right)_{kl}^{i}, \tag{C.14}$$

is calculated using the Wigner function before the time step, assumed to be knows. This intermediate value is of first order accuracy (see the forward difference (C.10a)). The corrector step calculates a new value of $(\partial\bar{W}/\partial t)$ using backward differences on the right hand side with the predicted values of the Wigner function $\bar{W}_{kl}^{i+1}$ as initial condition:

$$\left(\frac{\partial \bar{W}}{\partial t}\right)_{kl}^{i+1} = -p_l \frac{\bar{W}_{kl}^{i} - \bar{W}_{k-1,l}^{i}}{\Delta} + x_k \frac{\bar{W}_{kl}^{i} - \bar{W}_{k,l-1}^{i}}{\Delta}. \tag{C.15}$$

The averaged time derivative introduced earlier is then obtained as the mean value of the two time derivatives (C.13) and (C.15):

$$\left(\frac{\partial W}{\partial t}\right)_{\text{avg}} = \frac{1}{2}\left[\left(\frac{\partial W}{\partial t}\right)_{kl}^{i} + \left(\frac{\partial \bar{W}}{\partial t}\right)_{kl}^{i+1}\right]. \tag{C.16}$$

Using this expression, an average of two time steps performed with a forward and backward difference respectively, we obtain the final expression for the Wigner function at time $i = 1$:

$$W_{kl}^{i+1} = W_{kl}^{i} + \Delta t \left(\frac{\partial W}{\partial t}\right)_{\text{avg}}. \tag{C.17}$$

The combination of forward and backward differences in both steps makes this method second order accurate without the need to use more complicated higher terms in the Taylor expansion (C.2), [119]). One can also choose to use backward differences in the predictor and forward differences in the corrector step and in our implementation, we alternate between these two possibilities at each time step. There is no mathematical reason for this, just the experience that our simulations appear to be more stable in this case.

C.3 Interactions and collisions

After demonstrating MacCormack's technique on the simple non-interacting case (C.1), we extend our method to include interactions. We recall the collisionless Boltzmann equation with mean-field interactions, given in dimensionless units as

$$\frac{\mathrm{d}}{\mathrm{d}t}\hat{W}(x,p) + p\partial_x \hat{W}(x,p) = i\left[\hat{V}(x), \hat{W}(x,p)\right] + \frac{1}{2}\left\{\partial_x \hat{V}(x), \partial_p \hat{W}(x,p)\right\}. \tag{C.18}$$

The commutator contains no derivative, hence its discretization is very simple:

$$\left[\hat{V}(x), \hat{W}(x,p)\right]_{kl}^{i} = \left[\hat{V}_{k}^{i}, \hat{W}_{kl}^{i}\right]. \tag{C.19}$$

For the anticommutator with derivatives, we note that it actually has the same form as the trapping term, because the x appearing there is the derivative of the harmonic potential. This means, we can add trap and mean-field $\hat{V}(x) = V^{\text{trap}}(x) + \hat{V}^{\text{mf}}(x)$ and evaluate the discretized derivative of $\hat{V}(x)$ as a central difference:

$$\left(\frac{\partial \hat{V}(x)}{\partial x}\right)_k^i = \frac{1}{2\Delta}\left(V_{k+1}^i - V_{k-1}^i\right). \tag{C.20}$$

This is then used as the potential during the MacCormack step sequence.

We obtain the mean-field and collision term by using the standard discretization scheme for integrals

$$\int dx f(x) \approx \Delta \sum_j f_j. \tag{C.21}$$

One exception is the part of the collision integral quadratic in the T-matrix, which features terms such as $\hat{W}(x, p - \frac{1}{2}(q - \sqrt{k^2 + \Delta Q})$, where the value of the collision term at a grid point i, j can depend on an off-grid value of the Wigner function due to a quadratic Zeeman shift ΔQ. We interpolate such values using bilinear interpolation. If the phase-space coordinates are inside a grid square, such that $x_k, < x < x_{k+1}$ and $p_l < p < p_{l+1}$, we approximate the Wigner function at x, p with the expression

$$\begin{aligned} W(x,p) \approx \frac{1}{\Delta^2}\,&[W_{kl}(x_{k+1} - x)(p_{l+1} - p) + W_{k+1,l}(x - x_k)(p_{l+1} - p) \\ &+ W_{k,l+1}(x_{k+1} - x)(p - p_l) + W_{k+1,l+1}(x - x_k)(p - p_l)] \end{aligned} \tag{C.22}$$

and define it to be zero if it is outside of the grid area. In general, we choose the grid such that the Wigner function is effectively zero at the boundary, where we employ periodic boundary conditions to prevent numerical diffusion errors.

C.4 Grid sizes and parallelization

For a good balance of accuracy, stability and demand on computational power, we use phase space grids ranging from 60 × 60 to 120 × 120, with rare exceptions to larger grids for graphs such as Figure 9.5, where complex spatial structures emerge. A sometimes counter-intuitive feature of numerical simulations of partial differential equations is that larger grids, or rather smaller Δ mean lower stability and we need to reduce the time step as well. Simply speaking, the quotient $v_{\max} = \Delta/\Delta t$ defines a "maximum velocity", and if any process in the system exceeds this velocity, the simulation becomes unstable. The occurrence of such unstable situations is difficult to predict a priori for non-linear equations.

In the collisionless case, a rough estimate for the run-time of our simulations is 32 hours on a 90 × 90-grid for a single processor, and 14 days with the collision term, which is the most demanding part. Since the discretized collision term is effectively just a huge summation over many indices, our simulations parallelize well. The same simulations with the collision term mentioned above take about 2 days, when running in parallel on 8 processors. Our entire code is written in FORTRAN 95 and we use the current version GNU and Intel mpi compilers.

Appendix D

Details on the tensor expansion

In this appendix, we provide some further details on the tensor expansion of the Wigner function of chapter 8. We explain how to calculate the coefficients α_l that appear in the tensor expansion of the mean-field potential and lay out the difference between a true spin-3/2 system an the actual system described in that chapter, a subsystem of a spin-9/2 gas, where only the inner four components $m = \pm 1/2, \pm 3/2$ have non-zero populations. We begin by repeating the basic properties of the tensors T_l^m we introduced in section 8.1. For $l > 0$, they are traceless

$$\mathrm{Tr}\left(T_l^m\right) = \begin{cases} 1, \text{ if } l = 0 \\ 0, \text{ if } l > 0. \end{cases} \tag{D.1}$$

With respect to the scalar product defined by the trace, all tensors orthonormal

$$\mathrm{Tr}\left(T_l^m T_{l'}^{m'}\right) = \delta_{ll'}\delta_{mm'}. \tag{D.2}$$

All of them are Hermitian 4×4-matrices

$$T_l^m = \left(T_l^m\right)^\dagger. \tag{D.3}$$

This means that they form a complete orthonormal basis for all 4×4 Hermitian matrices and any such matrix $\hat{M}$ can be expanded in terms of the tensors

$$\hat{M} = \sum_{ml} T_l^m M_l^m. \tag{D.4}$$

The expansion coefficients can be obtained by multiplying Eq. (D.4) with $T_{l'}^{m'}$, taking the trace and using property (D.3):

$$M_l^m = \mathrm{Tr}\left(T_l^m \hat{M}\right). \tag{D.5}$$

We note, that the coupling constants (2.16) are of the following form:

$$\begin{aligned} U_{klmn} &= \sum_{SM} g_s \langle SM|ik\rangle\langle SM|jl\rangle \\ &= \sum_{SM} g_S M_{ik}^{SM} M_{lj}^{SM}, \end{aligned} \tag{D.6}$$

where we defined the Hermitian matrices

$$M_{mn}^{SM} = i\langle SM|mn\rangle \tag{D.7}$$

with a factor of i, since the Clebsch-Gordan coefficients are real and antisymmetric with respect to exchanging m, n for the fermionic case considered in this thesis. For simplicity of notation, we introduce the index $a = (l, m)$ to denote the tensor basis with a single index $a = 1, \ldots, 16$ only, such that $T_l^m \to T^a$.

Being Hermitian matrices, we can expand the matrices (D.7) in terms of T^a and obtain

$$M_{mn}^{SM} = \sum_a M_a^{SM} T_{mn}^a, \tag{D.8}$$

with coefficients

$$M_a^{SM} = \mathrm{Tr}\left(T^a \hat{M}^{SM}\right). \tag{D.9}$$

The product of elements of two such matrices, that appears in the interaction constants (D.6) then expands as

$$M_{ik}^{SM} M_{lj}^{SM} = \sum_{ab} M_a^{SM} M_b^{SM} T_{ik}^a T_{lj}^b. \tag{D.10}$$

The transformation of this expression into a sum of matrices $B_{ij}B_{kl}$ is called a Fierz transformation. Since we have a complete orthonormal basis available, we only need to know how the basis matrices themselves transform:

$$T_{ij}^a T_{kl}^b = \sum_{abcd} C_{abcd} T_{il}^c T_{jk}^d. \tag{D.11}$$

A multiplication of Eq. (D.11) with $T_{li}^e T_{kj}^f$ with a subsequent trace operation reveals that the Fierz coefficients are given by

$$C_{abcd} = \mathrm{Tr}\left((T^d)^{\mathrm{T}} T^b T^c T^a\right). \tag{D.12}$$

Hence, the coupling constants can be rewritten as

$$U_{klmn} = \sum_{SM}\sum_{abcd} g_S M_a^{SM} M_b^{SM} C_{abcd} \left(T_{kl}^c T_{mn}^d\right). \tag{D.13}$$

It is a feature of such Fierz transformations, that when the basis matrices T^a correspond to irreducible representations of a symmetry group (here SU(4)), the coefficients only have few distinct values. Here, the C_{abcd} are only non-zero if $a = b$ and $c = d$. Hence we define $\mathcal{C}_{ab} \equiv C_{aabb}$. As a consequence, the coupling constants (D.13) do not “mix” tensors with different indices and are given as

$$U_{klmn} = \sum_{SM}\sum_{ab} \alpha_a \left(T_{kl}^a T_{mn}^a\right), \tag{D.14}$$

where

$$\alpha_a = \sum_{SM} \sum_{b} g_S M_b^{SM} M_b^{SM} \mathcal{C}_{ba} \left(T_{kl}^b T_{mn}^b \right), \tag{D.15}$$

correspond to the coefficients introduced in section 8.1. This equation gives the prescription on how to obtain the coefficients α_a for arbitrary values of spin, assuming one knows the full set of the corresponding tensors T_l^m with the right properties (rotational invariance, orthogonality, etc.). This is explored in a recent paper for arbitrary spins [86].

It was shown, that for a real spin-3/2 gas, i.e. a system, where the coupling constants depend on the Clebsch-Gordan coefficients for $F = 3/2$:

$$M_a^{SM} = i\langle SM|F = 3/2, m; F = 3/2, n\rangle, \tag{D.16}$$

the coefficients α_a have only three distinct values [87]. Going back to the original indices $a \to (l, m)$, we find that the α_l^m do not depend on m and the coefficients for $l = 1$ and $l = 3$ are degenerate:

$$\alpha_0^0 = \frac{1}{2}\left(g_0 + 5g_2\right), \ \ \alpha_1^m = \frac{1}{2}\left(-g_0 - g_2\right), \ \ \alpha_2^m = \frac{1}{2}\left(g_0 - 3g_2\right), \ \ \alpha_3^m = \frac{1}{2}\left(-g_0 - g_2\right). \tag{D.17}$$

This is a case of an inherent SO(5)-symmetry in spin-3/2 systems [84, 87]. If $g_0 = g_2 \equiv g$, this symmetry increases to SU(4) and all coefficients for $l > 1$ become degenerate

$$\alpha_0^0 = \frac{3}{2}g, \ \ \alpha_{l>1}^m = -g. \tag{D.18}$$

This is actually a feature of all SU(N)-systems (see e.g. [33, 104]). If tensors with the rotational properties can be defined as above, the corresponding coefficients for the interactions would be

$$\alpha_0^0 = \frac{N-1}{2}g, \ \ \alpha_{l>1}^m = -g. \tag{D.19}$$

In contrast, in the system considered in chapter 8, the coupling constants are those for a spin-9/2 system, where we truncate all coupling to outside the subset of spin components given by $m = \pm 1/2, \pm 3/2$. Hence,

$$M_a^{SM} = i\langle SM|F = 9/2, m; F = 9/2, n\rangle. \tag{D.20}$$

With more scattering lengths involved, the expressions for the coefficients α_l^m are considerably more complicated, as is evident from the list below:

$$\begin{aligned}
\alpha_0^0 &= \frac{1}{10}g_0 + \frac{83}{264}g_2 + \frac{1623}{5720}g_4 + \frac{58}{165}g_6 + \frac{322}{715}g_8,\\
\alpha_1^0 = \alpha_1^1 &= -\frac{1}{10}g_0 - \frac{13}{60}g_2 - \frac{387}{2860}g_4 - \frac{97}{1650}g_6 + \frac{7}{650}g_8,\\
\alpha_1^2 &= -\frac{1}{10}g_0 + \frac{29}{1320}g_2 + \frac{9}{1144}g_4 - \frac{16}{165}g_6 + \frac{238}{715}g_8,\\
\alpha_2^0 &= \frac{1}{10}g_0 - \frac{1}{8}g_2 - \frac{87}{520}g_4 - \frac{1}{5}g_6 - \frac{7}{65}g_8,\\
\alpha_2^1 = \alpha_2^2 &= \frac{1}{10}g_0 + \frac{2}{33}g_2 - \frac{54}{715}g_4 - \frac{8}{33}g_6 - \frac{49}{143}g_8,\\
\alpha_2^3 = \alpha_2^4 &= \frac{1}{10}g_0 - \frac{13}{132}g_2 - \frac{321}{2860}g_4 - \frac{59}{330}g_6 - \frac{301}{1430}g_8,\\
\alpha_3^0 &= -\frac{1}{10}g_0 - \frac{93}{440}g_2 - \frac{711}{5720}g_4 - \frac{3}{55}g_6 - \frac{7}{715}g_8,\\
\alpha_3^1 = \alpha_3^2 &= -\frac{1}{10}g_0 - \frac{197}{1760}g_2 - \frac{1143}{22880}g_4 - \frac{67}{1100}g_6 - \frac{1267}{7150}g_8,\\
\alpha_3^3 = \alpha_3^4 &= -\frac{1}{10}g_0 - \frac{149}{1056}g_2 - \frac{1857}{22880}g_4 - \frac{43}{660}g_6 - \frac{161}{1430}g_8,\\
\alpha_3^5 = \alpha_3^6 &= -\frac{1}{10}g_0 - \frac{4}{33}g_2 - \frac{81}{715}g_4 - \frac{16}{165}g_6 - \frac{49}{715}g_8.
\end{aligned}\tag{D.21}$$

Only a few values are degenerate in this case and the coefficients now explicitly depend on m, a fact we suppressed in section 8.1 to keep the description simpler and closer to a true spin-3/2 system.

That the "truncated" spin-9/2 system is nevertheless sufficiently close to the true spin-3/2 case becomes evident, if we introduce the coefficients

$$a_l^m = \frac{M}{4\pi\hbar^2}\alpha_l^m, \tag{D.22}$$

i.e. we express them as scattering lengths. In units of Bohr radii a_B, using the values for ^{40}K (see table 8.4), they are given as

$$\begin{aligned}
a_0^0 &= 238.428\, a_B,\\
a_1^0 = a_1^1 &= -73.7641\, a_B,\\
a_1^2 &= -79.672\, a_B,\\
a_2^0 &= -84.7898\, a_B,\\
a_2^1 = a_2^2 &= -89.2074\, a_B,\\
a_2^3 = a_2^4 &= -85.8012\, a_B,\\
a_3^0 &= -73.9663\, a_B,\\
a_3^1 = a_3^2 &= -76.5611\, a_B,\\
a_3^3 = a_3^4 &= -75.7148\, a_B,\\
a_3^5 = a_3^6 &= -75.8078\, a_B.
\end{aligned}\tag{D.23}$$

Here, we see that the values for each l do not deviate too strongly, justifying the treatment of the truncated spin-9/2 as a spin-3/2 system in section 8.1.

Appendix E

Explicit form of irreducible tensors for spin 3/2

In this appendix, we provide the full matrix expressions for the tensors T_l^m introduced in chapter 8. We begin by repeating their definition:

$$
\begin{aligned}
&T_0^0 = \frac{1}{2}\mathbb{1}, \qquad T_1^0 = \frac{1}{\sqrt{5}}S_x, \qquad T_1^1 = \frac{1}{\sqrt{5}}S_y, \qquad T_1^2 = \frac{1}{\sqrt{5}}S_z,\\
&T_2^0 = \frac{1}{2}\left(S_z^2 - \frac{5}{4}\mathbb{1}\right), \qquad T_2^1 = \frac{1}{2\sqrt{3}}\left(S_x^2 - S_y^2\right), \qquad T_2^2 = \frac{1}{2\sqrt{3}}\left(S_xS_y + S_yS_x\right),\\
&T_2^3 = \frac{1}{2\sqrt{3}}\left(S_zS_x + S_xS_z\right), \qquad T_2^4 = \frac{1}{2\sqrt{3}}\left(S_yS_z + S_zS_y\right),\\
&T_3^0 = \frac{\sqrt{5}}{3}\left(S_z^3 - \frac{41}{20}S_z\right), \qquad T_3^1 = \frac{\sqrt{5}}{3}\left(S_x^3 - \frac{41}{20}S_x\right), \qquad T_3^2 = \frac{\sqrt{5}}{3}\left(S_y^3 - \frac{41}{20}S_y\right),\\
&T_3^3 = \frac{1}{2\sqrt{3}}\left\{S_x, S_y^2 - S_z^2\right\}, \qquad T_3^4 = \frac{1}{2\sqrt{3}}\left\{S_y, S_z^2 - S_x^2\right\}, \qquad T_3^5 = \frac{1}{2\sqrt{3}}\left\{S_z, S_x^2 - S_y^2\right\},\\
&T_3^6 = \frac{1}{\sqrt{3}}\left(S_xS_yS_z + S_zS_yS_x\right). \qquad\qquad \text{(E.1)}
\end{aligned}
$$

These tensors are constructed using the 4×4 identity matrix $\mathbb{1}$ and the spin-3/2 matrices

$$
\mathbb{1} = \begin{pmatrix} 1 & 0 & 0 & 0\\ 0 & 1 & 0 & 0\\ 0 & 0 & 1 & 0\\ 0 & 0 & 0 & 1 \end{pmatrix}, \qquad S_x = \frac{1}{2}\begin{pmatrix} 0 & \sqrt{3} & 0 & 0\\ \sqrt{3} & 0 & 2 & 0\\ 0 & 2 & 0 & \sqrt{3}\\ 0 & 0 & \sqrt{3} & 0 \end{pmatrix},
$$

$$
S_y = \frac{i}{2}\begin{pmatrix} 0 & -\sqrt{3} & 0 & 0\\ \sqrt{3} & 0 & -2 & 0\\ 0 & 2 & 0 & -\sqrt{3}\\ 0 & 0 & \sqrt{3} & 0 \end{pmatrix}, \quad S_z = \frac{1}{2}\begin{pmatrix} 3 & 0 & 0 & 0\\ 0 & 1 & 0 & 0\\ 0 & 0 & -1 & 0\\ 0 & 0 & 0 & -3 \end{pmatrix}.
$$

In full matrix form, the 16 tensors T_l^m are given by

$$T_0^0 = \frac{1}{2}\begin{pmatrix} 1 & 0 & 0 & 0 \\ 0 & 1 & 0 & 0 \\ 0 & 0 & 1 & 0 \\ 0 & 0 & 0 & 1 \end{pmatrix}, \qquad T_1^0 = \frac{1}{2\sqrt{5}}\begin{pmatrix} 0 & \sqrt{3} & 0 & 0 \\ \sqrt{3} & 0 & 2 & 0 \\ 0 & 2 & 0 & \sqrt{3} \\ 0 & 0 & \sqrt{3} & 0 \end{pmatrix},$$

$$T_1^1 = \frac{i}{2\sqrt{5}}\begin{pmatrix} 0 & -\sqrt{3} & 0 & 0 \\ \sqrt{3} & 0 & -2 & 0 \\ 0 & 2 & 0 & -\sqrt{3} \\ 0 & 0 & \sqrt{3} & 0 \end{pmatrix}, \qquad T_1^2 = \frac{1}{2\sqrt{5}}\begin{pmatrix} 3 & 0 & 0 & 0 \\ 0 & 1 & 0 & 0 \\ 0 & 0 & -1 & 0 \\ 0 & 0 & 0 & -3 \end{pmatrix},$$

$$T_2^0 = \frac{1}{2}\begin{pmatrix} 1 & 0 & 0 & 0 \\ 0 & -1 & 0 & 0 \\ 0 & 0 & -1 & 0 \\ 0 & 0 & 0 & 1 \end{pmatrix}, \qquad T_2^1 = \frac{1}{2}\begin{pmatrix} 0 & 0 & 1 & 0 \\ 0 & 0 & 0 & 1 \\ 1 & 0 & 0 & 0 \\ 0 & 1 & 0 & 0 \end{pmatrix},$$

$$T_2^2 = \frac{i}{2}\begin{pmatrix} 0 & 0 & -1 & 0 \\ 0 & 0 & 0 & -1 \\ 1 & 0 & 0 & 0 \\ 0 & 1 & 0 & 0 \end{pmatrix}, \qquad T_2^3 = \frac{1}{2}\begin{pmatrix} 0 & 1 & 0 & 0 \\ 1 & 0 & 0 & 0 \\ 0 & 0 & 0 & -1 \\ 0 & 0 & -1 & 0 \end{pmatrix},$$

$$T_2^4 = \frac{i}{2}\begin{pmatrix} 0 & -1 & 0 & 0 \\ 1 & 0 & 0 & 0 \\ 0 & 0 & 0 & 1 \\ 0 & 0 & -1 & 0 \end{pmatrix}, \qquad T_3^0 = \frac{1}{2\sqrt{5}}\begin{pmatrix} 1 & 0 & 0 & 0 \\ 0 & -3 & 0 & 0 \\ 0 & 0 & 3 & 0 \\ 0 & 0 & 0 & -1 \end{pmatrix},$$

$$T_3^1 = \frac{1}{4\sqrt{5}}\begin{pmatrix} 0 & -\sqrt{3} & 0 & 5 \\ -\sqrt{3} & 0 & 3 & 0 \\ 0 & 3 & 0 & -\sqrt{3} \\ 5 & 0 & -\sqrt{3} & 0 \end{pmatrix}, \quad T_3^2 = \frac{i}{2\sqrt{5}}\begin{pmatrix} 0 & \sqrt{3} & 0 & 5 \\ -\sqrt{3} & 0 & -3 & 0 \\ 0 & 3 & 0 & \sqrt{3} \\ -5 & 0 & -\sqrt{3} & 0 \end{pmatrix},$$

$$T_3^3 = \frac{1}{4}\begin{pmatrix} 0 & -1 & 0 & -\sqrt{3} \\ -1 & 0 & \sqrt{3} & 0 \\ 0 & \sqrt{3} & 0 & -1 \\ -\sqrt{3} & 0 & -1 & 0 \end{pmatrix}, \qquad T_3^4 = \frac{i}{4}\begin{pmatrix} 0 & -1 & 0 & \sqrt{3} \\ 1 & 0 & \sqrt{3} & 0 \\ 0 & -\sqrt{3} & 0 & -1 \\ -\sqrt{3} & 0 & 1 & 0 \end{pmatrix},$$

$$T_3^5 = \frac{1}{2}\begin{pmatrix} 0 & 0 & 1 & 0 \\ 0 & 0 & 0 & -1 \\ 1 & 0 & 0 & 0 \\ 0 & -1 & 0 & 0 \end{pmatrix}, \qquad T_3^6 = \frac{i}{2}\begin{pmatrix} 0 & 0 & -1 & 0 \\ 0 & 0 & 0 & 1 \\ 1 & 0 & 0 & 0 \\ 0 & -1 & 0 & 0 \end{pmatrix}.$$

Bibliography

[1] L. P. Pitaevskii and S. Stringari, *Bose-Einstein Condensation* (Clarendon Press, 2003).

[2] C. J. Pethick and H. Smith, *Bose-Einstein Condensation in Dilute Gases* (Cambridge University Press, 2002).

[3] M. Lewenstein, A. Sanpera, and V. Ahufinger, *Ultracold Atoms in Optical Lattices: Simulating Quantum Many-Body Systems* (Oxford University Press, 2012).

[4] D. M. Stamper-Kurn and M. Ueda, *Spinor Bose gases: Symmetries, magnetism, and quantum dynamics*, Rev. Mod. Phys. **85**, 1191 (2013).

[5] D. D. Osheroff, R. C. Richardson, and D. M. Lee, *Evidence for a New Phase of Solid He3*, Phys. Rev. Lett. **28**, 885 (1972).

[6] H. Anderson, J. R. Ensher, M. R. Matthews, C. E. Wieman, and E. A. Cornell, *Observation of Bose-Einstein Condensation in a Dilute Atomic Vapor*, Science **269**, 198 (1995).

[7] K. B. Davis, M. O. Mewes, M. R. Andrews, N. J. van Druten, D. S. Durfee, D. M. Kurn, and W. Ketterle, *Bose-Einstein Condensation in a Gas of Sodium Atoms*, Phys. Rev. Lett. **75**, 3969 (1995).

[8] B. DeMarco and D. S. Jin, *Exploring a quantum degenerate gas of fermionic atoms*, Phys. Rev. A **58**, R4267 (1998).

[9] M. Greiner, O. Mandel, T. Esslinger, T. W. Hänsch, and I. Bloch, *Quantum phase transition from a superfluid to a Mott insulator in a gas of ultracold atoms*, Nature **415**, 39 (2002).

[10] C. A. Regal, M. Greiner, and D. S. Jin, *Observation of Resonance Condensation of Fermionic Atom Pairs*, Phys. Rev. Lett. **92**, 040403 (2004).

[11] M. Zwierlein, J. R. Abo-Shaeer, A. Schirotzek, C. H. Schunck, and W. Ketterle, *Vortices and superfluidity in a strongly interacting Fermi gas*, Nature (London) **435**, 1047 (2005).

[12] G. B. Jo, Y. R. Lee, J. H. Choil, C. A. Christensen, T. H. Kim, J. H. Thywissen, D. E. Pritchard, and W. Ketterle, *Itinerant Ferromagnetism in a Fermi Gas of Ultracold Atoms*, Science **325**, 1521 (2009).

[13] G. J. Conduit and E. Altman, *Effect of three-body loss on itinerant ferromagnetism in an atomic Fermi gas*, Phys. Rev. A **83**, 043618 (2011).

[14] D. Pekker, M. Babadi, R. Sensarma, N. Zinner, L. Pollet, M. W. Zwierlein, and E. Demler, *Competition between Pairing and Ferromagnetic Instabilities in Ultracold Fermi Gases near Feshbach Resonances*, Phys. Rev. Lett. **106**, 050402 (2011).

[15] S. Zhang and T.-L. Ho, *Atom loss maximum in ultra-cold Fermi gases*, New Journal of Physics **13**, 055003 (2011).

[16] M. Ueda and M. Koashi, *Theory of spin-2 Bose-Einstein condensates: Spin correlations, magnetic response, and excitation spectra*, Phys. Rev. A **65**, 063602 (2002).

[17] H. Mäkelä and K.-A. Suominen, *Ground states of spin-3 Bose-Einstein condensates for conserved magnetization*, Phys. Rev. A **75**, 033610 (2007).

[18] R. B. Diener and T.-L. Ho, ^{52}Cr *Spinor Condensate: A Biaxial or Uniaxial Spin Nematic*, Phys. Rev. Lett. **96**, 190405 (2006).

[19] R. Barnett, A. Turner, and E. Demler, *Classifying Novel Phases of Spinor Atoms*, Phys. Rev. Lett. **97**, 180412 (2006).

[20] A. Sommer, M. Ku, G. Roati, and M. W. Zwierlein, *Universal spin transport in a strongly interacting Fermi gas*, Nature (London) **472**, 201 (2011).

[21] M. Koschorreck, D. Pertot, E. Vogt, and M. Köhl, *Universal spin dynamics in two-dimensional Fermi gases*, Nat. Phys. **9**, 405 (2013).

[22] M. Vengalattore, S. R. Leslie, J. Guzman, and D. M. Stamper-Kurn, *Spontaneously Modulated Spin Textures in a Dipolar Spinor Bose-Einstein Condensate*, Phys. Rev. Lett. **100**, 170403 (2008).

[23] J. Kronjäger, C. Becker, P. Soltan-Panahi, K. Bongs, and K. Sengstock, *Spontaneous Pattern Formation in an Antiferromagnetic Quantum Gas*, Phys. Rev. Lett. **105**, 090402 (2010).

[24] M. Srednicki, *Chaos and quantum thermalization*, Phys. Rev. E **50**, 888 (1994).

[25] M. Rigol, V. Dunjko, and M. Olshanii, *Thermalization and its mechanism for generic isolated quantum systems*, Nature (London) **452**, 854 (2008).

[26] J. Dziarmaga, *Dynamics of a quantum phase transition and relaxation to a steady state*, Advances in Physics **59**, 1063 (2010).

[27] A. Polkovnikov, K. Sengupta, A. Silva, and M. Vengalattore, *Colloquium : Nonequilibrium dynamics of closed interacting quantum systems*, Rev. Mod. Phys. **83**, 863 (2011).

[28] M. Gring, M. Kuhnert, T. Langen, T. Kitagawa, B. Rauer, M. Schreitl, I. Mazets, D. A. Smith, E. Demler, and J. Schmiedmayer, *Relaxation and Prethermalization in an Isolated Quantum System*, Science **337**, 1318 (2012).

[29] T. Langen, R. Geiger, M. Kuhnert, B. Rauer, and J. Schmiedmayer, *Local emergence of thermal correlations in an isolated quantum many-body system*, Nat. Phys. **9**, 640 (2013).

[30] S. Trotzky, Y.-A. Chen, A. Flesch, I. P. McCulloch, U. Schollwöck, J. Eisert, and I. Bloch, *Probing the relaxation towards equilibrium in an isolated strongly correlated one-dimensional Bose gas*, Nat. Phys. **8**, 325 (2012).

[31] C. Honerkamp and W. Hofstetter, *Ultracold Fermions and the* SU(N) *Hubbard Model*, Phys. Rev. Lett. **92**, 170403 (2004).

[32] A. V. Gorshkov, M. Hermele, V. Gurarie, C. Xu, P. S. Julienne, J. Ye, P. Zoller, E. Demler, M. D. Lukin, and A. M. Rey, *Two-orbital SU(N) magnetism with ultracold alkaline-earth atoms*, Nature Physics **6**, 289 (2010).

[33] M. A. Cazalilla, A. F. Ho, and M. Ueda, *Ultracold gases of ytterbium: ferromagnetism and Mott states in an SU(6) Fermi system*, New. J. Phys. **11**, 103033 (2009).

[34] A. J. Daley, M. M. Boyd, J. Ye, and P. Zoller, *Quantum Computing with Alkaline-Earth-Metal Atoms*, Phys. Rev. Lett. **101**, 170504 (2008).

[35] F. Schreck, S. Stellmer, and T. C. Killian, *Degenerate Quantum Gases of Strontium*, in *Annual Review of Cold Atoms and Molecules* (World Scientific, 2014), vol. 2, chap. 1, pp. 1–80.

[36] Y. Kawaguchi and M. Ueda, *Spinor Bose-Einstein condensates*, Physics Reports **520**, 253 (2012).

[37] M. S. Chang, Q. Qin, W. Zhang, L. You, and M. S. Chapman, *Coherent spinor dynamics in a spin-1 Bose condensate*, Nat. Phys. **1**, 111 (2005).

[38] H. Schmaljohann, M. Erhard, J. Kronjäger, M. Kottke, S. van Staa, L. Cacciapuoti, J. J. Arlt, K. Bongs, and K. Sengstock, *Dynamics of* $F = 2$ *Spinor Bose-Einstein Condensates*, Phys. Rev. Lett. **92**, 040402 (2004).

[39] C. Gerving, T. Hoang, B. Land, M. Anquez, C. Hamley, and M. Chapman, *Nonequilibrium dynamics of an unstable quantum pendulum explored in a spin-1 Bose-Einstein condensate*, Nature Communications **3**, 1169 (2012).

[40] Y. Endo and T. Nikuni, *Spin Dynamics of a Trapped Spin-1 Bose Gas above the Bose-Einstein Transition Temperature*, J. Low Temp. Phys. **152**, 21 (2008).

[41] S. S. Natu and E. J. Mueller, *Spin waves in a spin-1 normal Bose gas*, Phys. Rev. A **81**, 053617 (2010).

[42] H. K. Pechkis, J. P. Wrubel, A. Schwettmann, P. F. Griffin, R. Barnett, E. Tiesinga, and P. D. Lett, *Spinor Dynamics in an Antiferromagnetic Spin-1 Thermal Bose Gas*, Phys. Rev. Lett. **111**, 025301 (2013).

[43] J. M. McGuirk and L. F. Zajiczek, *Optical excitation of nonlinear spin waves*, New Journal of Physics **12**, 103020 (2010).

[44] T. Nikuni, J. E. Williams, and C. W. Clark, *Linear spin waves in a trapped Bose gas*, Phys. Rev. A **66**, 043411 (2002).

[45] L. Santos and T. Pfau, *Spin-3 Chromium Bose-Einstein Condensates*, Phys. Rev. Lett. **96**, 190404 (2006).

[46] S. Trotzky, P. Cheinet, S. Fölling, M. Feld, U. Schnorrberger, A. M. Rey, A. Polkovnikov, E. A. Demler, M. D. Lukin, and I. Bloch, *Time-Resolved Observation and Control of Superexchange Interactions with Ultracold Atoms in Optical Lattices*, Science **319**, 295 (2008).

[47] E. Haller, R. Hart, M. J. Mark, J. G. Danzl, L. Reichsöllner, M. Gustavsson, M. Dalmonte, G. Pupillo, and H. C. Nägerl, *Pinning quantum phase transition for a Luttinger liquid of strongly interacting bosons*, Nature **466**, 597 (2010).

[48] J. Zhang, F. M. Cucchietti, C. M. Chandrashekar, M. Laforest, C. A. Ryan, M. Ditty, A. Hubbard, J. K. Gamble, and R. Laflamme, *Direct observation of quantum criticality in Ising spin chains*, Phys. Rev. A **79**, 012305 (2009).

[49] A. Friedenauer, H. Schmitz, J. T. Glueckert, D. Poraas, and T. Schaetz, *Simulating a quantum magnet with trapped ions*, Nature Physics **4**, 757 (2008).

[50] T. W. B. Kibble, *Topology of cosmic domains and strings*, Journal of Physics A: Mathematical and General **9**, 1387 (1976).

[51] W. H. Zurek, *Cosmological experiments in superfluid helium?*, Nature **317**, 505 (1985).

[52] J. Berges, S. Borsányi, and C. Wetterich, *Prethermalization*, Phys. Rev. Lett. **93**, 142002 (2004).

[53] S. R. White, *Density matrix formulation for quantum renormalization groups*, Phys. Rev. Lett. **69**, 2863 (1992).

[54] U. Schollwöck, *The density-matrix renormalization group*, Rev. Mod. Phys. **77**, 259 (2005).

[55] G. Vidal, *Efficient Classical Simulation of Slightly Entangled Quantum Computations*, Phys. Rev. Lett. **91**, 147902 (2003).

[56] U. Ebling, A. Eckardt, and M. Lewenstein, *Spin segregation via dynamically induced long-range interactions in a system of ultracold fermions*, Phys. Rev. A **84**, 063607 (2011).

[57] J. Heinze, J. S. Krauser, N. Fläschner, K. Sengstock, C. Becker, U. Ebling, A. Eckardt, and M. Lewenstein, *Engineering Spin Waves in a High-Spin Ultracold Fermi Gas*, Phys. Rev. Lett. **110**, 250402 (2013).

[58] J. S. Krauser, U. Ebling, N. Fläschner, J. Heinze, K. Sengstock, M. Lewenstein, A. Eckardt, and C. Becker, *Giant Spin Oscillations in an Ultracold Fermi Sea*, Science **343**, 157 (2014).

[59] U. Ebling, J. S. Krauser, N. Fläschner, K. Sengstock, C. Becker, M. Lewenstein, and A. Eckardt, *Relaxation Dynamics of an Isolated Large-Spin Fermi Gas Far from Equilibrium*, Phys. Rev. X **4**, 021011 (2014).

[60] B. DeMarco, *Quantum Behavior of an Atomic Fermi Gas*, Ph.D. thesis, University of Colorado (2001).

[61] S. Giorgini, L. P. Pitaevskii, and S. Stringari, *Theory of ultracold atomic Fermi gases*, Rev. Mod. Phys. **80**, 1215 (2008).

[62] L. D. Landau and E. M. Lifshits, *Quantum Mechanics: Non-relativistic Theory* (Butterworth-Heinemann, 1977).

[63] K. Huang and C. N. Yang, *Quantum-Mechanical Many-Body Problem with Hard-Sphere Interaction*, Phys. Rev. **105**, 767 (1957).

[64] J. N. Fuchs, D. M. Gangardt, and F. Laloë, *Large amplitude spin waves in ultra-cold gases*, Eur. Phys. J. D **25**, 57 (2003).

[65] S. S. Natu and E. J. Mueller, *Anomalous spin segregation in a weakly interacting two-component Fermi gas*, Phys. Rev. A **79**, 051601 (2009).

[66] M. Hillery, R. O'Connell, M. Scully, and E. Wigner, *Distribution functions in physics: Fundamentals*, Physics Reports **106**, 121 (1984).

[67] C. Kurtsiefer, T. Pfau, and J. Mlynek, *Measurement of the Wigner function of an ensemble of Helium atoms*, Nature **386**, 150 (1997).

[68] W. P. Schleich, *Quantum Optics in Phase Space* (Wiley, 2001).

[69] L. R. Corruccini, D. D. Osheroff, D. M. Lee, and R. C. Richardson, *Spin-wave phenomena in liquid ^{3}He systems*, J. Low Temp. Phys. **8**, 229 (1972).

[70] E. P. Bashkin, *Spin waves in polarized paramagnetic gases*, JETP Lett. **33**, 8 (1981).

[71] L. P. Lévy and A. E. Ruckenstein, *Collective Spin Oscillations in Spin-Polarized Gases: Spin-Polarized Hydrogen*, Phys. Rev. Lett. **52**, 1512 (1984).

[72] W. J. Gully and W. J. Mullin, *Observation of Spin Rotation Effects in Polarized* ^{3}He-^{4}He *Mixtures*, Phys. Rev. Lett. **52**, 1810 (1984).

[73] B. R. Johnson, J. S. Denker, N. Bigelow, L. P. Lévy, J. H. Freed, and D. M. Lee, *Observation of Nuclear Spin Waves in Spin-Polarized Atomic Hydrogen Gas*, Phys. Rev. Lett. **52**, 1508 (1984).

[74] C. Lhuillier and F. Laloë, *Transport properties in a spin polarized gas, I*, J. Phys. (Paris) **43**, 197 (1982).

[75] C. Lhuillier and F. Laloë, *Transport properties in a spin polarized gas, II*, J. Phys. (Paris) **43**, 225 (1982).

[76] C. Lhuillier and F. Laloë, *Spin Oscillations in Polarized Gases*, Phys. Rev. Lett. **54**, 1207 (1985).

[77] F. Piéchon, J. N. Fuchs, and F. Laloë, *Cumulative Identical Spin Rotation Effects in Collisionless Trapped Atomic Gases*, Phys. Rev. Lett. **102**, 215301 (2009).

[78] S. L. Adler, *Normalization of collisional decoherence: squaring the delta function, and an independent cross-check*, Journal of Physics A: Mathematical and General **39**, 14067 (2006).

[79] J.-N. Fuchs, *Contribution à la méchanique statistique quantique des gaz froids*, Ph.D. thesis, Université Paris VI (2003).

[80] M. Olshanii, *Atomic Scattering in the Presence of an External Confinement and a Gas of Impenetrable Bosons*, Phys. Rev. Lett. **81**, 938 (1998).

[81] X. Du, L. Luo, B. Clancy, and J. E. Thomas, *Observation of Anomalous Spin Segregation in a Trapped Fermi Gas*, Phys. Rev. Lett. **101**, 150401 (2008).

[82] G. J. Conduit and E. Altman, *Dynamical instability of a spin spiral in an interacting Fermi gas as a probe of the Stoner transition*, Phys. Rev. A **82**, 043603 (2010).

[83] J. M. McGuirk, H. J. Lewandowski, D. M. Harber, T. Nikuni, J. E. Williams, and E. A. Cornell, *Spatial Resolution of Spin Waves in an Ultracold Gas*, Phys. Rev. Lett. **89**, 090402 (2002).

[84] C. Wu, *Hidden Symmetry and Quantum Phases in Spin-3/2 Cold Atomic Systems*, Modern Physics Letters B **20**, 1707 (2006).

[85] J. S. Krauser, *Spin dynamics in fermionic quantum gases - from two-particle to many-body physics*, Ph.D. thesis, Universität Hamburg (2014).

[86] T.-L. Ho and B. Huang, *The Local Spin Structure of Large Spin Fermions*, ArXiv e-prints (2014), `1401.4513`.

[87] C. Wu, J.-P. Hu, and S.-C. Zhang, *Exact SO(5) Symmetry in the Spin-*$3/2$ *Fermionic System*, Phys. Rev. Lett. **91**, 186402 (2003).

[88] S. Murakami, N. Nagosa, and S.-C. Zhang, *SU(2) non-Abelian holonomy and dissipationless spin current in semiconductors*, Phys. Rev. B **69**, 235206 (2004).

[89] C. Wu, *Exotic many-body physics with large-spin Fermi gases*, Physics **3**, 92 (2010).

[90] J. S. Krauser, J. Heinze, N. Fläschner, S. Götze, O. Jürgensen, D.-S. Lühmann, C. Becker, and K. Sengstock, *Coherent multi-flavour spin dynamics in a fermionic quantum gas*, Nat. Phys. **8**, 813 (2012).

[91] W. Kohn, *Cyclotron Resonance and de Haas-van Alphen Oscillations of an Interacting Electron Gas*, Phys. Rev. **123**, 1242 (1961).

[92] D. M. Stamper-Kurn, M. R. Andrews, A. P. Chikkatur, S. Inouye, H.-J. Miesner, J. Stenger, and W. Ketterle, *Optical Confinement of a Bose-Einstein Condensate*, Phys. Rev. Lett. **80**, 2027 (1998).

[93] T. Ohmi and K. Machida, *Bose-Einstein Condensation with Internal Degrees of Freedom in Alkali Atom Gases*, Journal of the Physical Society of Japan **67**, 1822 (1998).

[94] T.-L. Ho, *Spinor Bose Condensates in Optical Traps*, Phys. Rev. Lett. **81**, 742 (1998).

[95] J. Stenger, S. Inouye, D. M. Stamper-Kurn, H.-J. Miesner, A. P. Chikkatur, and W. Ketterle, *Spin domains in ground-state Bose-Einstein condensates*, Nature (London) **396**, 345 (1998).

[96] J. Mur-Petit, M. Guilleumas, A. Polls, A. Sanpera, M. Lewenstein, K. Bongs, and K. Sengstock, *Dynamics of* $F = 1$ ^{87}Rb *condensates at finite temperatures*, Phys. Rev. A **73**, 013629 (2006).

[97] C. Klempt, O. Topic, G. Gebreyesus, M. Scherer, T. Henninger, P. Hyllus, W. Ertmer, L. Santos, and J. J. Arlt, *Multiresonant Spinor Dynamics in a Bose-Einstein Condensate*, Phys. Rev. Lett. **103**, 195302 (2009).

[98] Q. Beaufils, R. Chicireanu, T. Zanon, B. Laburthe-Tolra, E. Maréchal, L. Vernac, J.-C. Keller, and O. Gorceix, *All-optical production of chromium Bose-Einstein condensates*, Phys. Rev. A **77**, 061601 (2008).

[99] J. Miao, J. Hostetter, G. Stratis, and M. Saffman, *Magneto-optical trapping of holmium atoms*, Phys. Rev. A **89**, 041401 (2014).

[100] M. Lu, S. H. Youn, and B. L. Lev, *Trapping Ultracold Dysprosium: A Highly Magnetic Gas for Dipolar Physics*, Phys. Rev. Lett. **104**, 063001 (2010).

[101] Y. Dong and H. Pu, *Spin mixing in spinor Fermi gases*, Phys. Rev. A **87**, 043610 (2013).

[102] K. Rodríguez, A. Argüelles, M. Colomé-Tatché, T. Vekua, and L. Santos, *Mott-Insulator Phases of Spin-*3/2 *Fermions in the Presence of Quadratic Zeeman Coupling*, Phys. Rev. Lett. **105**, 050402 (2010).

[103] J. Jaramillo, S. Greschner, and T. Vekua, *Band-to-Mott-insulator transformations in four-component alkali-metal fermions at half-filling*, Phys. Rev. A **88**, 043616 (2013).

[104] M. A. Cazalilla and A. M. Rey, *Ultracold Fermi Gases with Emergent SU(N) Symmetry*, ArXiv e-prints (2014), `1403.2792`.

[105] K. Gawryluk, M. Brewczyk, K. Bongs, and M. Gajda, *Resonant Einstein–de Haas Effect in a Rubidium Condensate*, Phys. Rev. Lett. **99**, 130401 (2007).

[106] Y. Kawaguchi, H. Saito, and M. Ueda, *Einstein–de Haas Effect in Dipolar Bose-Einstein Condensates*, Phys. Rev. Lett. **96**, 080405 (2006).

[107] Y. Kawaguchi, H. Saito, and M. Ueda, *Can Spinor Dipolar Effects Be Observed in Bose-Einstein Condensates?*, Phys. Rev. Lett. **98**, 110406 (2007).

[108] S. Kotochigova and A. Petrov, *Anisotropy in the interaction of ultracold dysprosium*, Phys. Chem. Chem. Phys. **13**, 19165 (2011).

[109] C. D. Fertig, K. M. O'Hara, J. H. Huckans, S. L. Rolston, W. D. Phillips, and J. V. Porto, *Strongly Inhibited Transport of a Degenerate 1D Bose Gas in a Lattice*, Phys. Rev. Lett. **94**, 120403 (2005).

[110] T. Kinoshita, T. Wenger, and D. S. Weiss, *A quantum Newton's cradle*, Nature **440**, 900 (2006).

[111] E. Timmermans, *Degenerate Fermion Gas Heating by Hole Creation*, Phys. Rev. Lett. **87**, 240403 (2001).

[112] E. Zaremba, T. Nikuni, and A. Griffin, *Dynamics of Trapped Bose Gases at Finite Temperatures*, Journal of Low Temperature Physics **116**, 277 (1999).

[113] N. P. Proukakis and B. Jackson, *Finite-temperature models of Bose–Einstein condensation*, Journal of Physics B: Atomic, Molecular and Optical Physics **41**, 203002 (2008).

[114] M. Lu, N. Q. Burdick, and B. L. Lev, *Quantum Degenerate Dipolar Fermi Gas*, Phys. Rev. Lett. **108**, 215301 (2012).

[115] T. G. Tiecke, *Feshbach resonances in ultracold mixtures of the fermionic quantum gases ^{6}Li and ^{40}K.*, Ph.D. thesis, University of Amsterdam (2009).

[116] E. Arimondo, M. Inguscio, and P. Violino, *Experimental determinations of the hyperfine structure in the alkali atoms*, Rev. Mod. Phys. **49**, 31 (1977).

[117] G. Breit and I. I. Rabi, *Measurement of Nuclear Spin*, Phys. Rev. **38**, 2082 (1931).

[118] W. H. Press, B. P. Flannery, S. A. Teukolsky, and W. T. Vetterling, *Numerical Recipes* (Cambridge University Press, Cambridge, 2007), 3rd ed.

[119] J. D. Anderson, Jr., *Computational Fluid Dynamics* (McGraw-Hill, 1995), 1st ed.

[120] R. W. MacCormack, *The Effect of Viscosity in Hypervelocity Impact Cratering*, Journal of Spacecraft and Rockets **40**, 757 (2003).